1.0

4.5
5.0
5.6

2.8 2.5

3.2 2.2

3.6

4.0 2.0

1.1

1.8

1.25 1.4 1.6

MICROCOPY RESOLUTION TEST CHART

NATIONAL BUREAU OF STANDARDS-1963-A

DNA 4087F

IN SITU CONSTITUTIVE RELATIONS OF SOILS AND ROCKS

ADA064123

SRI International
333 Ravenswood Avenue
Menlo Park, California 94025

August 1976
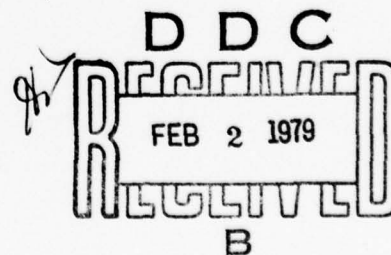
Final Report for Period 4 September 1974—3 November 1975

CONTRACT No. DNA 001-75-C-0077

DDC FILE COPY.

D D C
RECEIVED
FEB 2 1979
B

Prepared for

Director

DEFENSE NUCLEAR AGENCY

Washington, D. C. 20305

78 12 14 003

SECURITY CLASSIFICATION OF THIS PAGE *(When Data Entered)*

REPORT DOCUMENTATION PAGE		READ INSTRUCTIONS BEFORE COMPLETING FORM
1. REPORT NUMBER DNA 4087F	2. GOVT ACCESSION NO.	3. RECIPIENT'S CATALOG NUMBER
4. TITLE *(and Subtitle)* IN SITU CONSTITUTIVE RELATIONS OF SOILS AND ROCKS		5. TYPE OF REPORT & PERIOD COVERED Final Report For Period 4 Sep 74—3 Nov 75
		6. PERFORMING ORG. REPORT NUMBER SRI Project PYU-3698
7. AUTHOR(s) J. T. Rosenberg C. W. Smith D. R. Curran, Supervisor		8. CONTRACT OR GRANT NUMBER(s) DNA 001-75-C-0077
9. PERFORMING ORGANIZATION NAME AND ADDRESS SRI International 333 Ravenswood Avenue Menlo Park, California 94025		10. PROGRAM ELEMENT, PROJECT, TASK AREA & WORK UNIT NUMBERS Subtask Y99QAXSB047-82
11. CONTROLLING OFFICE NAME AND ADDRESS Director Defense Nuclear Agency Washington, D.C. 20305		12. REPORT DATE August 1976
		13. NUMBER OF PAGES 116
14. MONITORING AGENCY NAME & ADDRESS*(if different from Controlling Office)*		15. SECURITY CLASS *(of this report)* UNCLASSIFIED
		15a. DECLASSIFICATION/DOWNGRADING SCHEDULE
16. DISTRIBUTION STATEMENT *(of this Report)* Approved for public release; distribution unlimited.		
17. DISTRIBUTION STATEMENT *(of the abstract entered in Block 20, if different from Report)*		

18. SUPPLEMENTARY NOTES

This work sponsored by the Defense Nuclear Agency under RDT&E RMSS Code B344075464 Y99QAXSB04782 H2590D.

19. KEY WORDS *(Continue on reverse side if necessary and identify by block number)*

Constitutive Relations	Spherical Flow
Lagrange Analysis	In Situ Measurements
LASS	Ground Motion Measurements
Dynamic Response	Stress Gages
Stress-Strain Trajectories	Ytterbium Gages

20. ABSTRACT *(Continue on reverse side if necessary and identify by block number)*

Current results of an ongoing SRI program to determine dynamic in situ stress-strain response at field sites are presented. The method used was the LASS technique (Lagrange analysis for stresses and strains). In this technique field measurements of radial stress and particle velocity histories induced by explosive loading are combined with a numerical analysis to solve the governing partial differential flow equations for the desired stress and strain trajectories. The first successful LASS field test, performed as an

DD FORM
1 JAN 73 **1473** EDITION OF 1 NOV 65 IS OBSOLETE

SECURITY CLASSIFICATION OF THIS PAGE *(When Data Entered)*

19.   KEY WORDS (Continued)

Particle Velocity Gages
Mutual Inductance Particle Velocity Gage
CENSE II
Spherical PUFF

20.   ABSTRACT (Continued)

add-on to the WES CENSE II series, yielded reasonable radial stress-volume
strain load-release paths for the CENSE II site material. Experimental and
analytical studies of the mutual inductance particle velocity gage indicated
that gage response can be improved by modifying the power supplies and that
emplacing the gages in radial grout columns is acceptable. The analysis was
refined and demonstrated to be capable of calculating stress-strain tra-
jectories accurate to the 5 to 10 percent, given high quality stress and
particle velocity histories from 5 to 8 gage locations. Shear response
calculations are not yet satisfactory, but possible improvements are discussed.
The major conclusion of this effort is that the LASS technique is ready for
field use at sites of interest.

SUMMARY

The objectives of this program are to develop a measurement and analysis method for determining dynamic response of in situ geologic materials and to use the technique to characterize materials at sites of interest to the Defense Nuclear Agency (DNA). The LASS technique (Lagrange Analysis for Stresses and Strains) that has been developed is intended for use in site characterization (material properties determinations) for structural hardness or vulnerability calculations.

The three major activities in this year's work were to:

- Field test the LASS technique in CENSE II, Shots 8 and 9.
- Test and evaluate the performance of the mutual inductance particle velocity (MIPV) gage.
- Evaluate and improve the accuracy of the LASS analysis.

Results of close-in stress measurements on the 100-ton (9.07 Mg) TNT and 120-ton (109 Mg) ANFO Pre Dice Throw events performed as an add-on task to this contract are presented in a separate report.[1]

We performed the first successful field test of the LASS technique as an add-on to Shots 8 and 9 of the U.S. Army Engineers Waterways Experiment Station (WES) CENSE II program. CENSE II : s a series of elevated, surface tangent, partially buried, and buried HE shots performed at a soil site near Hattiesburg, Mississippi. We obtained a 100 percent data return from the ytterbium stess and mutual inductance particle velocity (MIPV) gages in these two shots (see Figures 11-14) and used the LASS analysis to calculate very reasonable radial stress-volume strain trajectories (see Figure 26) for the CENSE II site soil.

We continued development of the MIPV gage by performing both experimental and analytic studies. As part of this development, we participated in a series of small explosive shots performed at the Systems, Science

1

and Software (S^3) test site[*] in which we were able to evaluate MIPV
gage performance in a controlled environment (see Appendix D). We
determined in these tests that signal-to-noise ratio of the MIPV gage
could be significantly improved by shortening the current cables; this
will require modification of the power supplies for remote operation in
the field. To determine the reliability of fielding MIPV gages in radial
grout columns, we performed two-dimensional code calculations for an
end-loaded grout column in soil with several assumed constitutive rela-
tions (Table 3). These calculations showed that the peak particle
velocity in the bottom of the grout column (gage location) closely
approaches the free field soil velocity (Figure 30) and that a density
mismatch of the grout and soil is worse than a modulus mismatch. Calcu-
lated MIPV gage response in grout was judged close enough to free-field
response for LASS analysis purposes.

To evaluate and improve the accuracy of the LASS analysis, we
developed a test problem by assuming constitutive relations (in this
case a variable modulus model fitted to Mixed Company sandstone) and
using them in conjunction with the spherical PUFF code to generate
simulated ideal gage records corresponding to the known constitutive
relations. Using this problem we showed that LASS radial stress-volume
strain trajectories near the center of an instrumented interval calculated
from high quality stress and particle velocity records obtained at 5 to
8 gage stations are accurate to about 5 to 10 percent. Attempts to
calculate the stress difference are not yet successful, but improved
methods are under development.

We conclude that the LASS instrumentation and analysis capabilities
are sufficiently developed and recommend that the LASS technique be used
in a dedicated test at a site of interest to DNA.

---

[*] These shots were part of an S^3 program to model the effects of layered
sites by testing layered concrete beds.

2

PREFACE

CONTENTS

5

ILLUSTRATIONS

78 12 14 003

TABLES

Table

CONVERSION FACTORS FOR U.S. CUSTOMARY TO METRIC (SI) UNITS OF MEASUREMENT

To Convert From	To	Multiply By
angstrom	meters (m)	$1.000\ 000 \times E -10$
atmosphere (normal)	kilo pascal (kPa)	$1.013\ 25\ \times E +2$
bar	kilo pascal (kPa)	$1.000\ 000 \times E +2$
barn	meter^2 (m^2)	$1.000\ 000 \times E -28$
British thermal unit (thermochemical)	joule (J)	$1.054\ 350 \times E +3$
calorie (thermochemical)	joule (J)	$4.184\ 000$
cal (thermochemical)/cm^2	mega joule/m^2 (MJ/m^2)	$4.184\ 000 \times E -2$
curie	giga becquerel (GBq)*	$3.700\ 000 \times E +1$
degree (angle)	radian (rad)	$1.745\ 329 \times E -2$
degree Fahrenheit	degree kelvin (K)	$t_k = (t°f + 459.67)/1.8$
electron volt	joule (J)	$1.602\ 19\ \times E -19$
erg	joule (J)	$1.000\ 000 \times E -7$
erg/second	watt (W)	$1.000\ 000 \times E -7$
foot	meter (m)	$3.048\ 000 \times E -1$
foot-pound-force	joule (J)	$1.355\ 818$
gallon (U.S. liquid)	meter^3 (m^3)	$3.785\ 412 \times E -3$
inch	meter (m)	$2.540\ 000 \times E -2$
jerk	joule (J)	$1.000\ 000 \times E +9$
joule/kilogram (J/kg) (radiation dose absorbed)	Gray (Gy)	$1.000\ 000$
kilotons	terajoules	4.183
kip (1000 lbf)	newton (N)	$4.448\ 222 \times E +3$
kip/inch^2 (ksi)	kilo pascal (kPa)	$6.894\ 757 \times E +3$
ktap	newton-second/m^2(N-s/m^2)	$1.000\ 000 \times E +2$
micron	meter (m)	$1.000\ 000 \times E -6$
mil	meter (m)	$2.540\ 000 \times E -5$
mile (international)	meter (m)	$1.609\ 344 \times E +3$
ounce	kilogram (kg)	$2.834\ 952 \times E -2$
pound-force (lbf avoirdupois)	newton (N)	$4.448\ 222$
pound-force inch	newton-meter (N-m)	$1.129\ 848 \times E -1$
pound-force/inch	newton/meter (N/m)	$1.751\ 268 \times E +2$
pound-force/foot^2	kilo pascal (kPa)	$4.788\ 026 \times E -2$
pound-force/inch^2 (psi)	kilo pascal (kPa)	$6.894\ 757$
pound-mass (lbm avoirdupois)	kilogram (kg)	$4.535\ 924 \times E -1$
pound-mass-foot^2 (moment of inertia)	kilogram-meter^2(kg/m^2)	$4.214\ 011 \times E -2$
pound-mass foot^3	kilogram/meter^3(kg/m^3)	$1.601\ 846 \times E +1$
rad (radiation dose absorbed)	Gray (Gy)†	$1.000\ 000 \times E -2$
roentgen	coulomb/kilogram (C/kg)	$2.579\ 760 \times E -4$
shake	second (s)	$1.000\ 000 \times E -8$
slug	kilogram (kg)	$1.459\ 390 \times E +1$
torr (mm Hg, 0°C)	kilo pascal (kPa)	$1.333\ 22\ \times E -1$

* The becquerel (Bq) is the SI unit of radioactivity; 1 Bq = 1 event/s.

† The Gray (Gy) is the SI unit of absorbed radiation.

10

1. INTRODUCTION

Since 1971 SRI has participated in an ongoing program for the Defense Nuclear Agency (DNA) to determine dynamic in situ constitutive properties of soils and rocks at sites of interest to DNA. The program has involved effort in three areas:

- Development of ground motion instrumentation in the stress range from 0.1 to 3.0 GPa.
- Development of a spherical Lagrange analysis.
- Field testing.

The program has produced a new site characterization method called the LASS technique (Lagrange Analysis for Stresses and Strains) which draws upon results from each of the above areas. In this technique field measurements of soil or rock motion induced by spherical explosive loading are combined with a Lagrange flow analysis to obtain dynamic in-situ stress-strain trajectories for site material.

This report describes progress from September 1974 to March 1975. Results of an add-on task to make close-in stress measurements on the 100-ton (90.7 Mg) TNT and 120-ton (109 Mg) ANFO Pre Dice Throw events, also performed under this contract, are presented in a separate report.[1]

PROBLEM

The vulnerability of structures to near surface detonations can be assessed by calculating the airblast, ground motion, cratering, and soil-structure interactions induced by the event. However, for partially contained detonations and for complicated site geologies and materials, code predictions of the ground motion, cratering and soil-structure interactions phenomena often do not agree with field measurements. The discrepancies are usually attributed to inadequacies in

11

the constitutive relations used to model the site in the calculations. Shear behavior in yielding is particularly uncertain.

Data for constructing constitutive models have traditionally been obtained from various laboratory studies of cores taken from vertical drill holes. However, such tests have three well-known limitations: (1) specimens are usually too small to include representative distributions of cracks, voids, flaws, and joints, which strongly affect ground motion at real sites; (2) the environmental conditions of the test such as prestress and moisture content may differ significantly from those prevailing in situ; and (3) strain rates are often not close to those encountered in large detonations.

Various computational and experimental approaches have been tried either to determine the relative importance of these limitations or to provide correction factors. The approaches include code studies of parameter sensitivity, laboratory rate dependence and prestress tests (usually with small specimens), in situ quasi-static flat jack tests, and the use of larger, faster laboratory mechanical testing devices. In spite of such efforts, the constitutive relations for in situ material under dynamic loading remained a major uncertainty in ground motion, cratering, and vulnerability calculations.

What is needed is a technique for obtaining site material response information under field event conditions. Ideally the measurements should be made with representative specimens of site material comparable in size to the wavelengths expected in the actual event, in the in situ environment, and at the loading rates expected in the event.

APPROACH

The SRI approach for determining site constitutive properties applicable to modeling field events uses an analysis technique called LASS. A

12

moderate size buried spherical[*] high explosive (HE) charge (typically 100 to 500 kg of TNT) is used to load the in situ site material. The resulting deformation within a region of several cubic meters is recorded by a series of radial stress and radial particle velocity field gages. The gage ranges are chosen so that, typically, peak radial stresses are between 0.1 and 2.5 GPa and peak particle velocities are between 20 and 300 m/s. This transition region between the elastic and hydrodynamic response regimes is important in free-field ground motion calculations. The field measurements are then used in a Lagrange flow analysis (LASS) to numerically solve the partial differential equations expressing conservation of mass and momentum for spherical flows. The results are the stress-strain trajectories of in situ particles (mass elements) under dynamic spherical loading. Details of the technique are given in Section 2.

This approach does not suffer from the three limitations of laboratory tests listed above. In addition no assumptions concerning the thermodynamic nature of the flow or the form of the constitutive relations are required to perform the LASS analysis. Since the results are stress-strain trajectories, they are in a convenient form for use in constructing constitutive models. The approach is applicable to other flow geometries, such as uniaxial or cylindrical, and to other stress ranges, both higher and lower than that we have investigated to date. The limitations of the present LASS analysis and the supporting in situ tests are: (1) the shot must be performed in site material that is sufficiently homogeneous and isotropic for the flow geometry to remain essentially spherical, (2) partial derivatives with respect to position must be estimated from a limited number of gage records, and (3) gage records from field events are often so noisy that accurate analysis is difficult.

Another in-situ approach for determining site constitutive relations is the CIST (cylindrical in-situ test) technique developed for DNA and

---

[*] The technique is also applicable to cylindrical and planar charges.

13

SAMSO by the Air Force Weapons Laboratory (AFWL). In their present

forms LASS and CIST results are complementary since CIST provides

data at low stresses (below 100 MPa) and for cylindrical loading

(the CIST source is typically a 40-foot-long (12.2 m) primacord rack in

a 2-foot-diameter (0.6 m) hole). A major difference between the approaches

is that at present the CIST instrumentation consists of arrays of accel-

erometers rather than stress and particle velocity gages used in the

LASS technique; consequently, CIST results are analyzed by assuming

a form for the site constitutive relations and iteratively adjusting

the free parameters until recorded accelerometer histories or their

integrals is obtained. The LASS approach, on the other hand, is to

start from the flow equations and make the measurements necessary to

solve them. Another major difference between CIST and LASS is that in

a strongly layered site the CIST HE cylinder and instrumentation will

usually span several zones, while the LASS measurements will be made

within a single zone. Therefore CIST provides integrated site response

information and LASS provides detailed response information for individual

layers.

PREVIOUS RESULTS

Previous work in the SRI in situ properties program and related

areas has been described in a series of DNA reports[1-12] summarized in

Appendix A. Major milestones (see Appendix A) were the proposal of the

LASS concept and the demonstration of its feasibility,[2] the development

of ytterbium stress gages and mutual inductance particle velocity gages

to the status of working field gages,[3-6] the subsequent use of ytterbium

stress gages to make ground motion measurements for DNA in a number of

nuclear and HE events,[1,7,9-12] and the development of the spherical

LASS analysis to its current code form in which it can calculate stress-

strain trajectories for complex time dependent flows.[2,4-6]

14

REPORT ORGANIZATION

Section 2, describes the LASS shot configuration, the instrumenta-
tion used to obtain field measurements, and the spherical Lagrange
analysis. It may be omitted by a reader familiar with the LASS technique.
Section 3, presents the findings from the LASS CENSE II field test, the
gage development, and the analysis modification and evaluation. Section
4, gives our assessment of the current status of the LASS technique and
our recommendations for further work.

2. METHODS

This section describes experimental and analytic aspects of the LASS technique, a method for determining dynamic mechanical properties of in situ site material. Topics discussed are shot configuration and scale, radial stress and radial particle velocity field gages, and the spherical Lagrange analysis. Much of this information has been presented in previous SRI reports (see Appendix A).

LASS EXPERIMENTS

The objectives in a LASS shot are to induce dynamic spherical deformation of in situ site material and to measure the resulting radial stress and radial particle velocity histories on a number of particle paths (Lagrange coordinates). As will be shown later, these measurements are sufficient to permit calculation of the stress-strain trajectories taken by the in situ site material during the spherical deformation.

The configuration of a typical LASS shot is shown in Figure 1. It consists of a spherical HE (high explosive) charge embedded in the site layer of interest and surrounded by a number of radial stress and radial particle velocity gages also embedded in the layer at various distances from the charge center. The essential features to note are: the spherical geometry of the initial configuration, the positioning of the test away from adjoining site layers to preserve the spherical symmetry of the flow during the measurement interval, and the measurement of two independent flow variables, radial stress and radial particle velocity, at a number of Lagrange coordinates (initial distances from the charge center).

16
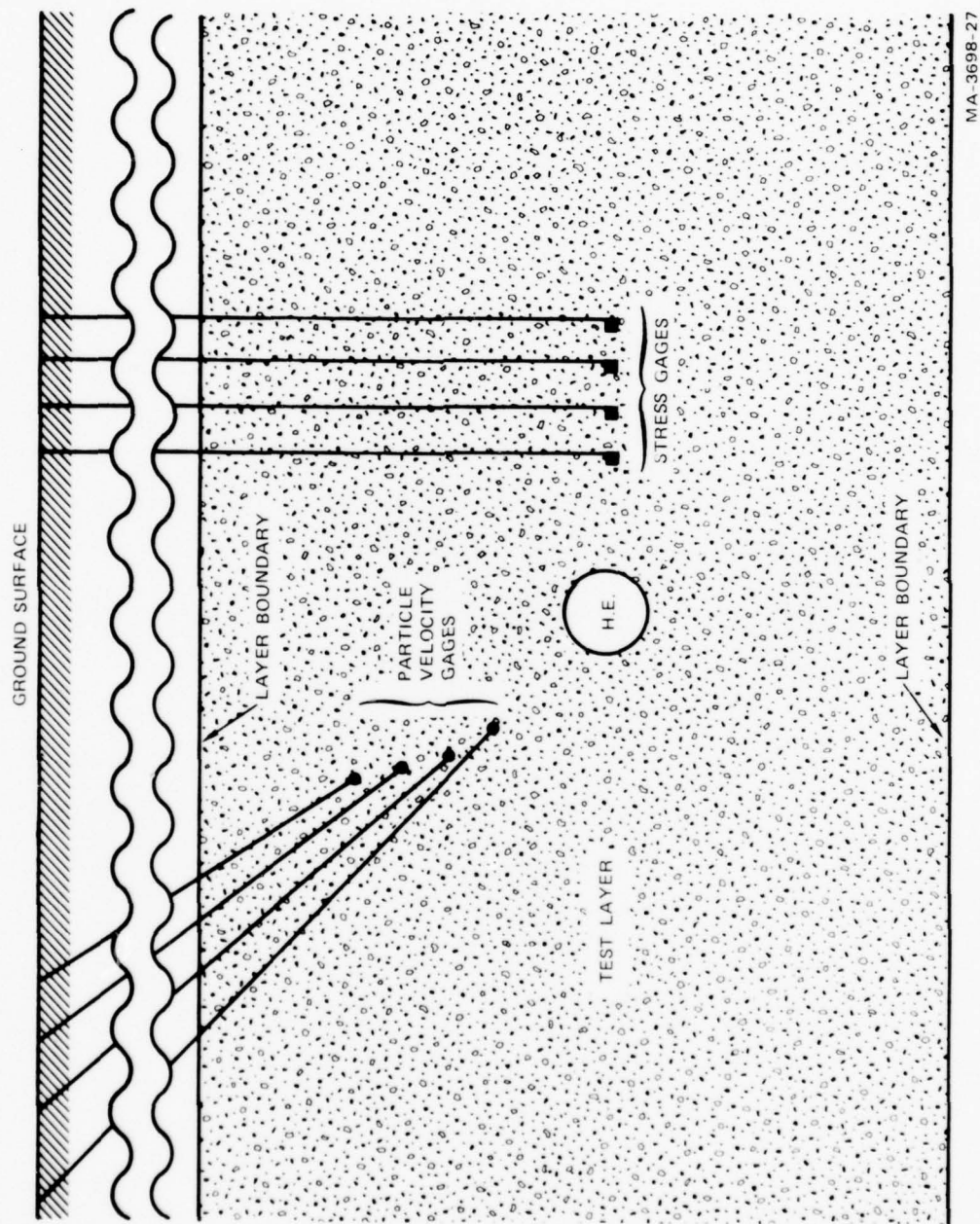
FIGURE 1   TYPICAL LASS SHOT CONFIGURATION

GROUND SURFACE

LAYER BOUNDARY

PARTICLE VELOCITY GAGES

STRESS GAGES

H.E.

TEST LAYER

LAYER BOUNDARY

MA-3698-27

It is worth emphasizing that there are two necessary, but not sufficient, conditions to be satisfied if gage data from a LASS shot are to provide valid input for the Lagrange analysis. First, the flow symmetry must correspond closely to that assumed in the analysis, (spherical in the present case) in the gage region during the measurement interval.* Therefore shots should be performed in site layers that are isotropic and homogeneous on the scale of the test dimensions, and field gages should be positioned to test for deviations from the assumed flow. Second, the gages must be Lagrangian; that is, they must move with the flow (along particle paths) and not significantly perturb it. It is up to the experimenter, after considering such factors as the stress range of interest and the specific site geology (competent rock, dry or wet soil, etc.), to choose gage designs and emplacement procedures that will lead to this condition being met. Field gage designs are discussed later in this section.

The scale of a LASS shot, that is, the HE source magnitude and the source to gage distances, are determined by the stress range of interest and the size and nature of the site region being characterized. The scale of the experiment is chosen either to stay within the geologic inhomogeneity, such as a soil layer, and measure the constitutive properties of the layer, or to span numerous inhomogenities, such as the joints of a rock site, and measure their averaged properties. Our measurements to date for DNA have been in the 0.1 to 2.5 GPa stress range in which soft sites compact and stiffen and hard sites yield. Gage spacing has typically been one-half to several meters and charge sizes in the 10 to 1000 Kg range.

---

*
Lagrange analyses have been developed for uniaxial flows and can be extended to cylindrical flows.

18

FIELD GAGES

Stress Gages

To measure radial stresses, we use piezoresistive gages with ytterbium as the active element. A 6 to 25 ohm photoetched ytterbium grid with its associated coaxial cable forms one arm of a bridge circuit. The incident stress wave changes the resistance of the grid, which produces a bridge imbalance proportional to the change in gage resistance. The bridge is calibrated by adding known resistors in series with the gage to simulate stress induced resistance changes.

The packaging of the ytterbium grids has evolved as two generic types, paddles and epoxy cylinders, shown in Figure 2. The paddle configuration consists of the ytterbium grid sandwiched between two thin plates, usually pieces of commerical epoxy/fiberglass board, with a tube as a handling fixture. These gages are usually installed in holes that are tangent to a wave front, that is, the axes of the holes are perpendicular to the direction of wave propagation. Gage 157 in Figure 2 is an example of a used paddle gage; the aluminum tube was destroyed by the shot. Paddle 165 shows another packaging material--6-mm sheets of homolite epoxy. Since the paddle configuration is "thin" in the direction of wave propagation, it will rapidly come into equilibrium with the surrounding stress field. Its disadvantage is that minor amounts of tangential strain may pull the gage apart.

MA-3698-28

FIGURE 2   YTTERBIUM STRESS GAGES.
Two cylindrical radial stress gages
and two paddle gages.

20

For long recording times we developed cylindrical epoxy packages
that are grouted into radial drill holes. Two examples are shown in
Figure 2. The gages are cylinders of epoxy about 75 mm in diameter and
75 mm long. The grid is parallel to and about 6 mm from the front face;
the coaxial cable exits from the rear. This gage type works well with
slowly rising stress pulses (>500 µs) where there is sufficient time for
numerous reverberations to occur and bring the epoxy cylinder into stress
equilibrium with the surrounding flow. Note that on small scale experi-
ments with rapid rise times, the stress measured in the epoxy will not
be equal to that in the surrounding flow until enough reverberations occur
to bring about equilibration. The gage package should be installed close
to the bottom of the radial hole so that one does not have a long cylinder
of grout in front of the gage; the effect of such a grout cylinder is
considered further in the next section on particle velocity gages.

Currently, with ytterbium stress gages, we are able to record waveforms
to near zero stress with accuracies in peak stress estimated to be about
±5 percent. The calibration is less reliable near zero stress because
the state of strain experienced by the grid in the field can be different
from that in the gas gun calibration work. Also, there are often dips
and spikes in the unloading profiles that we are unable to interpret.

Particle Velocity Gages

We measure particle velocity with the mutual inductance particle
velocity (MIPV) gage. This gage, described in detail in references
3 through 5 consists of rectangular coils of wire that are deformed by
the passage of the stress wave. A simplified two-coil version is
diagrammed in Figure 3. The deformation causes a change of mutual
inductance between the coils that is directly related to the particle
velocity.

21

PRESENT POSITION
OF SHOCK FRONT

LAGRANGIAN POINT
AT WHICH PARTICLE
VELOCITY IS MEASURED

CURRENT LOOP

U

u

SENSOR LOOP

x(t)
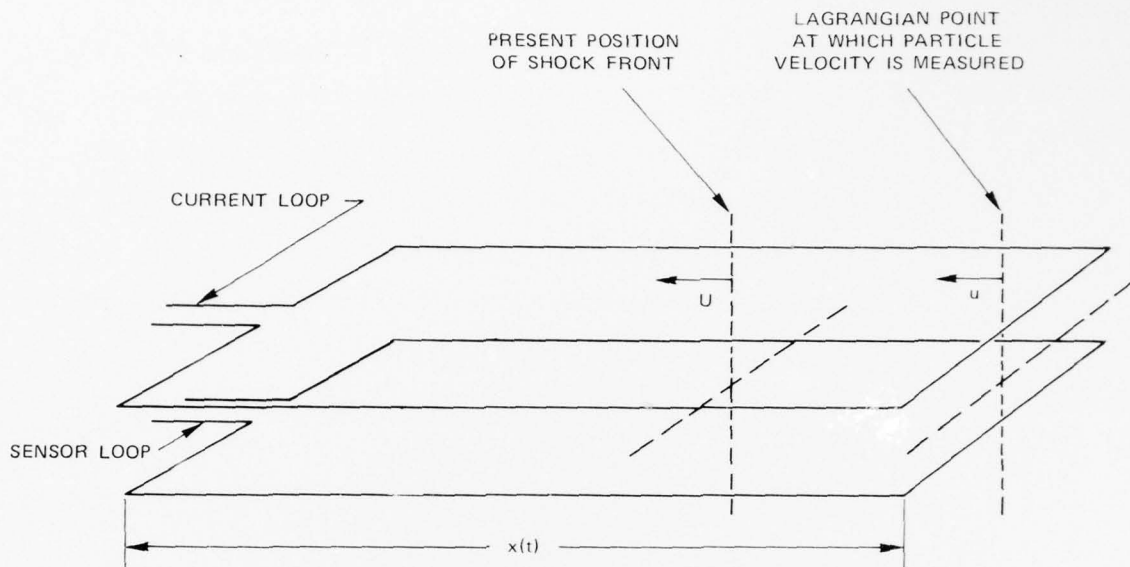
GA-8567-37A

FIGURE 3   GEOMETRY FOR TWO-TURN MIPV GAGE
U is the shock velocity and u is the particle velocity.

The MIPV gage originated at Engineering Physics Company (EPCO), which fielded versions of it on the nuclear shot Red Hot and on the large HE shot Distant Plain.[13] Early in the in situ program we reviewed "off the shelf," prototype, and "potential" particle velocity gages. No commercially available gages covered the 50 to 300 m/sec range of interest to us. Most of the "potential" gage concepts, such as radar reflectance, had serious shortcomings. The EPCO MIPV gage, still in the category of a prototype because only limited development work and field use had been carried out, offered the best promise in the relatively high velocity range of interest. Over the past few years, we have analyzed the MIPV gage concept, tested small versions of the gage in our gas gun (where we can independently measure the particle velocity), developed

22

calibration techniques, and used several version of the gage in small scale HE experiments and in several full-scale field tests. Additional work on the MIPV gage has also been performed at the Air Force Weapons Laboratory.[14,15]

The operation of the gage may be understood from the following description based on the simplified two-turn gage shown in Figure 3. The two rectangular coils are placed so that the direction of wave propagation is parallel to the long axis of the loops. One loop carries current; the second is the pickup loop. From electromagnetic theory the voltage $\mathcal{E}$ induced in the pickup is related to the change of flux Φ linking the two circuits by

$$\mathcal{E} = -\frac{d}{dt}\,\Phi = -\frac{d}{dt}\,(MI) \tag{1}$$

where the flux has been equated to the product of the mutual inductance M and the current I. With the current held constant and assuming axial motion only, we may write

$$\mathcal{E} = -I\,\frac{dM}{dt} = -I\,\frac{dM}{dx}\frac{dx}{dt} \tag{2}$$

where x is the axial coordinate of the end of the gage. When the impacted end of the gage equilibrates with the surrounding flow, the time rate of change of the axial coordinate equals the soil particle velocity, u. Thus

$$\mathcal{E} = -I\,\frac{dM}{dx}\,u \tag{3}$$

We have shown previously[5] that for a properly designed gage the change of mutual inductance with displacement may be treated as a gage constant. Therefore, by measuring the induced voltage $\mathcal{E}$ and the steady state current I, we can solve Eq. (3) for the particle velocity u. In practice the MIPV gage is composed of more than two loops; however the same transduction principles apply.

Because of its geometry, the MIPV gage must be installed in a radial hole, like the epoxy cylinder stress gage. Since the gage is grouted in this radial hole, we are actually measuring particle velocity in the grout. If the grout is well matched to the site material, we can claim that the measurement is close to the actual free field measurement. In this year's program we used a two-dimensional code to analyze this problem (see Section 3) and showed that, for a gage close to the end of a drill hole and a 20 percent to 30 percent mismatch of mechanical impedance of the grout and host material, the peak gage output is still within 5 percent of the free field particle velocity.

Our recent progress on this gage is as follows. On the earlier two Essex programs we obtained some useful measurements; however survival and noise problems were encountered.[5] In this years CENSE II program (see Section 3 and Appendix B) all gages survived, but with some noise. In the joint work with Systems, Science and Software, described in Appendix C, we obtained full survival and clean records; however, these shots did not involve the many thousands of feet of signal and power leads that are common in field tests.

LAGRANGE ANALYSIS FOR SPHERICAL FLOWS

The spherical LASS analysis calculates site material stress-strain trajectories from field measurements of radial stress and radial particle velocity. The approach is to use the field measurements in conjunction with finite difference methods to solve the partial differential equations defining strains and expressing the conservation of mass and momentum for spherical flow. The importance of the LASS method is that no assumptions whatsoever are required concerning the thermodynamic or mechanical constitutive relations of the material. Consequently the accuracy of the calculated stress-strain trajectories is limited only by the validity of the finite difference approximations for the partial derivatives and by the experimental errors in the field measurements. The LASS stress-

24

strain trajectories therefore provide convenient, unambiguous data for use in selecting a mathematical site material model or for evaluating the free parameters in such a model.

The current form of the LASS analysis was described in reference 5. For spherical flow the equations expressing conservation of mass and momentum in Lagrange coordinates are

$$\frac{\rho_o}{\rho} = \frac{r^2}{h^2} \left(\frac{\partial r}{\partial h} \right)_t \tag{4}$$

$$-\rho \left(\frac{\partial u_r}{\partial t} \right)_h = \left(\frac{\partial \sigma_r}{\partial h} \right)_t \left(\frac{\partial r}{\partial h} \right)_t^{-1} + 2 \frac{\Phi}{r} \tag{5}$$

where:

   stresses are taken as positive in compression

   ρ_o and ρ are the initial and present densities

   r is the Eulerian radial coordinate

   h is the Lagrange coordinate of a particle, i.e., its
      initial radial coordinate

   t is time

   u_r and σ_r are radial particle velocity and radial stress

   Φ is stress difference, $\sigma_r - \sigma_t$ (the difference between
      radial and tangential stress).

The definition of radial particle velocity as the time rate of change of Eulerian particle position provides a third flow equation, which may be written in differential or integral form

$$u_r = \left(\frac{\partial r}{\partial t} \right)_h \tag{6a}$$

or

$$r = h + \int_{T_0(h)}^{t} u_r(h, \tau) \, d\tau \tag{6b}$$

25

Where $T_0(h)$ is the time of first motion of the particle h.

Thus we have five flow variables, σ_r, u_r, ρ, r, and Φ, each a function of h and t, related by three equations, (4)-(6). Not all are independent, however. If two are selected that are independent, and if these are measured over some h-t domain, the remaining three variables can be calculated over the same domain by simultaneously solving the system of equations. Inspection of the equations shows that any of the seven pairs that can be formed from σ_r, Φ, and one of the remaining three variables is mathematically sufficient to solve the three equations. However, no experimental techniques are now available for measuring Φ, so four of the seven pairs can be eliminated. Early in the development of the LASS technique, we decided to measure particle velocity rather than density or displacement. Consequently we developed the LASS analysis to solve Eqs. (4)-(6) based on field measurements for σ_r and u_r. Because the field measurements constitute time series for these variables at various discrete particles, h_i, rather than a complete specification throughout an h-t domain, the analysis uses statistical interpolation methods and finite difference techniques to solve Eqs. (4)-(6).

To provide stress-strain trajectories, the analysis further calculates strain histories from the displacement field r(h,t). The following definitions are used for radial strain ϵ_r, tangential strain ϵ_t, and volume strain ϵ_v:

$$\epsilon_r = 1 - \left(\frac{\partial r}{\partial h}\right)_t \tag{7}$$

$$\epsilon_t = 1 - \frac{r}{h} \tag{8}$$

$$\epsilon_v = 1 - \frac{r^2}{h^2}\left(\frac{\partial r}{\partial h}\right)_t = 1 - \frac{\rho_o}{\rho} \tag{8}$$

26

The first step in the analysis is to use the field records $\sigma_r(h_i,t)$ and $u_r(h_i,t)$ to create analytic representations, which we call gage flow surfaces, for the σ_r and u_r surfaces over the h-t domain spanned by the measurements. The field records are equivalent to paths on these surfaces along which the parameter h assumes various constant values as shown schematically in Figure 4.

The major problem in creating accurate representations of the gage flow surfaces is the high level of noise and other anomalies often present in field records. This well-known and often lamented effect is an inherent property of field measurements, reflecting both the difficulty of making precise measurements outside the laboratory and also the numerous geologic inhomogeneities present in real sites. To handle the problem of possible unknown error in an individual measurement, we use all the gage measurements in establishing the flow surface amplitude at specific h_i, t coordinates. Having thus created a globally averaged mathematical representation of the gage flow surface, we can then generate more reliable estimates of individual records as needed to solve Eqs. (4)-(9). This technique is more circuitous than using the field records directly, but it significantly improves the accuracy of the calculations and is computationally convenient.

The present LASS procedure for creating the two globally averaged gage flow surfaces consists of three steps. First, the significant flow features on each record are identified and labeled. Significant features are those clearly identifiable in the majority of the records, such as precursor foot, a plastic wave peak, a point at which decay rate changes rapidly, or simply a specific percentage of peak amplitude for a smooth featureless profile. Second, since the many other features usually present in field data are not deemed statistically significant, the labelled features on each individual record are connected by straight line segments to produce piecewise linear gage history representations as shown in Figure 5. Finally, to interpolate between Lagrange measurement

27
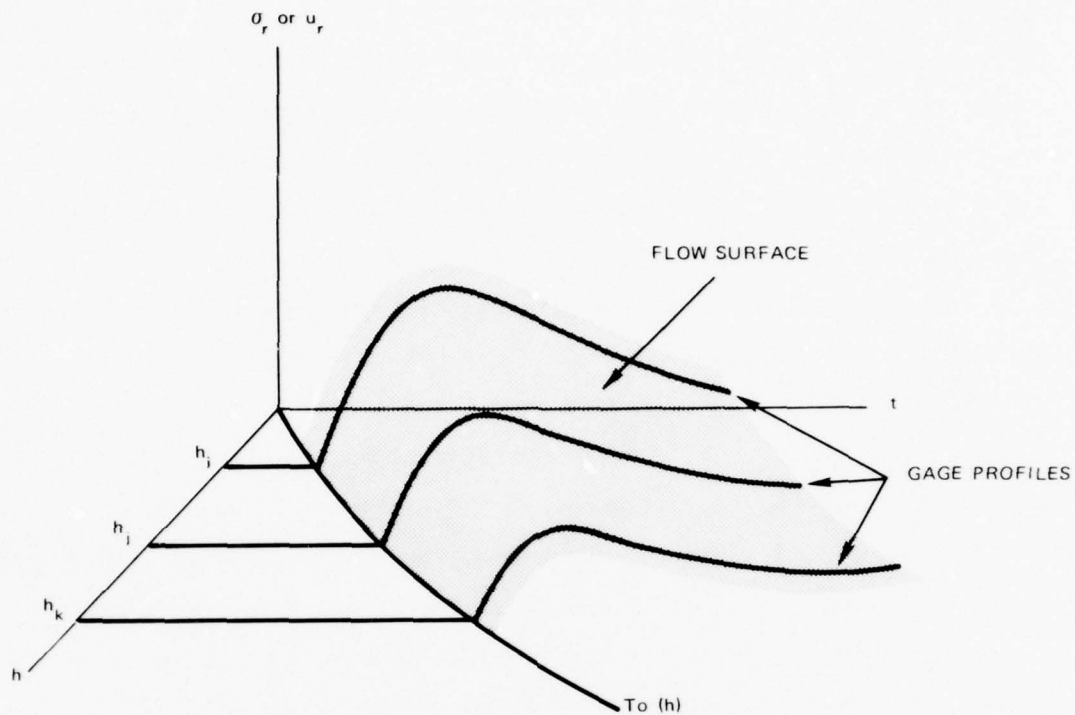
MA-1620-2C

FIGURE 4   GAGE FLOW SURFACE

The in-material gage profiles provide traces on this surface
and are used to approximate the surface.
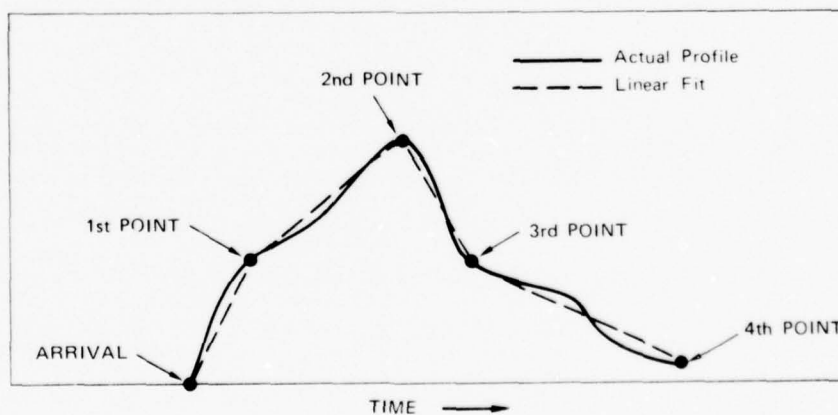
MA-2331-27A

FIGURE 5   PIECEWISE LINEAR REPRESENTATION OF GAGE RECORD

Points shown are parameters that were selected as best
characterizing the data.

locations h_i and to provide the global averaging discussed earlier, we link the amplitude coordinates and the time coordinates at each discrete position h_i for each feature such as peak stress, with smooth functions of h. A hypothetical peak stress amplitude versus h linking is shown in Figure 6. Of course, a time versus h linking for this feature is also necessary to complete specification of the peak stress locus on the gage flow surface. Linear or quadratic exponential functions are generally used for the h-linking:

$$
\left\{ \begin{array}{c} \text{amplitude} \\ \text{or} \\ \text{time} \end{array} \right\} = \left\{ \begin{array}{l} e^{\alpha+\beta h}, \text{ linear exponential fit} \\[2ex] e^{\gamma+\delta h+\lambda h^2}, \text{ quadratic exponential fit} \end{array} \right.
$$

Where α and β are constants created by the linear least squares fit, and γ, δ, and λ are constants created by the quadratic least squares fit. A different set (α,β) or (γ,δ,λ) is generated for each amplitude and each time link line.

The fitted link lines in conjunction with the piecewise linear form for gage records generate the gage flow surface representations shown schematically in Figure 7. With these representations for the stress and particle velocity flow surfaces, solutions of equations (4)-(9) proceed by numerical application of the exterior derivative or path line analysis approach described by Grady.[4] The accuracy of the current LASS analysis, namely, the piecewise linear constant-h trace, the globally averaged link lines, and the path line approach, was examined in this year's work using the test problem described in Section 3. Strain calculations were shown to be accurate to within 5 to 10 percent near the center of the h interval given a realistic number (5 to 8) of high quality gage records. This is judged very satisfactory performance for an analysis designed to accept very noisy field data.

29

RADIAL DISTANCE, h
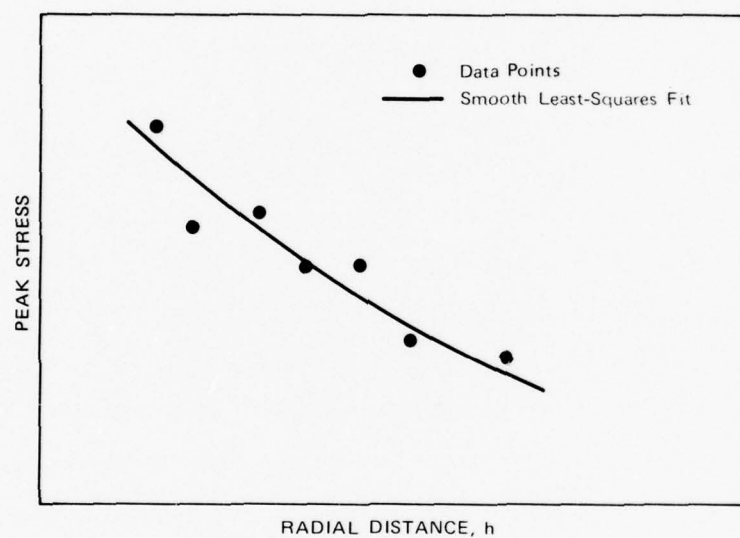
MA-2331-28A

FIGURE 6   AMPLITUDE-h LINK LINE FOR PEAK STRESS

This is an example of a link line generated to describe
the spatial variation of one of the characteristic points
(in this case, peak stress) from the piecewise linear
representation of the stress records.

σ_r or u_r

2nd LINK LINE

3rd LINK LINE

4th LINK LINE

PIECEWISE LINEARLY
APPROXIMATED GAGE
RECORDS

ARRIVAL
LINE

h

1st LINK LINE

MA-2331-29A
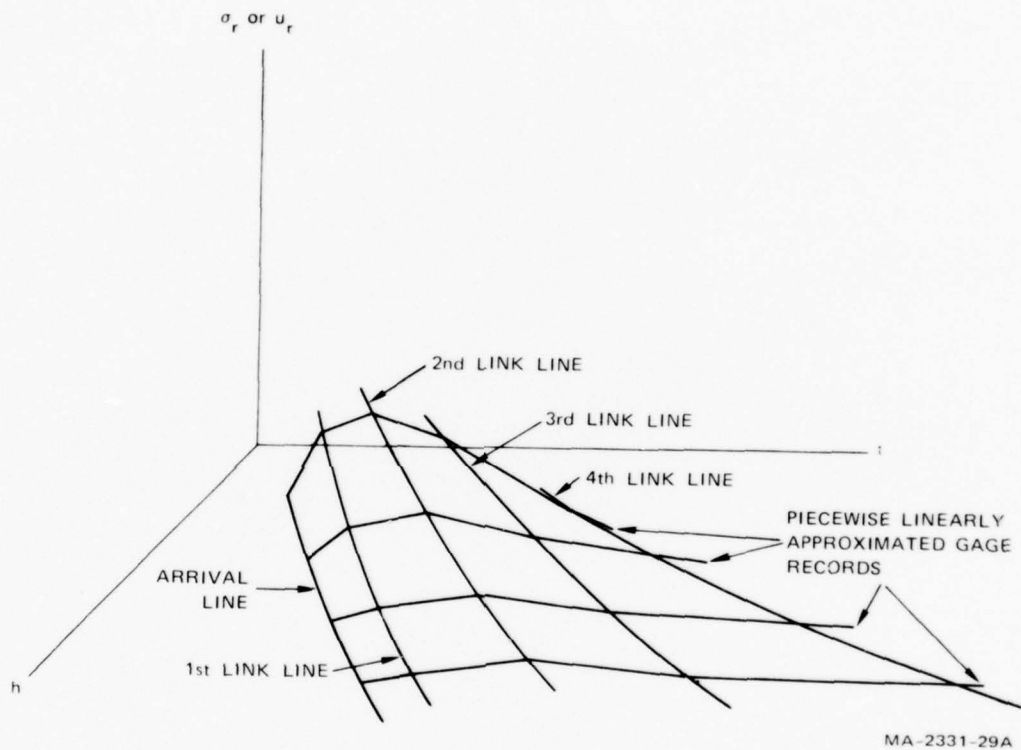
FIGURE 7   GAGE FLOW SURFACE REPRESENTATION

Determined from the experimental data by selecting parameters that best describe
the character of the flow within the quality of the data.   Note that gage records
are piecewise linear and that link lines are smooth.

31

As pointed out previously,[4-6] Φ is much more difficult to calculate than are the strains because Φ is typically a small quantity and it appears in Eq. (5) as the difference of two large derivatives. Although attempts to calculate Φ using field data have not yet provided reasonable results, during the coming year we expect to determine the feasibility of modifying the computational approach (see Section 4) to improve the Φ calculation.

3. RESULTS

During the period of this report we field tested the LASS technique in conjunction with the Waterways Experiment Station (WES) CENSE II program, performed computational and experimental tests of the MIPV field gage, and modified LASS and tested its accuracy. Results are presented below.

CENSE II

CENSE is a WES program to study the coupling effects of near surface explosions. High explosive shots are fired at various charge radii above, at, and below the surface, and the energy coupled into the ground is measured. CENSE I was carried out in 1973 at the DNA Mixed Company Site in Colorado where the geology was soft rock (sandstone). CENSE II was conducted in the late fall of 1974 at Camp Shelby, near Hattiesburg, Mississippi, where the geology was soil.

SRI participated in Shots 8 and 9 of the CENSE II series. These were buried shots 8 and 12 charge radii (2.2 and 3.3 m) below the surface and provided a good opportunity for us to try the LASS technique in the field. We also participated on Shot 5, a surface-centered shot, to provide high amplitude data for WES and to evaluate our field gage techniques. Shot 5 was not ammenable to the LASS analysis because the flow was not spherically symmetric; it is discussed in Appendix B.

The WES crew described the geology of the CENSE II site as uniform sandy clay soils characteristic of Southern pine woods. Drill cuttings from holes to 6 m showed no visible change from the near surface red to yellowish material. Enough clay was present that 45° slant holes

33

showed clean uniform sides. The water table was at a depth of about 7.5 m, well below our test region.

Instrumentation

The test geometry for Shots 8 and 9 is shown in Figure 8. The cast TNT spheres weighed 136 kg and were 0.55 m in diameter. The charges were grouted in the bottoms of slightly oversize holes. The grout, also used to emplace the gages, was a version of the ESSEX E2D grout altered to reflect the softer soil at this site.

Two lengths of mutual inductance particle velocity (MIPV) gages were used in these shots--0.51-m gages close to the source and 1.02-m gages farther out, as listed in Table 1. The length of the gage governs the recording time. Therefore, since the rise time will increase with increasing distance from the source, longer gages are required further out to record at least the rise to peak and the first part of the decay. Figure 9 shows an unused 1.02-m gage and a recovered 0.51-m gage.

The MIPV gages were grouted in 127-mm-diameter drill holes inclined at 45° to the surface. (The original request was for 76-mm-diameter holes but a 76-mm drill was not available at the site.) The bare gages, as shown in Figure 9, were grouted in position; this differs from previous use where we grouted the gages into cylindrical tubes in the laboratory and then, in the field, grouted the tubes into the drill holes. We made this change to circumvent problems encountered in the Essex series, where the grout in the tubes dried out in the time between original grouting and field installation causing impedance mismatches and early gage failure.

If 76-mm holes had been available, the MIPV gages would necessarily have been positioned nearly symmetrically in the bore as shown in Figure 10(a).

34

GROUND SURFACE

45°

GROUT

BACK
FILL

GROUT

GROUT

MIPV GAGES
AND CYLINDRICAL
STRESS GAGES

• • •

STRESS GAGES
(paddles)

136-kg
CAST TNT
SPHERE
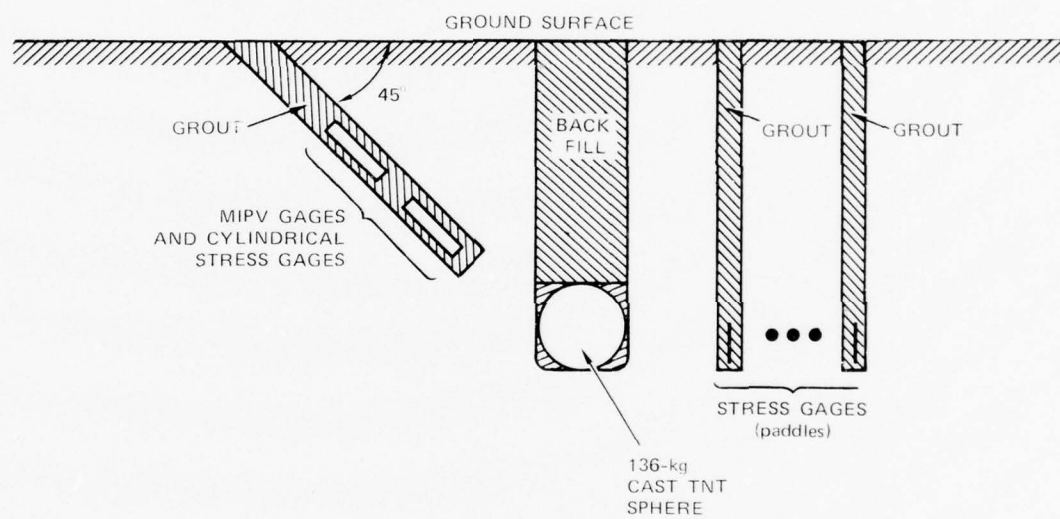
MA-3698-29

FIGURE 8   SHOT GEOMETRY FOR CENSE II, SHOTS 8 AND 9

Table 1

GAGE LOCATIONS FOR CENSE II, SHOTS 8 AND 9

Gage Number	Radial Distance (m)	Notes
Shot 8, ytterbium stress gages		
S1	0.716	Radial gage, angled hole (8D)
S2	0.762	Fiberglass paddle, vertical hole
S3	0.951	Epoxy paddle, vertical hole
S4	1.44	Fiberglass paddle, vertical hole
S5	1.55	Radial gage, angled hole (8A)
Shot 8, particle velocity gages		
P6	0.689	0.51-m gage, angled hole (8A)
P7	0.762	0.51-m gage, angled hole (8B)
P8	0.884	1.02-m gage, angled hole (8C)
P9	1.10	1.02-m gage, angled hole (8D)
P10	1.65	1.02-m gage, angled hole (8B)
Shot 9, ytterbium stress gages		
S1	0.716	Radial gage, angled hole (9D)
S2	0.777	Fiberglass paddle, vertical hole
S3	0.945	Epoxy paddle, vertical hole
S4	1.40	Fiberglass paddle, vertical hole
S5	1.63	Epoxy paddle, vertical hole
Shot 9, particle velocity gages		
P6	0.689	0.51-m gage, angled hole (9A)
P7	0.765	1.02-m gage, angled hole (9B)
P8	0.884	1.02-m gage, angled hole (9C)
P9	1.10	1.02-m gage, angled hole (9D)
P10	1.57	1.02-m gage, angled hole (9A)

MA 3698-30

FIGURE 9   MIPV GAGES FOR CENSE II, 0.51 m GAGE (USED) AND 1.02 m GAGE (NEW)

37

(a)

SOIL

DRILL HOLE FILLED
WITH GROUT

WAVE FRONT WITH
GROUT VELOCITY
LESS THAN SOIL
VELOCITY

MIPV
GAGE

WAVE FRONT WITH
GROUT VELOCITY
LARGER THAN SOIL
VELOCITY

(b)

SOIL

DRILL HOLE FILLED
WITH GROUT

WAVE FRONT WITH
GROUT VELOCITY
LESS THAN SOIL
VELOCITY

MIPV
GAGE

WAVE FRONT WITH
GROUT VELOCITY
LARGER THAN SOIL
VELOCITY
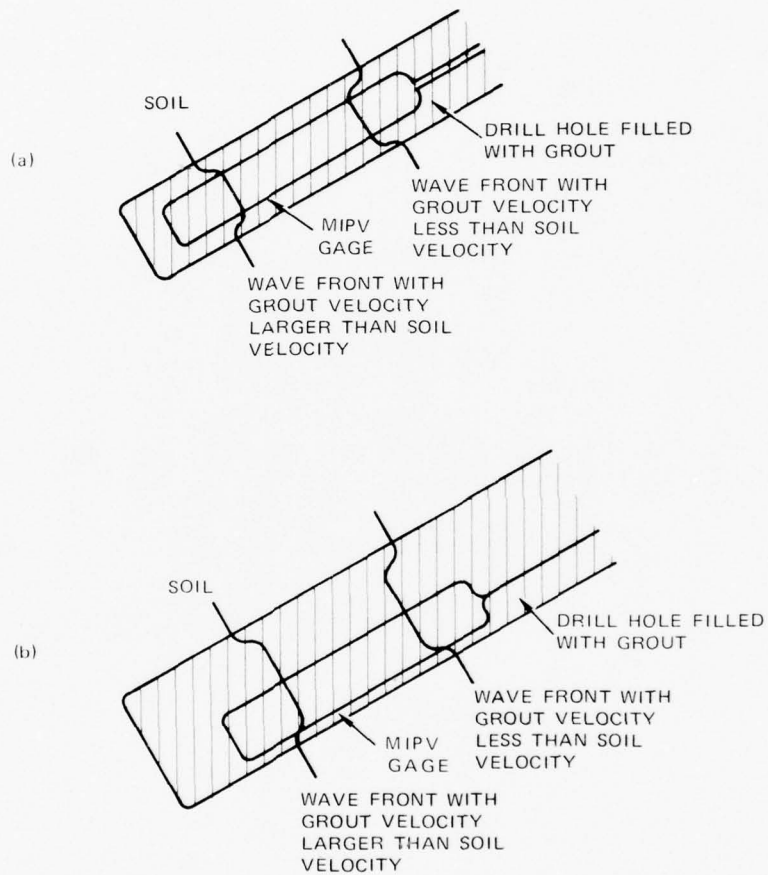
MA-3698-31

FIGURE 10   LOCATIONS OF MIPV GAGES

(a) Centered in small drill hole and (b) Off-center
in large drill hole

38

However, when emplaced in 127-mm holes, the MIPV gages probably laid well off the central axis in the nonsymmetrical position shown in Figure 10(b), and possibly were tilted with respect to the hole axis in addition. Effects of such nonideal emplacement on gage output are unknown.

Both paddle and cylindrical stress gages were used. The paddle gages were located in vertical drill holes, the cylindrical gages were installed in radial holes. Gage locations are given in Table 1. Because of the cost to drill the radial (45°) holes, we placed several gages in each hole. Although this technique opens the question of waves propagating in a radial grout column, we believed it useful to examine the possibilities of this approach.

Measurements

Figures 11 through 14 show the stress and particle velocity profiles obtained in CENSE II, Shots 8 and 9. These profiles were reduced using standard calibration procedures from raw voltage-time data recorded by the oscilloscopes. To aid the reader in interpreting the profiles in Figures 11 through 14, we discuss significant or anomalous features of the individual records in Appendix C. Note that temporary losses of gage signal are indicated in these figures by flat-topped regions of arbitrary height.

Peaks and times of arrival from the profiles in Figures 11 through 14 are given in Table 2. Figure 15 shows time of arrival versus distance. Except for gages beyond 1.5 m, the data cluster well. Peak stress versus distance data are shown in Figure 16 along with hand-fitted attenuation lines. Stress attenuates slightly faster for Shot 8 than for Shot 9.

Summarizing the field measurements we see that every stress gage produced a record and that in most cases the records were credible and

39
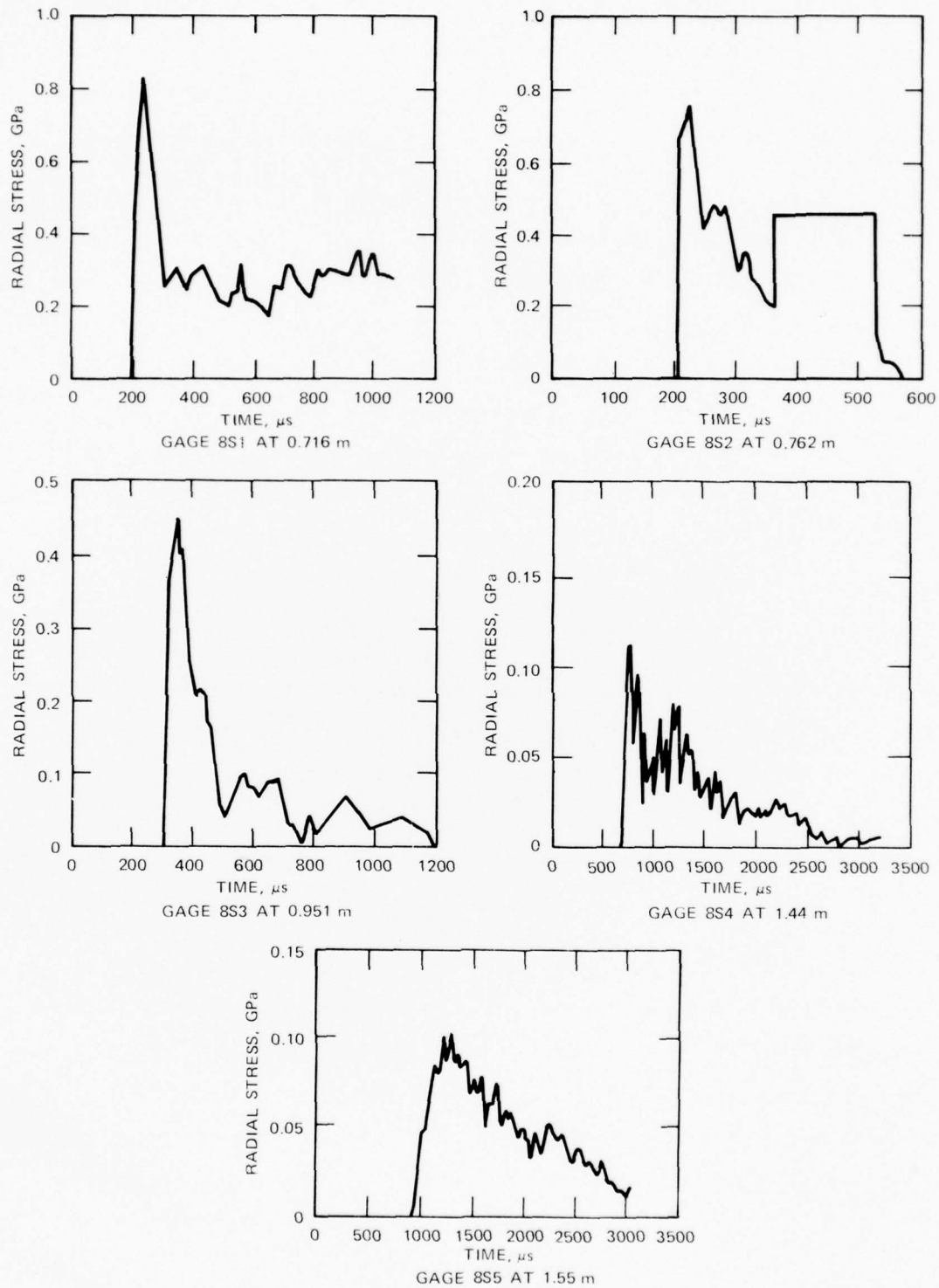
FIGURE 11   STRESS MEASUREMENTS, CENSE II, SHOT 8

MA-3698-32

40
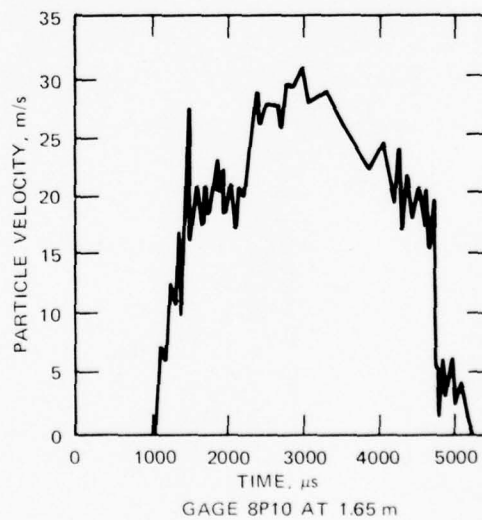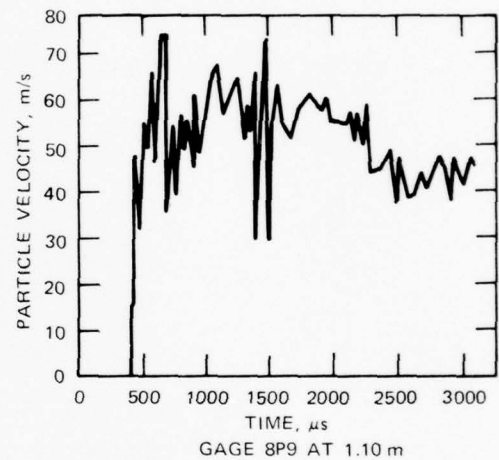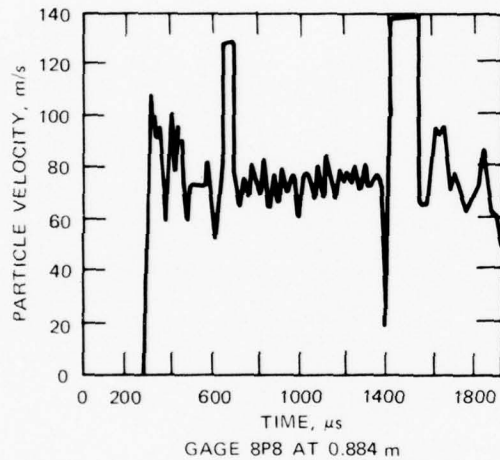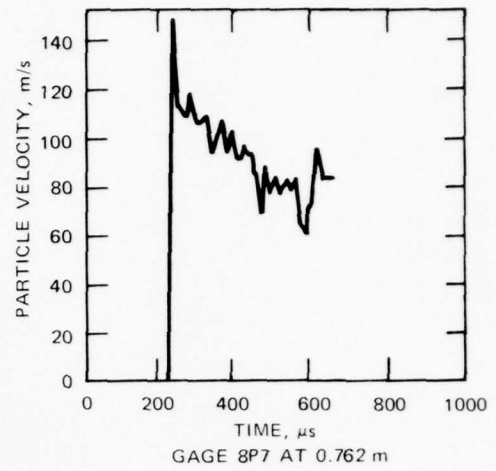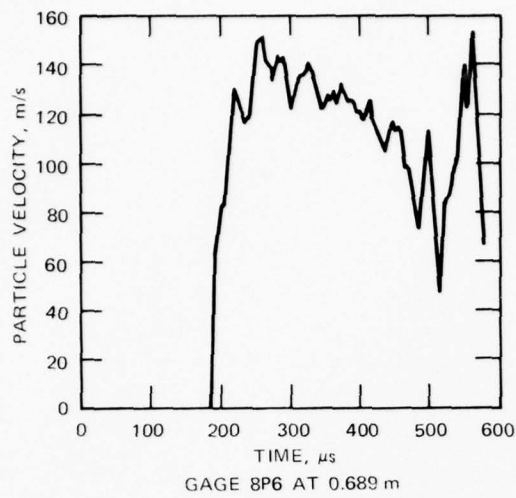
FIGURE 12   PARTICLE VELOCITY MEASUREMENTS, CENSE II, SHOT 8

MA-3698-33

41
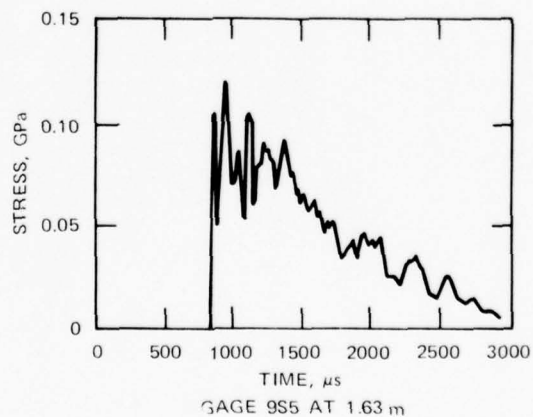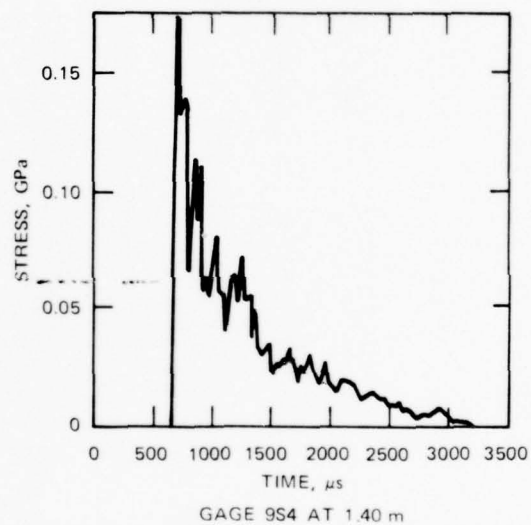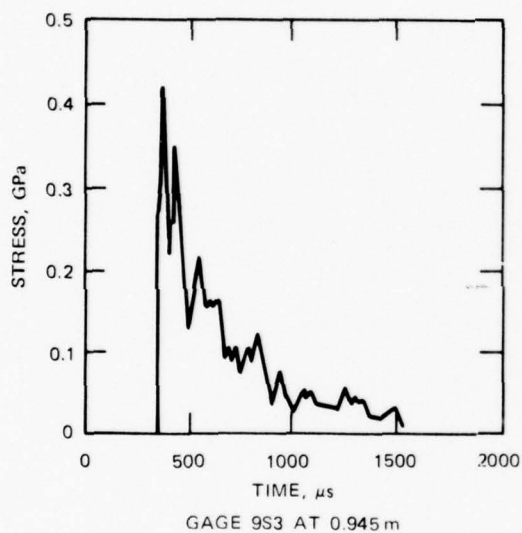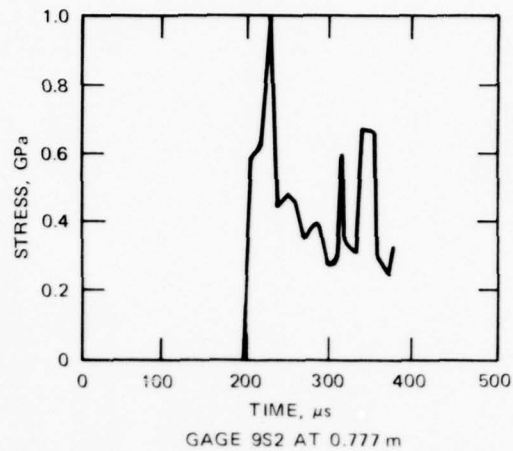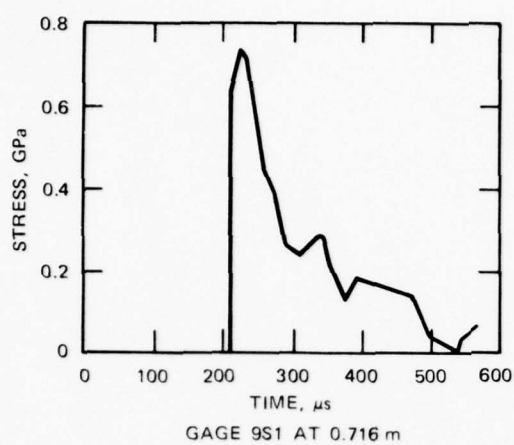
FIGURE 13   STRESS MEASUREMENTS, CENSE II, SHOT 9

MA-3698-34

42
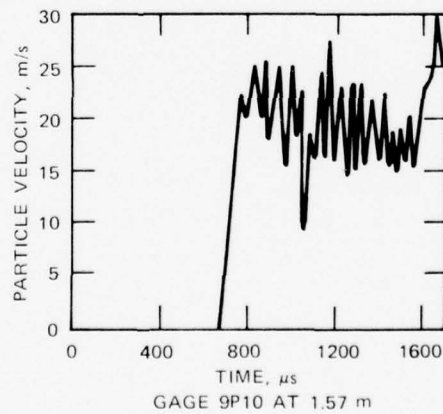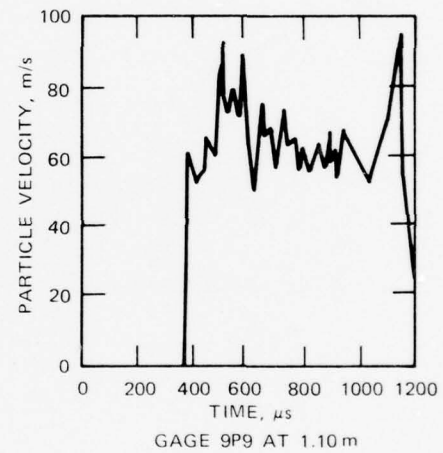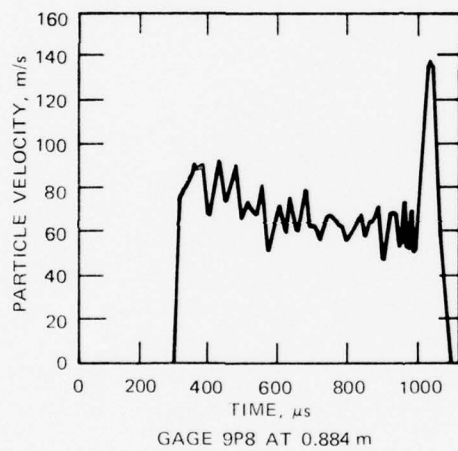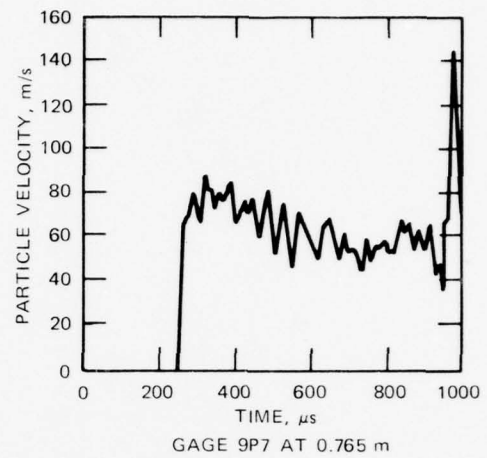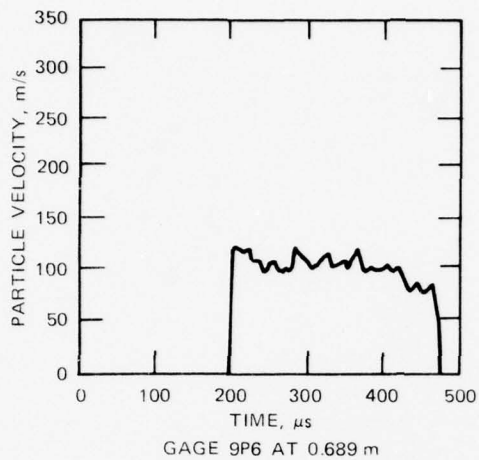
FIGURE 14   PARTICLE VELOCITY MEASUREMENTS, CENSE II, SHOT 9

MA-3698-35

43

Table 2

PEAK VALUES AND TIMES OF ARRIVAL, CENSE II, SHOTS 8 AND 9

Gage Number	Radial Distance (m)	Time of Arrival (μs)	Peak	Notes
Shot 8, ytterbium stress gages				
S1	0.716	192	0.84 GPa	
S2	0.762	205	0.76	
S3	0.951	213	0.46	
S4	1.44	680	0.116	
S5	1.55	900	0.103	
Shot 8, particle velocity gages				
P6	0.689	185	129 m/s	First peak
			151	Main peak
P7	0.762	235	148	
P8	0.884	277	108	
P9	1.10	400	48	First peak
			67	Main peak
P10	1.65	~1040	20	
Shot 9, ytterbium stress gages				
S1	0.716	207	0.74 GPa	
S2	0.777	200	0.6	First peak
			1.0	Spike
S3	0.945	336	0.43	
S4	1.40	684	0.175	
S5	1.63	850	0.124	
Shot 9, particle velocity gages				
P6	0.689	196	119 m/s	
P7	0.765	250	73	First shoulder
			91	Main peak
P8	0.884	303	77	First peak
			91	Main peak
P9	1.10	375	62.5	First peak
			94	Main peak
P10	1.57	681	22	First peak
			25	Main peak
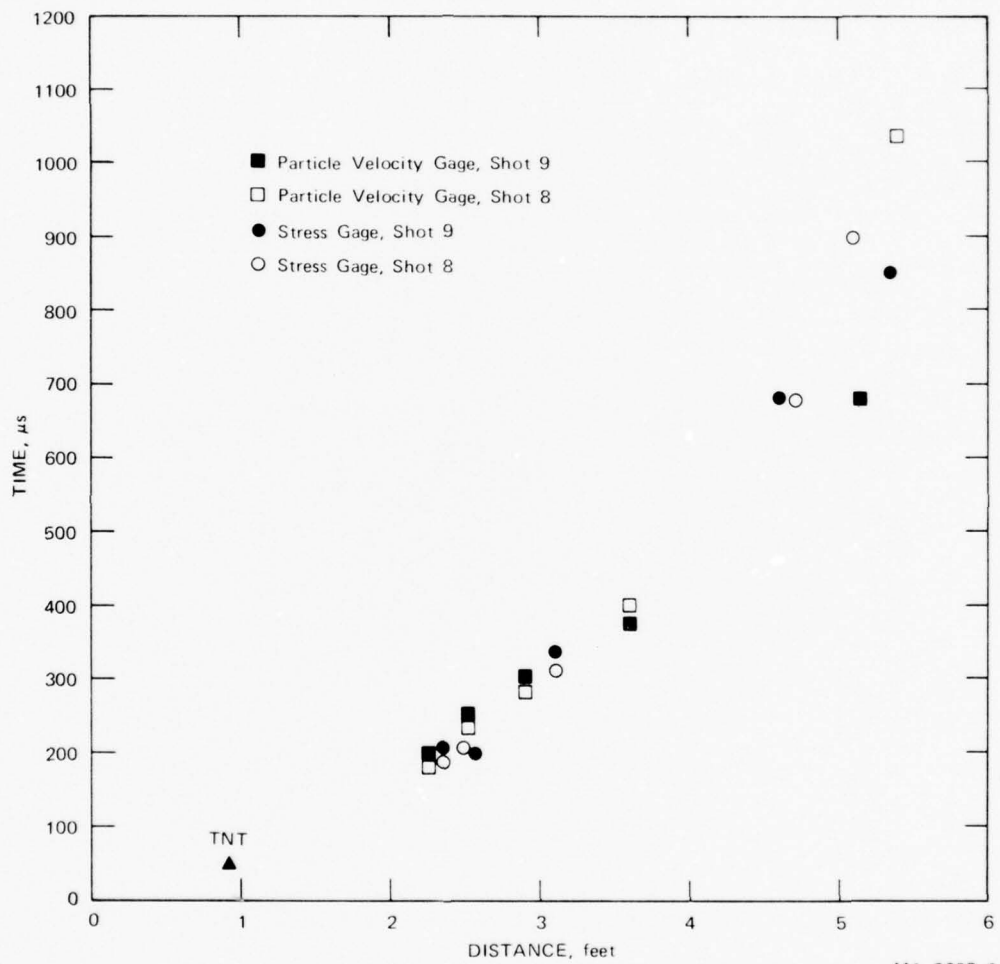
FIGURE 15   TIME OF ARRIVAL DATA FROM CENSE II, SHOTS 8 AND 9

MA-3698-6

45
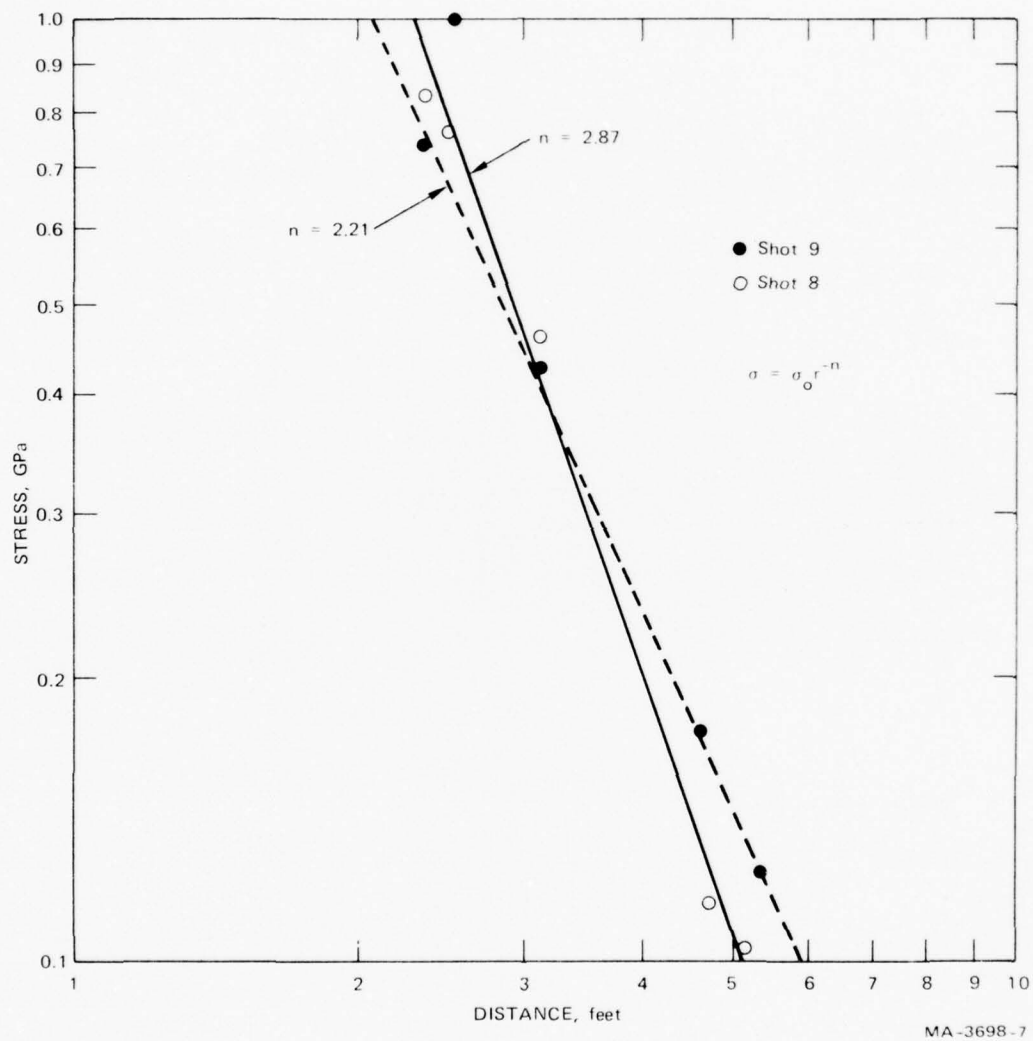
FIGURE 16   PEAK STRESS VERSUS DISTANCE FROM CENSE II, SHOTS 8 AND 9

46

lasted until near zero stress. The source of the oscillations in the
unloading portions are not fully understood. Particle velocity gages
also all produced records; however, approximately half of these contain
oscillations and noise that obscure the peak values. Although some of
the noise is electrical pickup, we feel that because the gages were
not centered in the holes, nonradial deformations occurred and may have
contributed to the unusual waveforms. This problem may be avoided in
the future by using installation holes only slightly larger than the
gages or by using some type of centering arrangement. (A universally
applicable installation procedure is unlikely because gage holes range
from short dry holes that may be visually inspected to deep holes filled
with drilling mud.)

Analysis

Since the differences between Shots 8 and 9 appear comparable
to the data scatter for the individual shots (see Figures 15
and 16), we analyzed the data in Figures 11 through 14 as though they had
been measured in a single experiment. Eight characteristic features in
addition to the wave foot were used to represent the stress profiles:
the peak, σ_{max}; 0.90 σ_{max}; 0.80 σ_{max}; 0.60 σ_{max}; 0.50 σ_{max}; 0.30 σ_{max};
0.20 σ_{max}; and 0.10 σ_{max}. These points were read from smoothed profiles
suggested by the experimenter based on (1) previous experience with the
gages and (2) the requirement that the profiles propagate and evolve
smoothly. The smoothed and original profiles are shown in Figures 17
and 18. Similarly the particle velocity profiles were characterized by
five features: the peak, u_{max}; 0.90 u_{max}; 0.80 u_{max}; 0.74 u_{max}; and
0.70 u_{max}. The original and smoothed particle velocity profiles are
shown in Figures 19 and 20. Note that two stress records and one particle
velocity record from Figures 11 through 14 were inconsistent with the
rest of the records, had large noise signals, or were otherwise judged
unreliable and are not included in Figures 17 through 20 and subsequent
analysis.

47
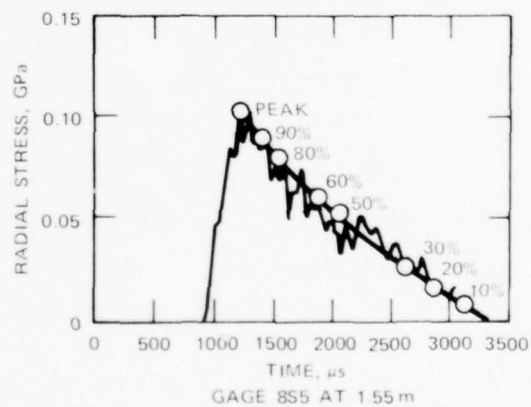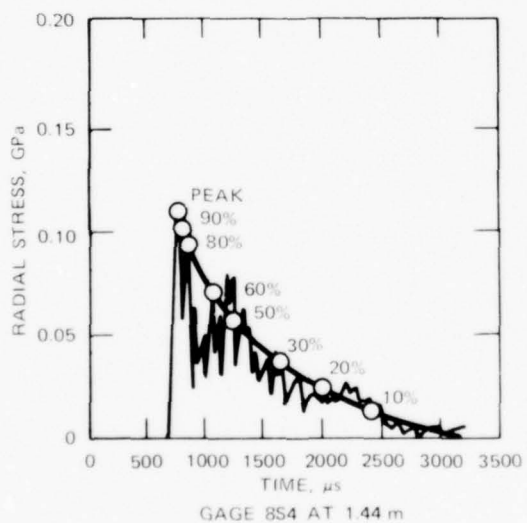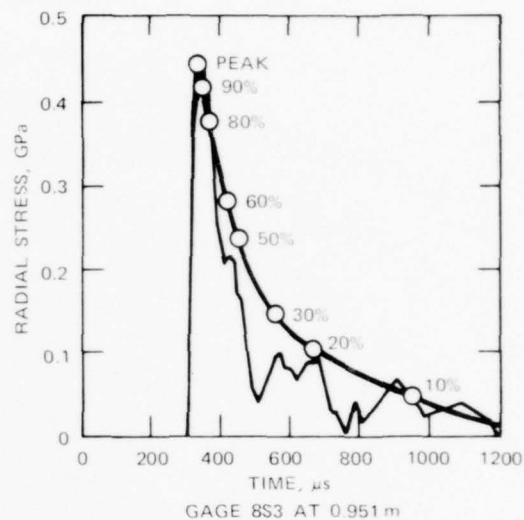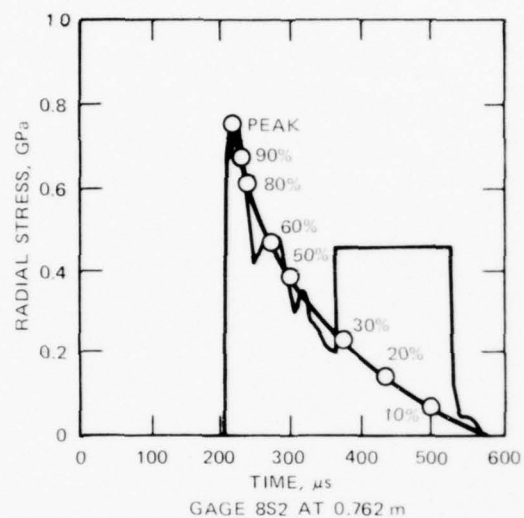
FIGURE 17   SMOOTHED STRESS PROFILES, CENSE II, SHOT 8 (SHOWING RAW DATA AND CHARACTERISTIC POINTS USED IN ANALYSIS)
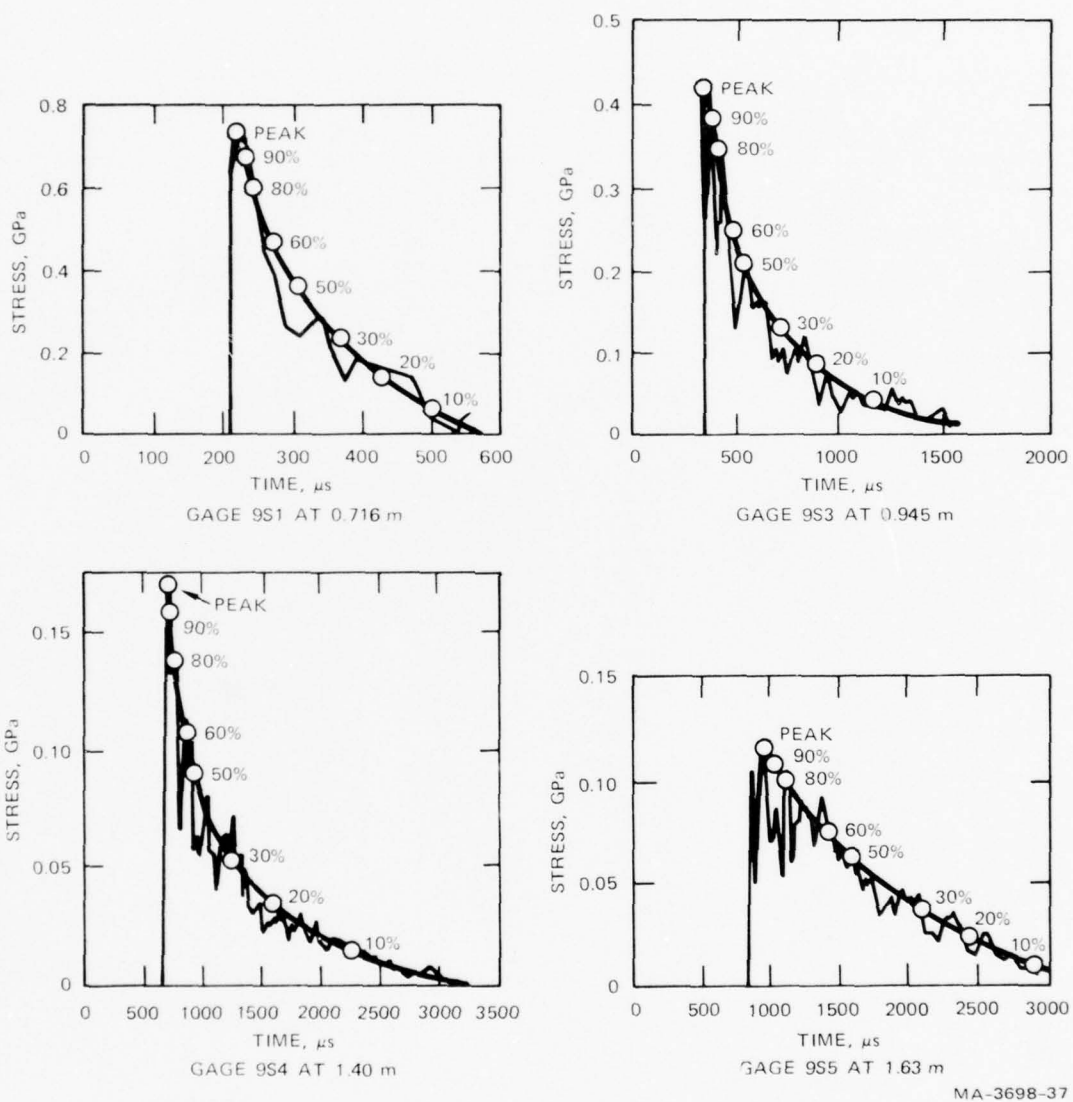
FIGURE 18   SMOOTHED STRESS PROFILES, CENSE II, SHOT 9 (SHOWING RAW DATA AND
CHARACTERISTIC POINTS USED IN ANALYSIS)

49
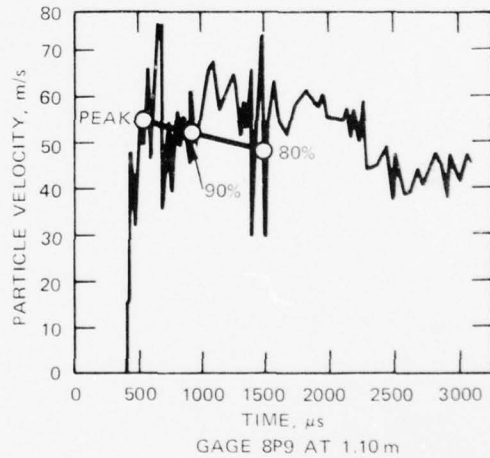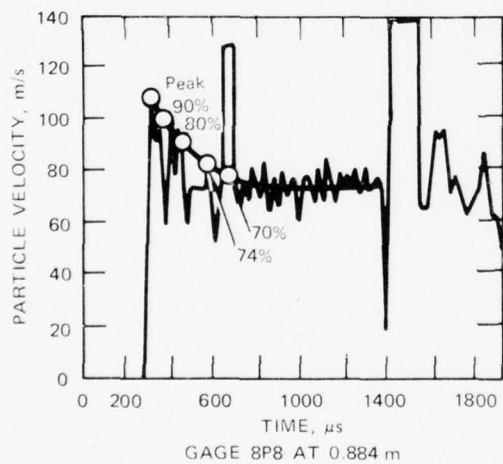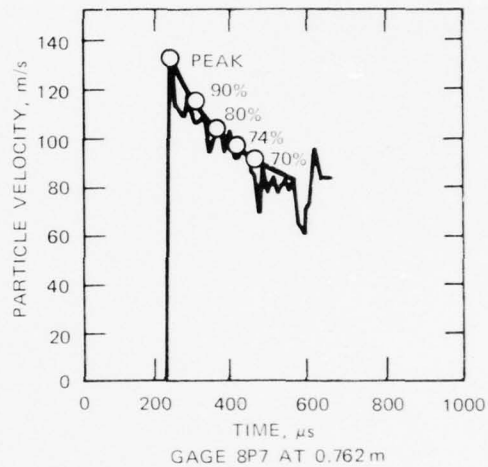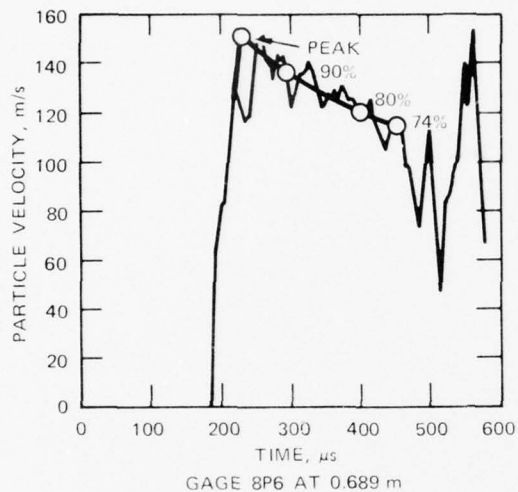
FIGURE 19   SMOOTHED PARTICLE VELOCITY PROFILES, CENSE II, SHOT 8 (SHOWING
RAW DATA AND CHARACTERISTIC POINTS USED IN ANALYSIS)

50
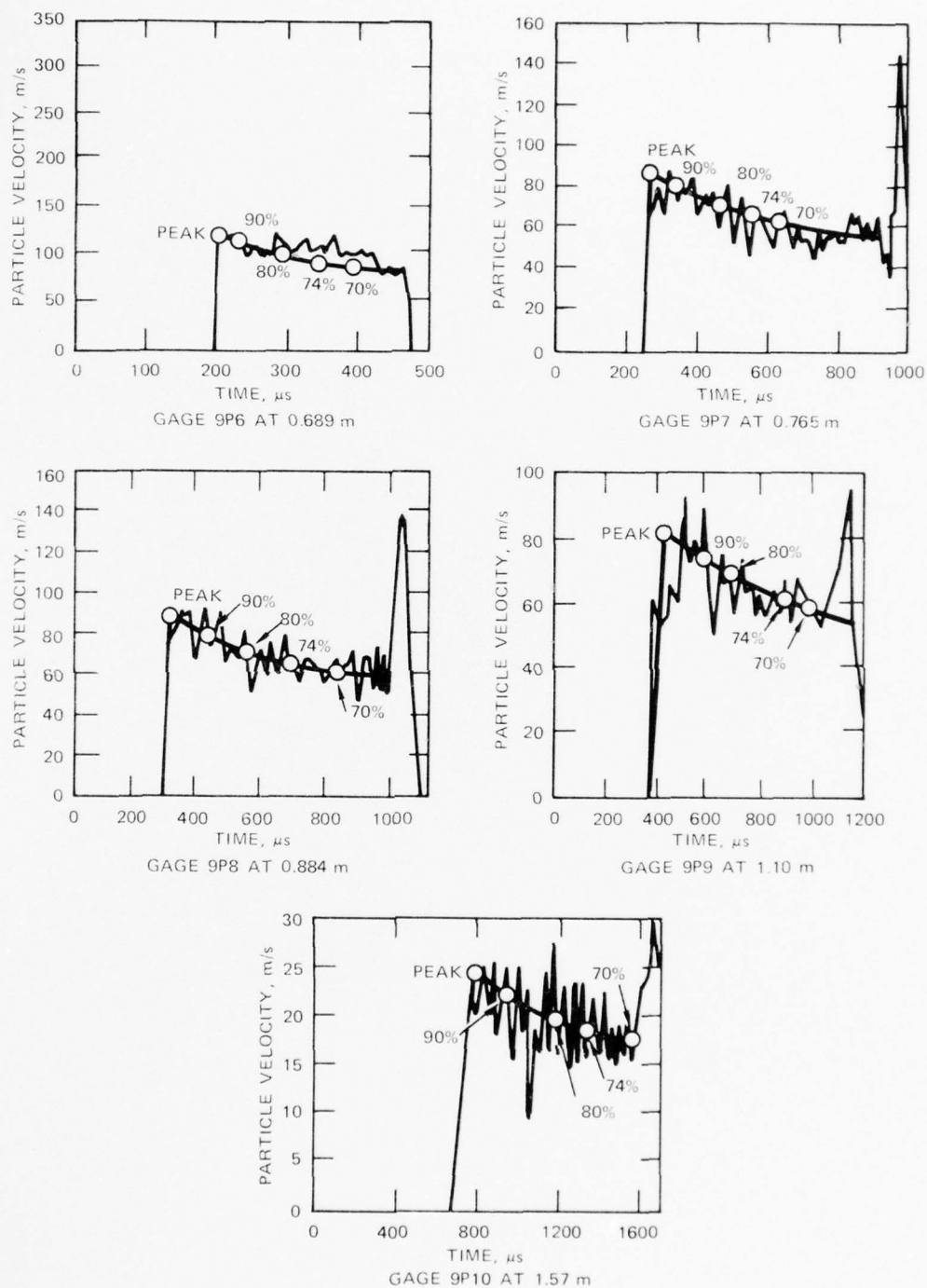
FIGURE 20   SMOOTHED PARTICLE VELOCITY PROFILES, CENSE II, SHOT 9 (SHOWING
RAW DATA AND CHARACTERISTIC POINTS USED IN ANALYSIS)

MA-3698-39

51

Stress and particle velocity gage flow surfaces were generated by
the LASS analysis using linear exponential expressions for the link
lines rather than quadratic exponential expressions because the data
scatter did not warrant the more complex form. From the gage flow
surfaces we obtained Lagrange stress and particle velocity histories.
Composite plots of five stress and five particle velocity histories
for particles at 0.70, 0.94, 1.17, 140, and 1.64 m are shown in Figures
21 and 22.

Using the gage flow surfaces, we then calculated the desired strain
and stress trajectories. These are shown in Figures 23 through 26.
Figure 23 gives the volume strain, ϵ_v, versus the strain difference,
$\epsilon_r - \epsilon_t$, for three particles at 0.94, 1.17, and 1.40 m from charge
center. Figures 24, 25, and 26 give the radial strain-tangential strain,
radial stress-radial strain and radial stress-volume strain trajectories
for the same particles. (The relationship of the calculated radial
stress-volume strain trajectories to material response is discussed
below.) The $\overset{\cdot}{\Phi}$ calculations are not reported because they show un-
realistically large oscillations and provide no material response informa-
tion. We believe that of the three trajectories in each plot, the one
for the particle at h = 1.17 m (near the center of the interval) is the
most accurate because the numerical approximations are best there, as
shown by the spherical PUFF test problem results discussed later in
this section.

Material response is most easily related to $\sigma_r - \epsilon_v$ trajectories,
Figure 26. The middle trajectory shows a volume strain of about 4 percent
at 0.25 GPa, which compares reasonably with available (static) data for
other soils such as the nearly water saturated ESSEX 1 soil units.[16,17]
The ESSEX static data are shown in Figure 27; an arbitrary average
response, with scatter range indicated, has been transferred from
Figure 27 to Figure 26 for comparison with the LASS results. The

52
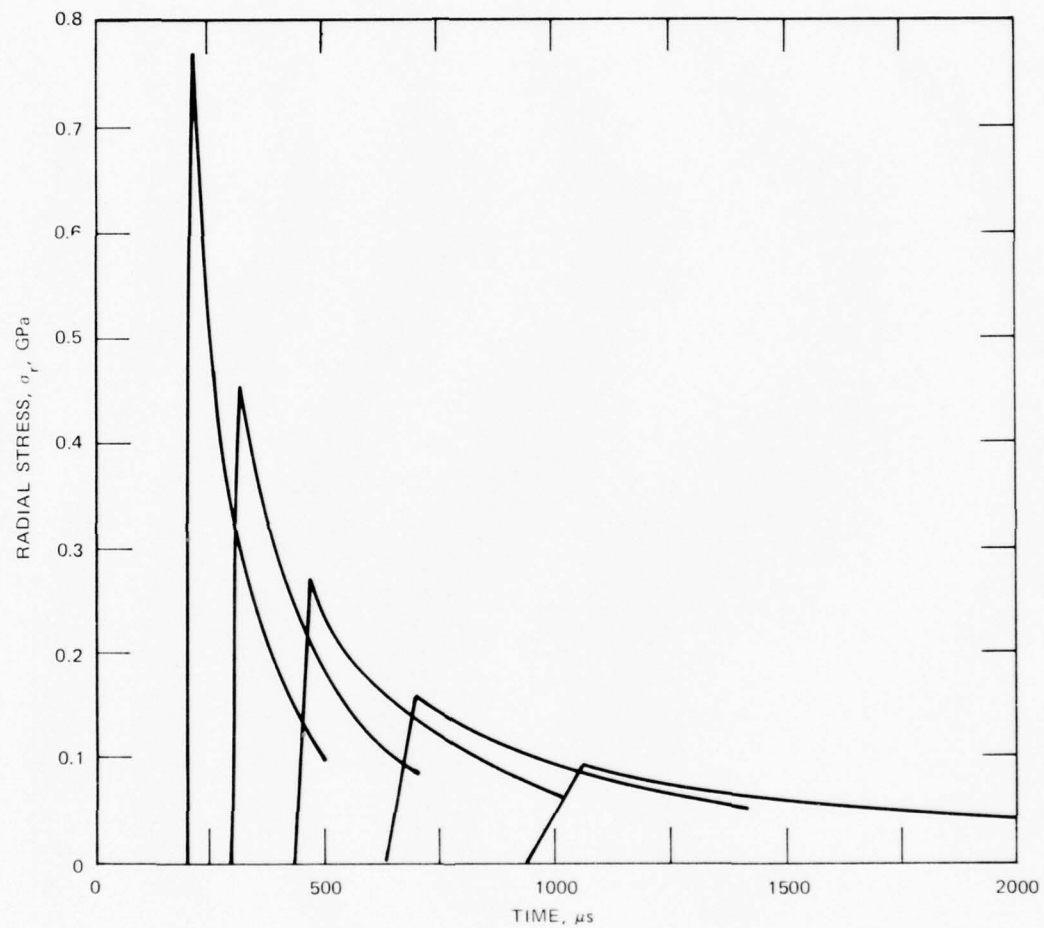
FIGURE 21   FIVE LAGRANGE STRESS-TIME PROFILES FROM GAGE FLOW SURFACE FOR
            CENSE II, SHOTS 8 AND 9
            Particles at h = 0.70, 0.94, 1.17, 1.40, and 1.64 m.
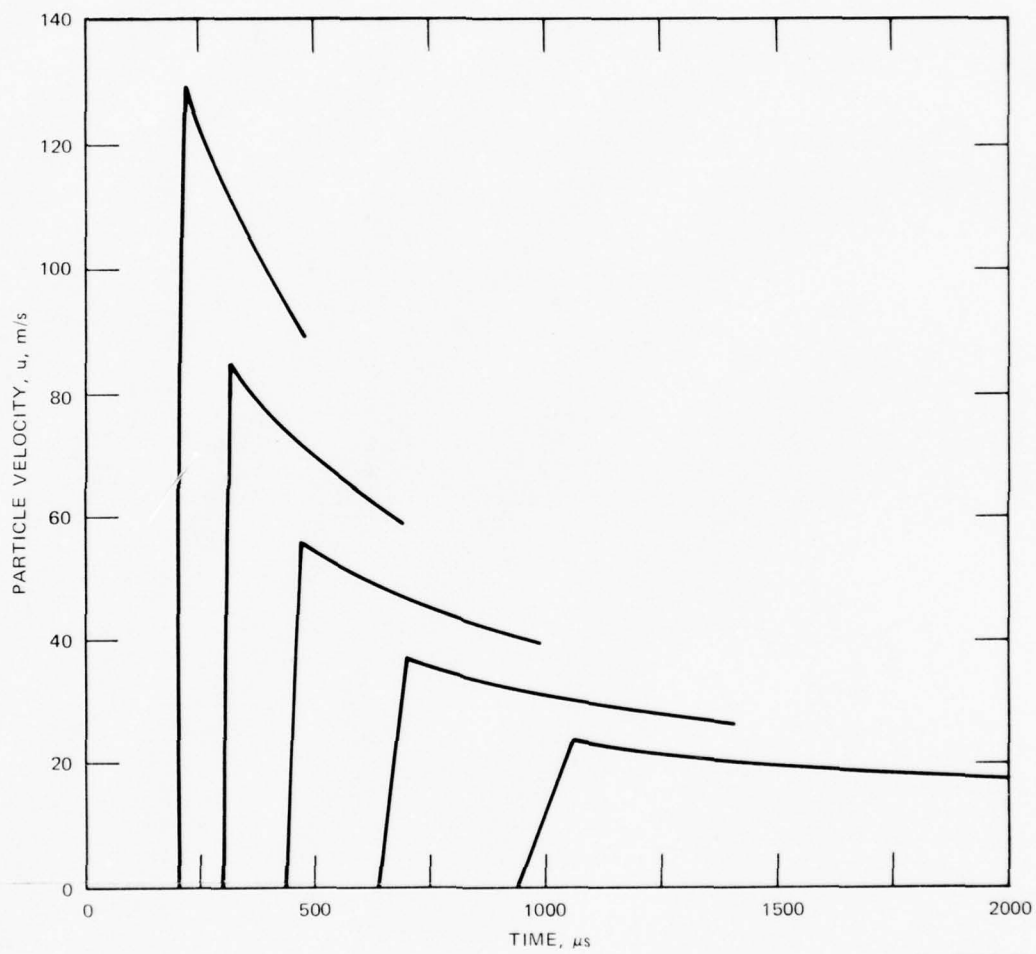
MA-3698-40

FIGURE 22   FIVE LAGRANGE PARTICLE VELOCITY-TIME PROFILES FROM GAGE FLOW
SURFACE FOR CENSE II, SHOTS 8 AND 9
Particles at h = 0.70, 0.94, 1.17, 1.40, and 1.64 m.
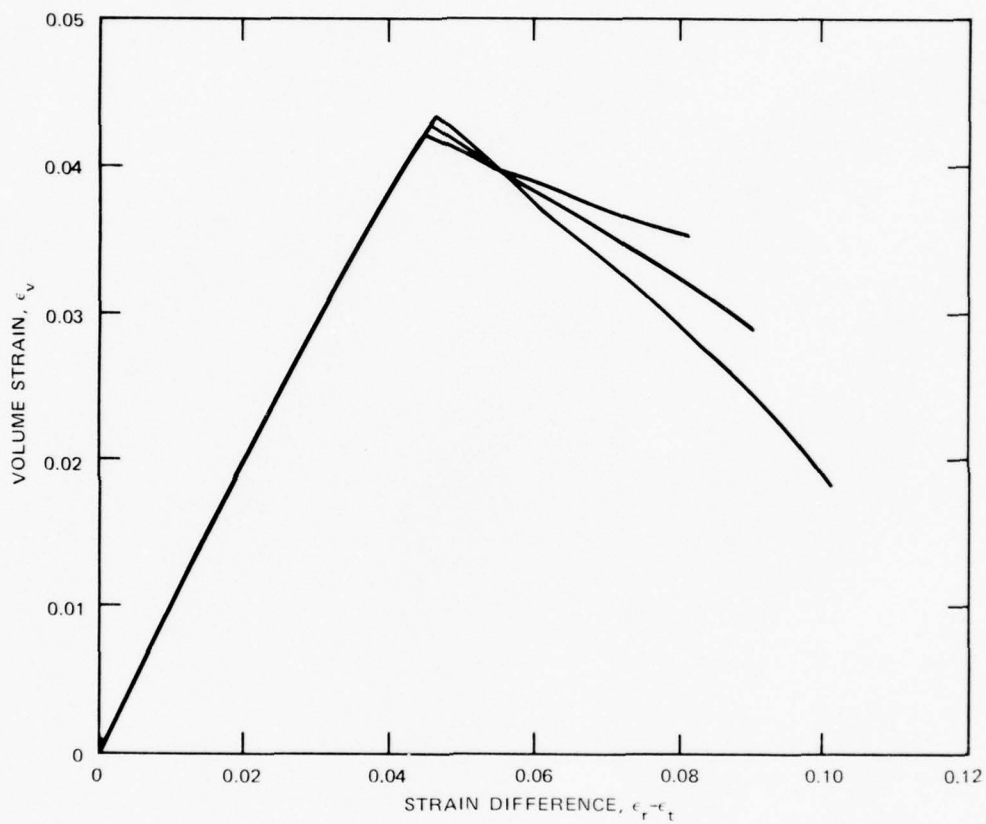
FIGURE 23   THREE VOLUME STRAIN-STRAIN DIFFERENCE TRAJECTORIES, CENSE II, SHOTS
8 AND 9, AT RANGES OF 0.94, 1.17, AND 1.40 m FROM CHARGE CENTER
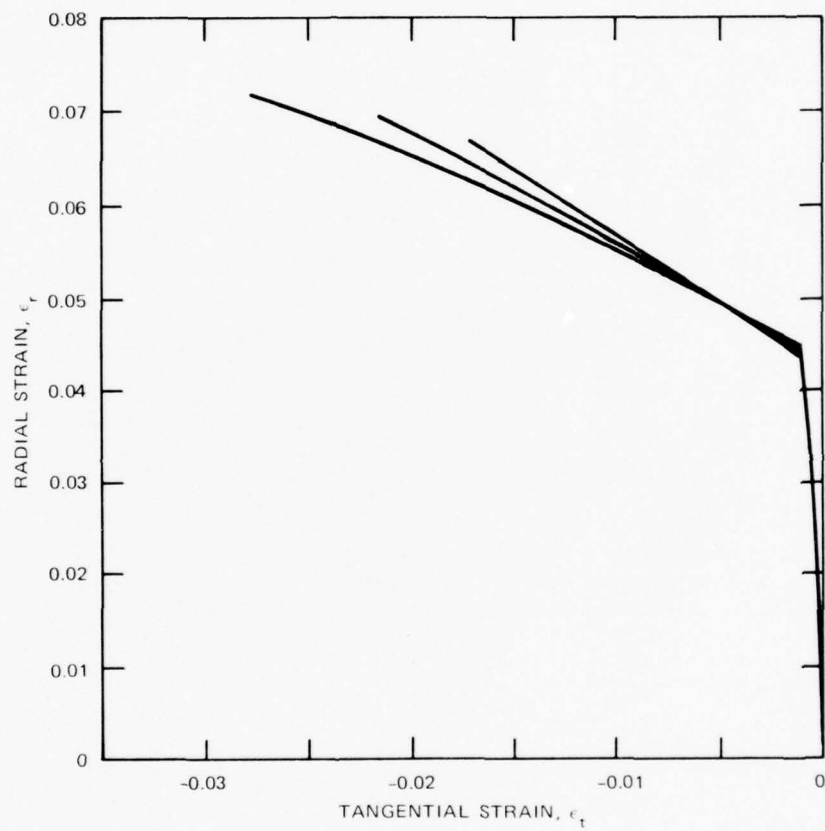
MA-3698-42

MA-3698-43

FIGURE 24   THREE RADIAL STRAIN-TANGENTIAL STRAIN TRAJECTORIES, CENSE II,
            SHOTS 8 AND 9, AT RANGES OF 0.94, 1.17, AND 1.40 m FROM CHARGE
            CENTER
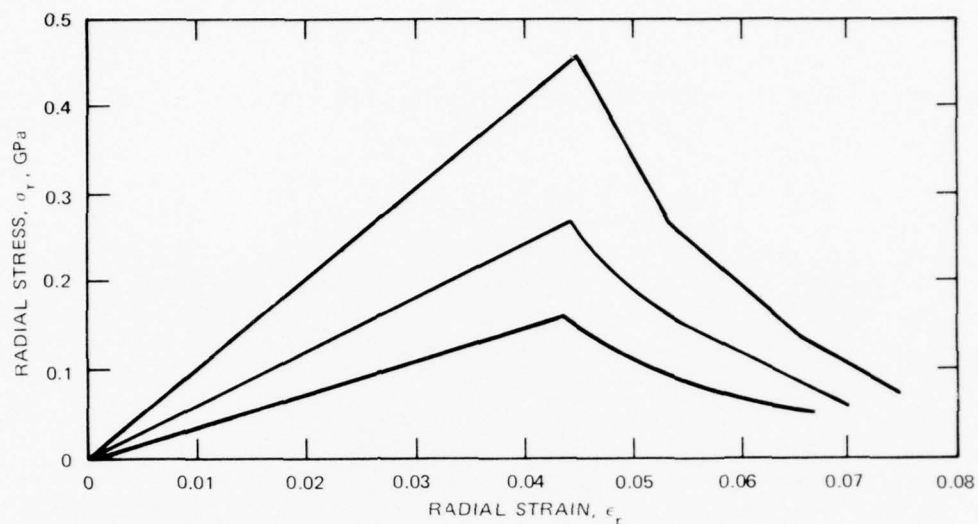
MA-3698-44

FIGURE 25   THREE RADIAL STRESS-RADIAL STRAIN TRAJECTORIES, CENSE II, SHOTS
            8 AND 9, AT RANGES OF 0.94, 1.17, AND 1.40 m FROM CHARGE CENTER
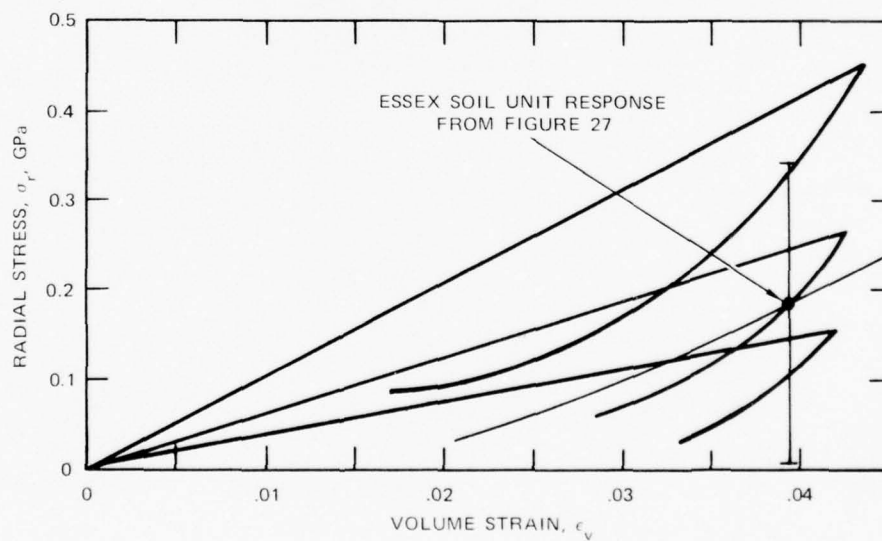
MA-3698-45

FIGURE 26   THREE RADIAL STRESS-VOLUME STRAIN TRAJECTORIES, CENSE II,
            SHOTS 8 AND 9, AT RANGES OF 0.94, 1.17, AND 1.40 m FROM CHARGE
            CENTER
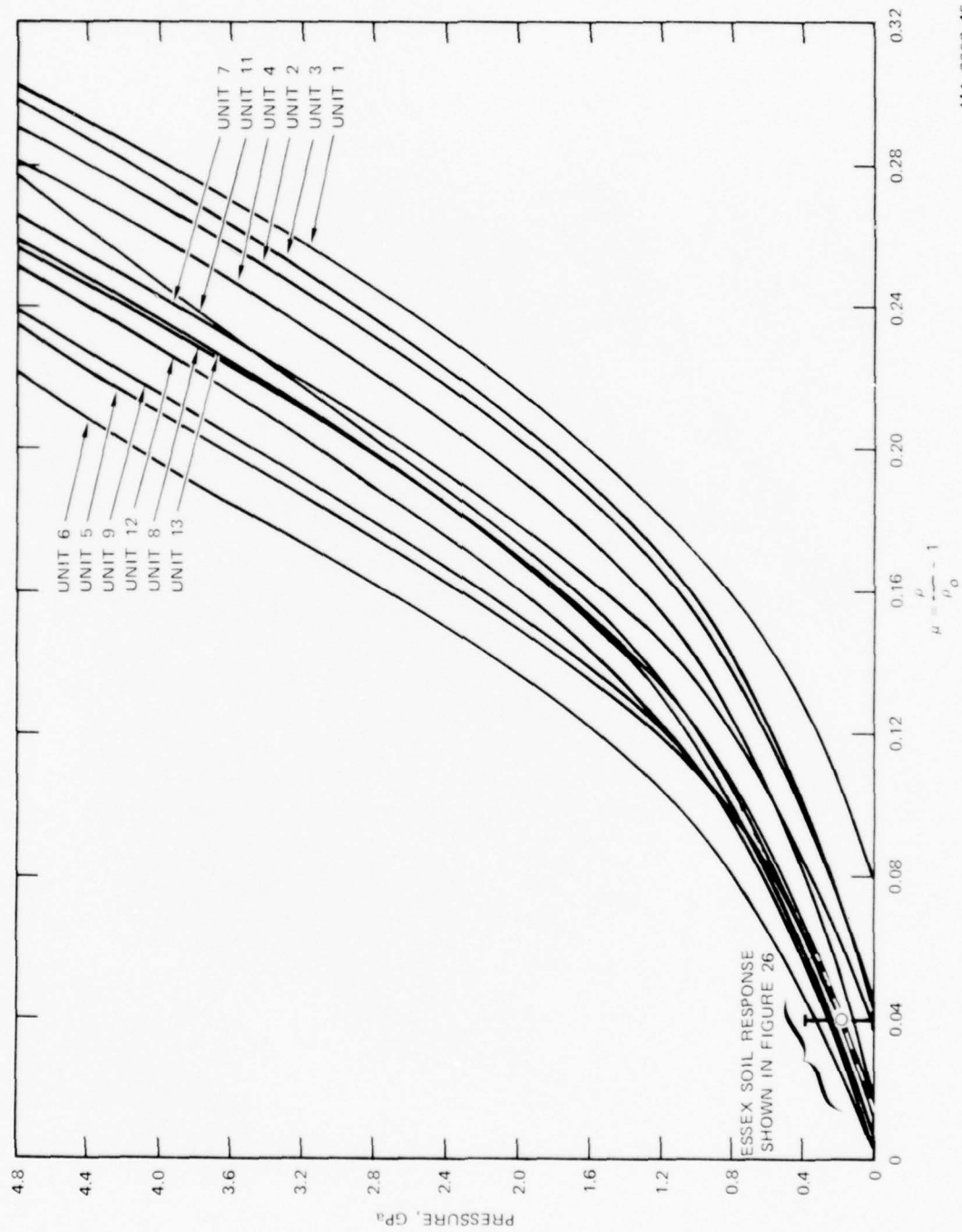
FIGURE 27   PRESSURE VERSUS μ FOR ESSEX I SOIL UNITS (FROM REFERENCE 17)

MA-3698-46

58

three calculated profiles in Figure 26 indicate a very steep compression
curve (obtained by connecting the peak state from each trajectory),
steeper than the release paths and steeper than the static data for
ESSEX material. Although the soil is surely in a locking regime at
these stresses, we believe the indicated compression curve is too steep.
The slope of the calculated release curves is much more reasonable and
compares well with the static data. In summary, we believe the middle
trajectory in Figure 26 is a reasonable calculation of the dynamic
properties of the CENSE II material and that the adjacent trajectories
give good release data but should not be used to establish the local
slope of the equlibrium compression curve.

It is worth pointing out that, for soils, the stress difference σ
is typically very small, about 0.01 GPa or less.[16] Since this is one
to two orders of magnitude less than the stress range of our measurements,
σ_r is nearly equal to the mean stress. Therefore the $\sigma_r - \epsilon_v$ trajectories
in Figure 26 should be close to mean stress- ϵ_v and hence can be used to
estimate the bulk modulus for CENSE II material.

MIPV FIELD GAGE PERFORMANCE

MIPV gages do not in general produce as high quality field records
as ytterbium stress gages. Therefore during the present program we
conducted both experimental and analytic studies to assess and improve
the performance of the MIPV gage.

Experiments

Possible sources of high frequency, high amplitude noise in MIPV
gage field records include electrical pickup (primarily in the long
cable runs typifying field events), mechanical buckling of the gage
during deformation, and real flow oscillations induced by the geologic
inhomogeneities of actual sites. To investigate the origin of the noise,

59

we fielded MIPV gages in several experiments performed at Systems, Science and Software (S^3) remote test site. The test site environment provided a more controlled measurement situation than typical field conditions, simplifying data interpretation.

The experiments and results are discussed in Appendix D. The records were quieter than field data, but they contained several large amplitude variations not usually seen in field data. The variations are attributed to the response of the concrete matrix being tested by S^3 and are not considered to be artifacts of the MIPV gage or to provide useful information for improving MIPV gage performance. The noise reduction, however, is considered to be significant and is attributed to the relatively short cable runs compared with field conditions. These results lead us to suggest that, in future field applications, the current carrying cables should be shortened by locating the MIPV gage power supplies in a hardened structure near the shot and operating them remotely. The results of the tests at S^3 indicate that under the proper conditions, in particular, short cable runs, the present MIPV gages can provide high quality field data.

Analysis

When MIPV gages are used at soil sites, such as in the CENSE II events, they are usually fielded near the bottom of grout columns aligned radial to the source. The basic configuration with typical gage hole dimensions is shown in Figure 28. This emplacement method is used because no practical techniques have yet been developed to embed the gages directly in native material. Nevertheless, an important question is whether an MIPV gage measurement made in a radial grout column differs significantly from the measurement the same gage would make in native material.

GROUND SURFACE

RADIAL GROUT
COLUMN (IN
SLANT DRILL HOLE)

MIPV GAGE

0.91 mm

51 mm

76 mm

51 mm

SOURCE
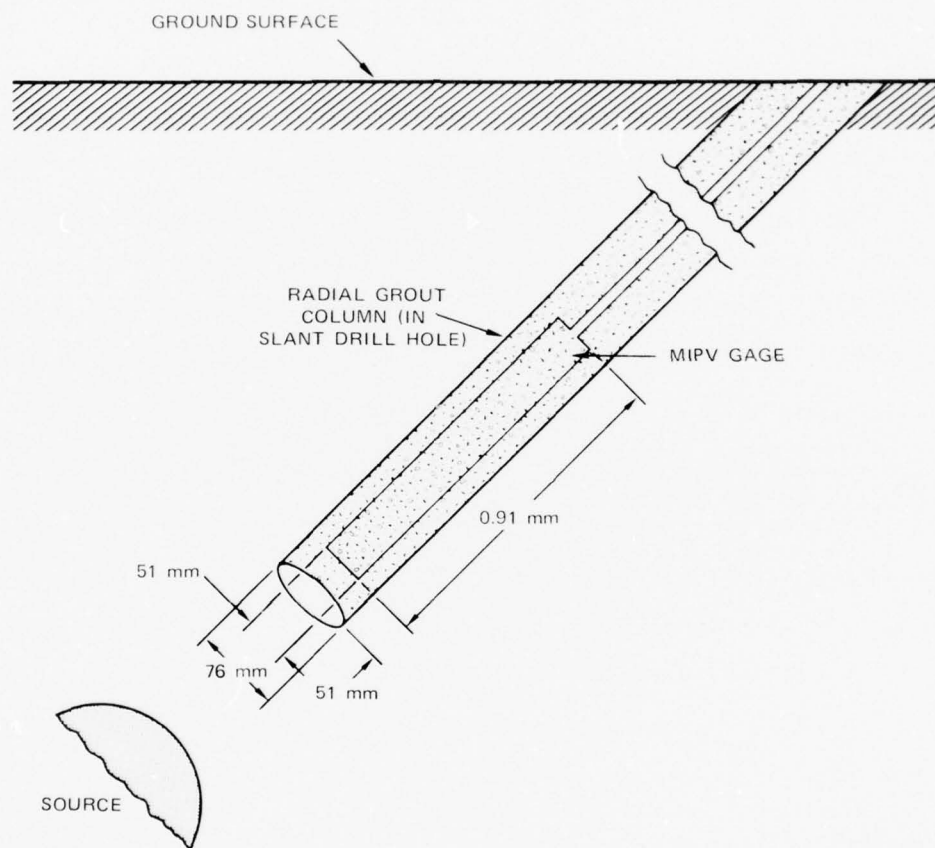
MA-3698-11A

FIGURE 28   SCHEMATIC REPRESENTATION OF MIPV GAGE FIELDED IN RADIAL
GROUT COLUMN

To examine this question, we performed a two-part analytical study. We first determined deformations in the grout column and the free field, using TOODY III, a two-dimensional wave propagation code. We then calculated the gage response to the local grout deformations by numerically solving the electromagnetic equations governing gage output. Results of these two calculations are discussed below. Note that the present studies pertain to fielding effects only and exclude experimental errors.

Calculations of the grout and free-field soil motions were based on the emplacement representation shown in Figure 29. We assumed the incident wave to be planar, and we used linear inelastic constitutive relations for the soil and grout. Baseline parameters for the constitutive models were taken from the WES static data for E-2D 28-day grout[18] and for Fort Polk, Unit 5 soil.[17] The interface between the soil and grout is a slide line of adjustable shear strength.

The investigation consisted of a four-case parameter study in which we varied the relative densities and moduli of the soil and grout as well as the strength of the interface. The magnitude of the density variation represented the largest experimentally observed differences; the larger moduli and interface variations were selected arbitrarily to determine the relative sensitivity to these parameters. The parameter variations and results are summarized in Table 3.

The key findings were as follows: (1) for the baseline case the peak axial particle velocity in the grout underregistered by less than 3 percent, (2) an 11 percent density variation produced a smaller axial velocity change than a 50 percent modulus variation, and (3) the interface strength is important, but even a change to zero strength caused only about a 10 percent axial velocity underregistration.

CODE BOUNDARY

GROUT
E-2D, 28 DAY

SLIDE LINE
(STRENGTH
ADJUSTABLE)

SOIL
FORT POLK, UNIT 5

CYLINDRICAL
SYMMETRY
AXIS

P(t)
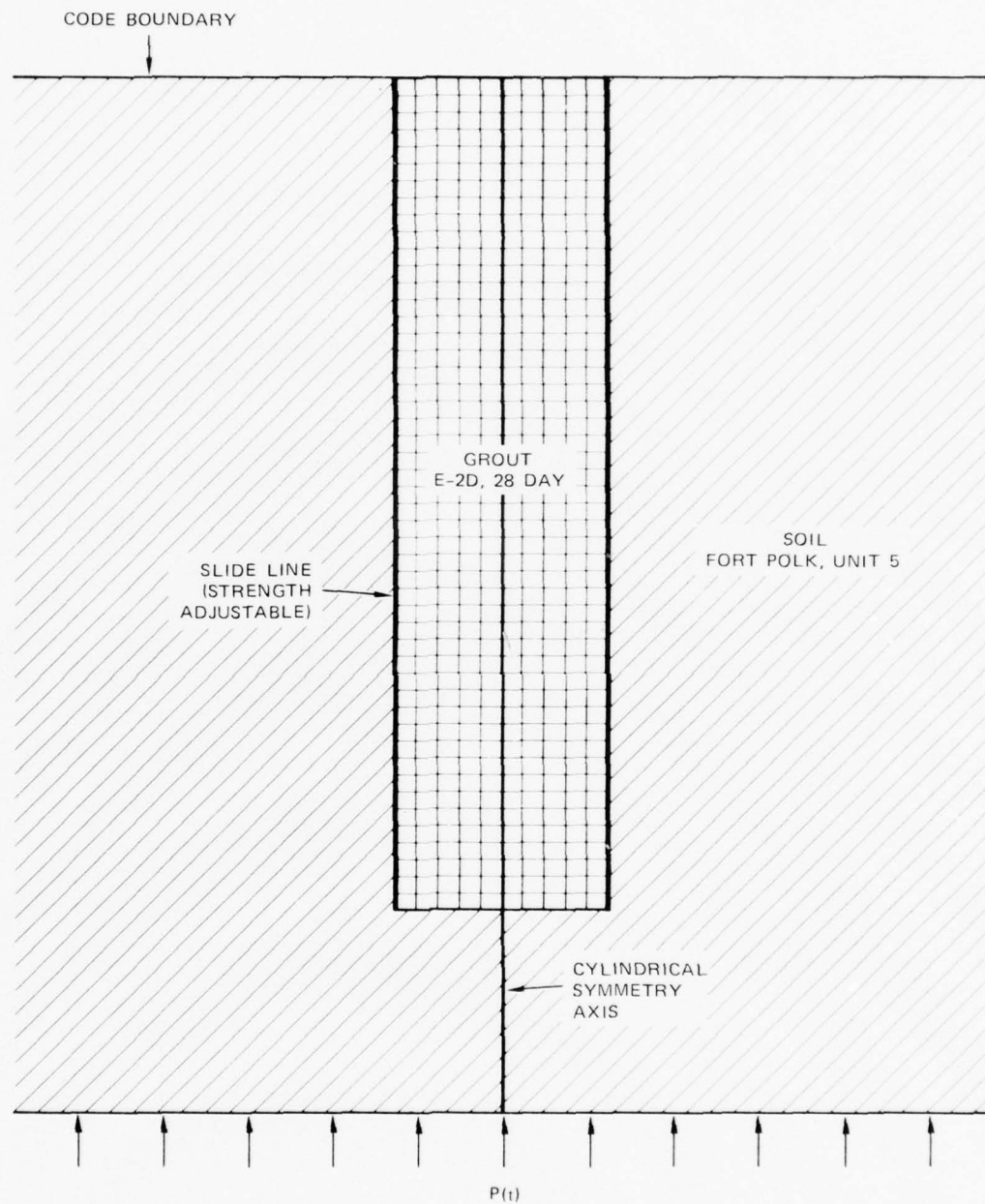
MA-3698-12

FIGURE 29   LAYOUT USED FOR TWO-DIMENSIONAL CALCULATIONS OF GROUT AND
SOIL MOTIONS

63

Table 3

FOUR-CASE PARAMETER STUDY OF GROUT AND SOIL MOTION

	Case 1 Baseline	Case 2 Density Varied	Case 3 Modulus Varied	Case 4 Interface Varied
Parameters varied				
Density ratio (grout/soil)	1.02	1.13	Baseline	Baseline
Modulus ratio (grout/soil)	1.34	Baseline	2.01	Baseline
Interface strength	∞	Baseline	Baseline	0
Results				
Peak particle velocity ratio (grout/soil)	0.97	0.90	0.94	0.88

To show the general relationship between axial and radial motions in the grout column, we present additional results for the baseline calculation, Case 1. Figure 30 shows results for two conditions at the stress boundary: step compression only and step compression followed by step release. The figure shows axial velocity 51 mm into the grout column on the centerline (typical gage location), radial velocity 51 mm into the grout at the grout-soil interface, and free field motion, which is entirely axial, at the corresponding location. The radial velocity arising from the grout-soil impedance mismatch reaches no more than 8 percent of the peak axial velocity and later decreases to essentially zero. Note also that the peak axial velocity approaches the free field values as reported in Table 3, but that during equilibration (early times) there are larger differences.

The second part of the analytical study of MIPV gages in grout columns was to calculate the gage response to the predicted grout column deformations. The electrical output, $\mathcal{E}$, of a two-loop gage with a constant current I flowing in the primary is given by Eq. (3), Section 2.

$$\mathcal{E} = - I \frac{dM}{dt} \tag{3}$$

where M is the mutual inductance between the loops. We have shown previously[4] that the mutual inductance between a primary loop, p, and a secondary loop, s, may be calculated from the relation

$$M_{ps} = \frac{\mu_o}{4\pi} \iint \frac{d\vec{\ell}_p \cdot d\vec{\ell}_s}{r_{ps}} \tag{4}$$

where $d\vec{\ell}_p$ and $d\vec{\ell}_s$ are elemental line vectors of the primary and secondary loops, and r_{ps} is the separation of the elements. By
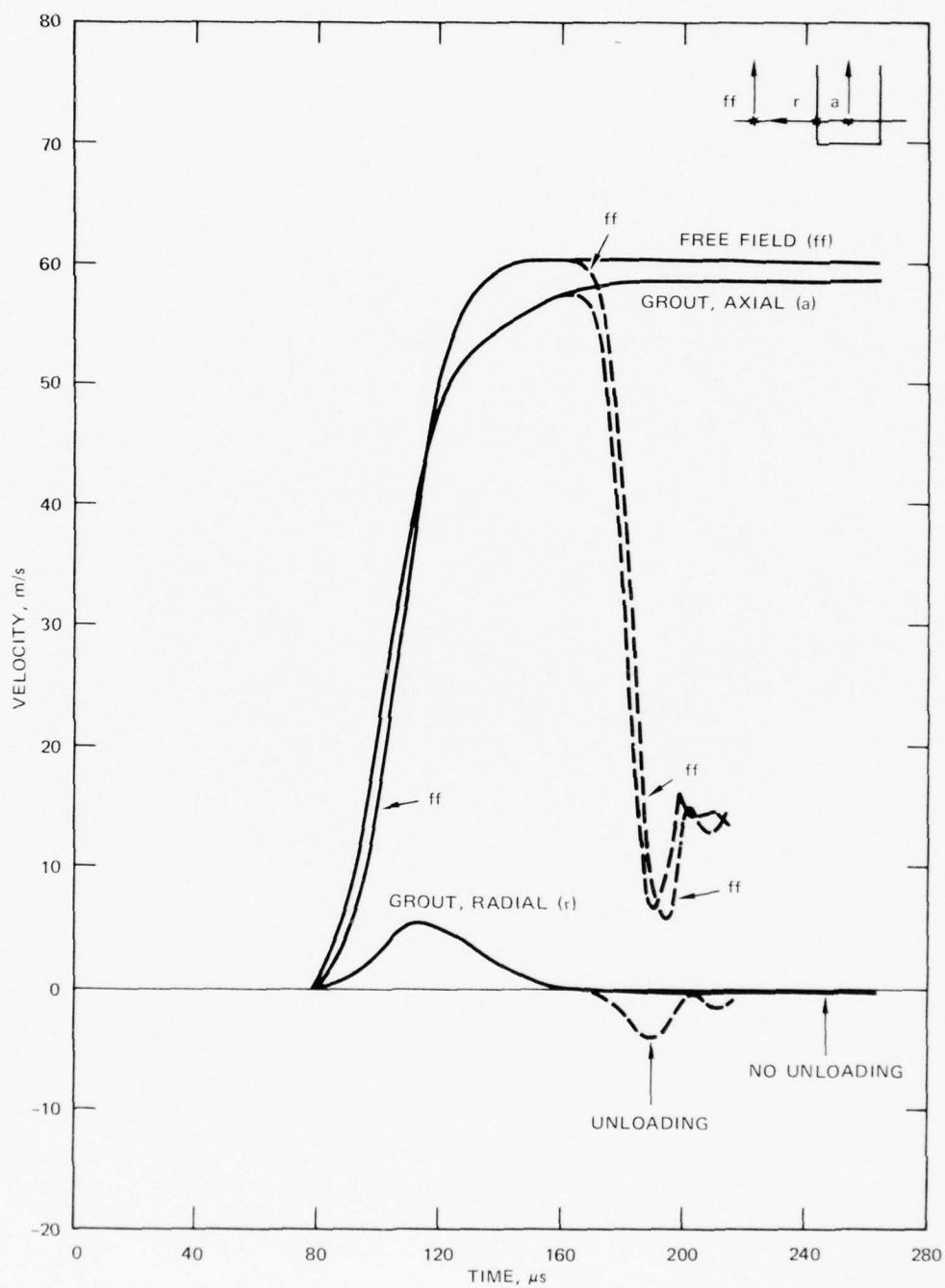
FIGURE 30   GROUT AND FREE FIELD SOIL MOTIONS, BASELINE CASE
Calculations without unloading (solid) and with unloading (dashed)
are shown.

66

dividing each loop of an MIPV gage into finite elements and assigning instantaneous positions to these elements from the previous TOODY III calculations, we can evaluate M_{ps} from Eq. (10) at various times during the deformation. Consequently we can solve Eq. (3) for the MIPV gage output as a function of time. A code was written to perform these steps for multiple loop MIPV gages.

Results for an ideally emplaced (free-field) MIPV gage and for an MIPV gage in grout (baseline grout deformation case) are shown in Figure 31. The signal for the gage in grout has been separated into one co component resulting from axial motion and one resulting from radial motion. Note that radial motion here is not just that at the front of the gage (see Figure 30), but is the motion of all elements from the gage front to the current position of the loading wave. The component of the gage signal resulting from nonaxial motions never exceeds about 7 percent of the total signal and is usually much less. Except during an equilibration period near the peak of the compression, the field gage signal is within a few percent of the ideal signal everywhere.

Our conclusion from this study is that the differences in signal between an ideally emplaced gage and a gage near the bottom of a grout column well matched to the site are not significant compared with typical noise levels in field records. The effects on the LASS analysis of the deviations from ideal response during equilibration are not known but are expected to be small since a similar error is introduced at each gage station.

ANALYSIS DEVELOPMENT

The objective of this phase of the program was to assess and improve the accuracy of the LASS analysis described in Section II. This form of Lagrange analysis represents individual records as piecewise linear

67
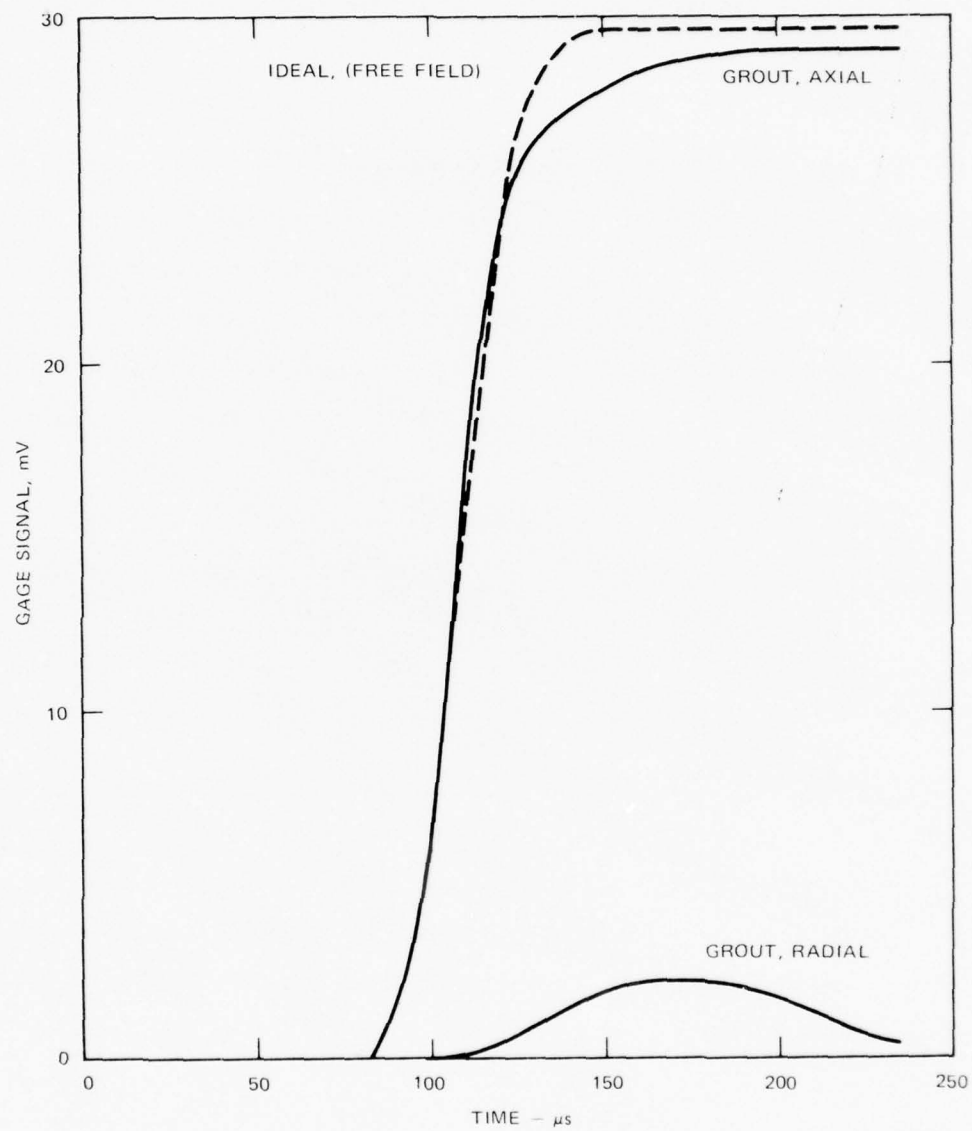
FIGURE 31   CALCULATIONS OF MIPV GAGE SIGNALS, BASELINE CASE, FOR FREE FIELD AND GROUT EMBEDDED GAGES

The output for the grout embedded gage has been decomposed into axial and radial components. The calculation is for a hypothetical two-loop gage.

68

profiles and spatially connects the profiles by smooth global link lines.
The piecewise linear analysis was created to handle field data, which
typically have a lower confidence level for individual profile measure-
ments than laboratory data.

We were primarily interested in two questions: (1) How sensitive
are LASS results to specific internal numerical data handling procedures?
(2) What is the actual error in the calculated trajectories? To examine
these questions, we created a test problem for which the profiles and
corresponding stress and strain trajectories were known and used it to
evaluate LASS. We also reanalyzed Swift's small scale spherical block
shot experiments in Mixed Company sandstone.[19] The following two sub-
sections give the LASS findings on the test problem and the results of
the Mixed Company sandstone analysis.

SPHERICAL PUFF TEST PROBLEM RESULTS

It is difficult to test or improve the Lagrange analysis by using
actual gage records because these records have experimental errors and
because the material constitutive relations corresponding to them are
unknown. Therefore we developed a test problem by assuming a specific
constitutive model and using the one-dimensional wave propagation code,
spherical PUFF, to calculate stress and particle velocity profiles
corresponding to the constitutive relations and a prescribed boundary
condition. This is an extension of earlier work in this program by
Grady et al.[5] Note that the assumed constitutive relations need not
model a specific real material although they should be reasonably
representative of geophysical materials; the objective is simply to
obtain a set of profiles (ideal gage records) and the corresponding
constitutive relations.

The assumed constitutive relations were of the variable modulus
form with parameters fitted to approximately describe Mixed Company

69

sandstone response in small scale spherical block shots.[19]   For spherical

flow, the variable modulus model consists of two relations

$$K \; = \; \frac{dP}{d\mu} \tag{11}$$

and

$$G \; = \; \frac{d\bar{\Phi}}{d\epsilon} \tag{12}$$

where K and G are the bulk and shear moduli, P and $\bar{\Phi}$ are the

mean stress and stress difference, and μ and ϵ are the volume strain

and strain difference ($\epsilon_r - \epsilon_t$). The model is completed by specifying

K, G, and ρ_o (the initial density).

For the test problem we assumed:

$$K \text{ (GPa)} = \begin{cases} K_Y = 12.2 & , \; \mu_{max} < 0.011 \text{ (elastic loading or} \\ & \qquad\qquad\qquad\quad \text{unloading)} \\[2ex] K_L = 1.5 + 1.0 \times 10^2 \mu & , \; \dot{\mu} > 0 \text{ and } \mu = \mu_{max} \text{ (plastic loading)} \\[2ex] K_U = 15 + 6.0 \times 10^2 \mu & , \; \text{(unloading or cycling beyond elastic} \\ & \qquad\qquad\qquad\quad \text{limit)} \end{cases}$$

$$G \text{ (GPa)} = \begin{cases} G_Y = 0.5 + 18.5 \, \mu - 6.5 \, \epsilon & , \; \dot{\epsilon} > 0 \quad \text{(loading)} \\[2ex] G_U = 7.5 & , \; \dot{\epsilon} < 0 \quad \text{(unloading)} \end{cases}$$

$$\rho_o \, (\text{kg/m}^3) = 2.07 \times 10^3$$

where the subscripts Y, L, and U denote preyield, load, and unload

moduli, and μ_{max} is the maximum volume strain attained at any time

during the loading cycle. The comparison of μ with μ_{max} to determine

conditions for changing from unloading to the loading modulus during

small cycles or oscillations in the flow conforms to established practice[20]

and avoids the unrealistic prediction of large volume decrements from small stress oscillations. In the present case, for computational convenience, we accomplished the same purpose by using minimization criteria on P and Φ rather than by saving μ_{max} for comparison with μ:

$$P = MIN \left[P_o + K_U d\mu, \int_o^\mu K_L d\mu \right] , \quad \mu > 0.011$$

$$\Phi = MIN \left[\Phi_o + G_U d\epsilon, \int_o^\epsilon G_L d\epsilon \right]$$

where MIN $[X,Y]$ means the lesser of X and Y, and P_o and Φ_o are the values of P and Φ before the last time increment.

The above model, in conjunction with an exponentially decaying particle velocity history boundary condition, produces records displaying precursor formation, peak attenuation, and dispersion. Seven particle velocity and seven stress histories calculated from the model are shown in Figures 32 and 33.

The success of the test problem approach depends on the accuracy with which spherical PUFF generates the stress and particle velocity histories from the assumed constitutive relations. To determine the accuracy of spherical PUFF wave propagation calculations, given constitutive relations and a boundary condition, we applied the code to an elastic problem for which analytic solutions are available. The results, given in Table 4, indicate that the agreement between calculated and analytic profiles is excellent, typically within one percent. We therefore proceeded to use the test problem profiles to evaluate the LASS analysis.

We determined the effects on the LASS results of (1) using a large number of characteristic points to represent the gage records versus a subset containing only the dominant structure, (2) using simple or more

71
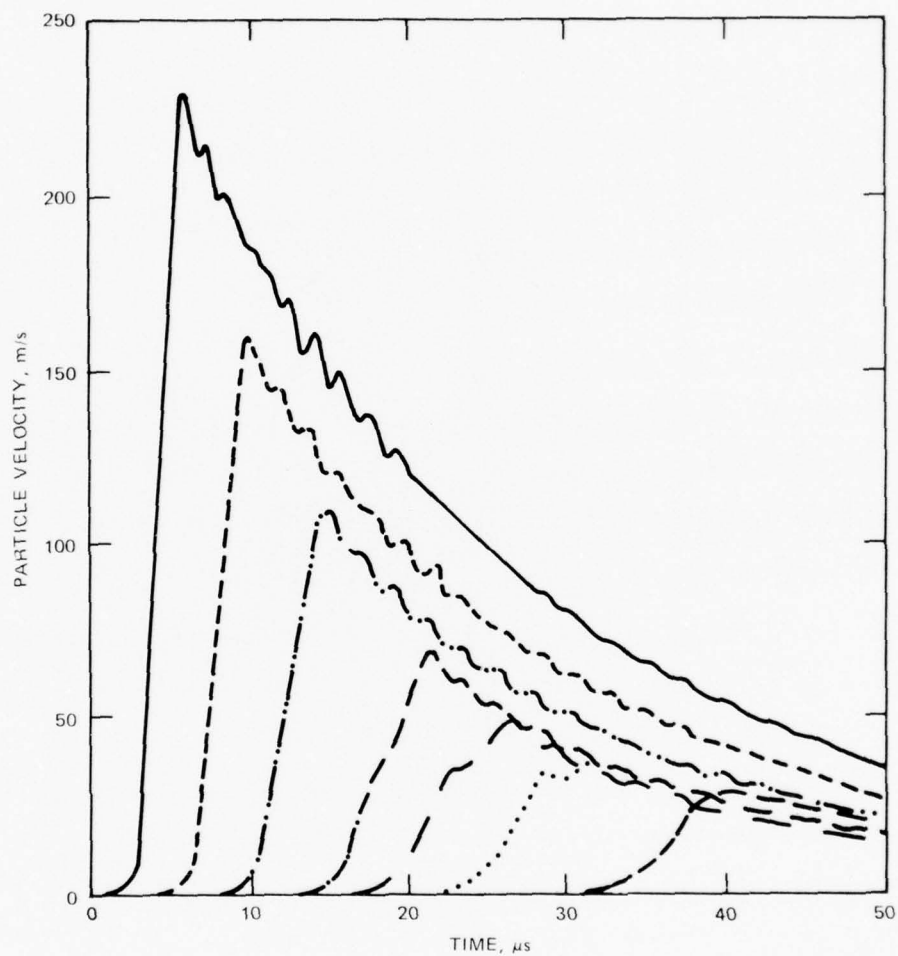
MA-3698-47

FIGURE 32   SEVEN LAGRANGE PARTICLE VELOCITY-TIME PROFILES FROM SPHERICAL
PUFF
Particles at h = 0.0642, 0.0749, 0.0862, 0.100, 0.112, 0.126, and 0.151 m.
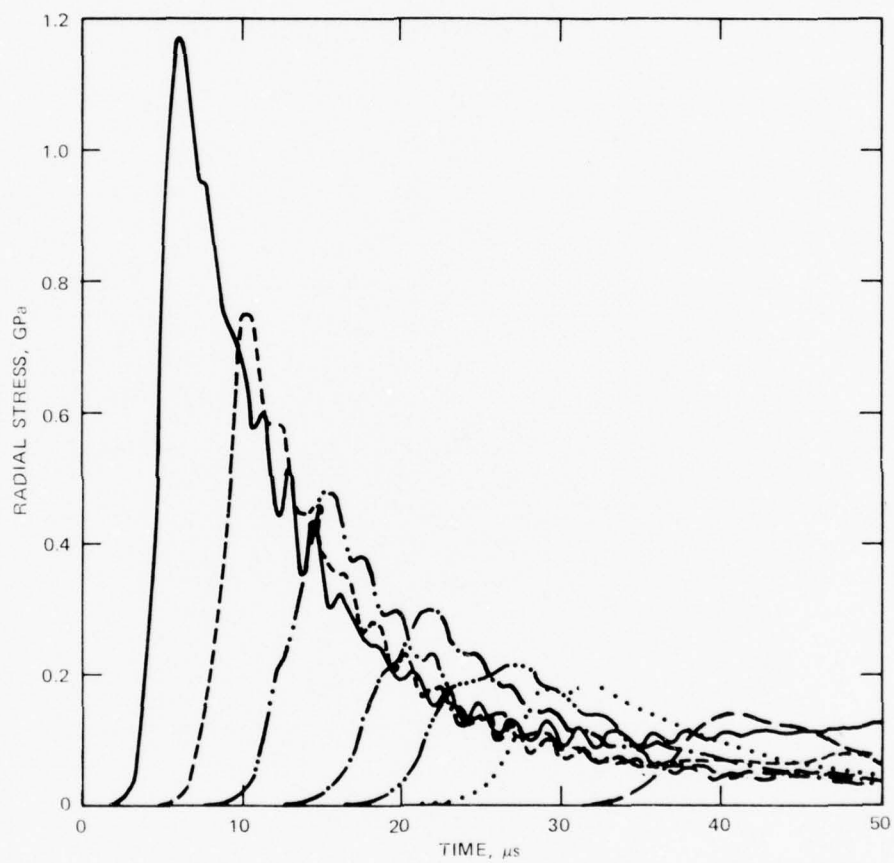
MA-3698-48

FIGURE 33   SEVEN LAGRANGE RADIAL STRESS-TIME PROFILES FROM SPHERICAL PUFF
Particles at h = 0.0650, 0.0763, 0.0876, 0.102, 0.113, 0.127, and 0.152 m.

Table 4

COMPARISON OF SPHERICAL PUFF AND ANALYTIC SOLUTIONS FOR
STRESS AND PARTICLE VELOCITY HISTORIES AT TWO LAGRANGE
COORDINATES, h_1 and h_2, IN AN ELASTIC MEDIUM[a]

Time	Stress (GPa)		Particle Velocity (m/s)	
(μs)	PUFF	EXACT	PUFF	EXACT
Gage Plane 1 at h_1 = 10.0 mm[b]				
1.635	0.0039	0.0043	0.1224	1.246
2.019	0.6809	0.6836	41.00	40.95
2.562	1.0277	1.0310	56.68	56.69
2.890	1.0562	1.0660	53.66	53.73
3.655	0.9378	0.0738	33.08	33.18
Gage Plane 5 at h_2 = 16.0 mm[b]				
2.673	0.0880	0.09165	06.41	6.172
3.217	0.5120	0.5032	30.35	29.81
3.435	0.5460	0.5394	31.65	31.33
3.655	0.5380	0.5351	30.35	30.27

[a] The problem being considered is the motion of an infinite, homogeneous, isotropic medium surrounding a spherical cavity of radius a = 1 cm. The cavity surface is given a spherical displacements such that its velocity is given by

$$V = \frac{1}{H} f'' + \frac{1}{H^2} f'$$

where H = h/a is the dimensionless Lagrange position normalized by the cavity radius a, and

$$f(\xi) = \frac{0.02}{3} \xi^3 e^{\xi}.$$

The properties of the elastic medium are defined by the bulk modulus K = 66.7 GPa and the shear modulus G = 26.7 GPa.

[b] Particle velocities at h_i; stresses at h_i + 0.05 mm.

complex mathematical functions for the link lines, and (3) using large or small integral and nonintegral numbers of incremental time steps to interpolate between pairs of characteristic points.

To provide a detailed representation of the particle velocity profiles in Figure 32, we used 16 points: 2 for the foot of the wave, 3 for the precursor knee, 2 for the peak, and 9 during release evenly spaced from 90 percent to 10 percent of peak. Similarly, to represent the stress profiles in Figure 33 in detail, we used 18 points: 3 for the foot, 3 for the precursor knee, 3 for the peak, and 9 during release from 90 percent to 10 percent of peak stress. For minimum representation retaining only essential features, we reduced each set to just three points: the precursor, the peak, and the 50 percent release point. Note that the curvature at the foot of the profiles (Figures 32 and 33) was determined to be an early-time artifact of the artificial viscosity factor in spherical PUFF; the curvature was eliminated by extrapolating the profiles to zero from higher amplitudes.

For a simple representation for the link lines, we used a two-parameter linear exponential function. For a more complex representation, we used a three-parameter quadratic exponential function.

The best case, from the points of view of accuracy and cost effectiveness, is the three-feature, quadratic exponential link line analysis. The link lines and results for that case are shown in Figures 34 and 35. The results, Figure 35, are given in the form of four stress-strain and strain-strain plots. Each plot shows calculated trajectories for four gage positions spanning the interval from the cavity radius to the station where the peak amplitudes were attenuated to the precursor level. In one of these plots, $\sigma_r - \epsilon_v$, (see upper left of Figure 35) we also show for comparison the "correct" trajectories at these positions as determined by the assumed variable modulus model and
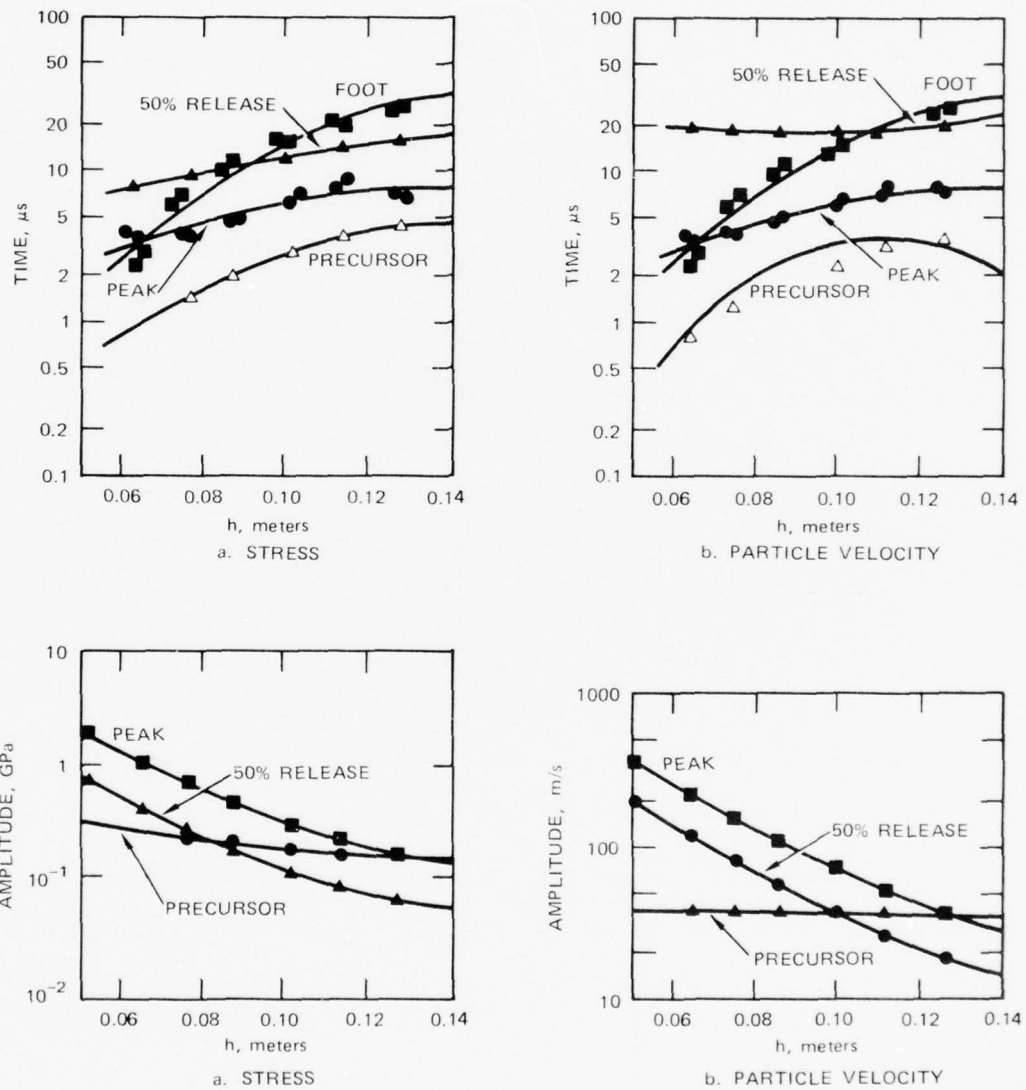
FIGURE 34   QUADRATIC EXPONENTIAL FITS TO CHARACTERISTIC FEATURES FROM
SPHERICAL PUFF STRESS AND PARTICLE VELOCITY PROFILES, FIGURES
32 AND 33
Note that in the time-h plots, the arrival of the foot of the wave is in real time,
and the times of the other features are in relative time (time measured from the
foot of the wave).
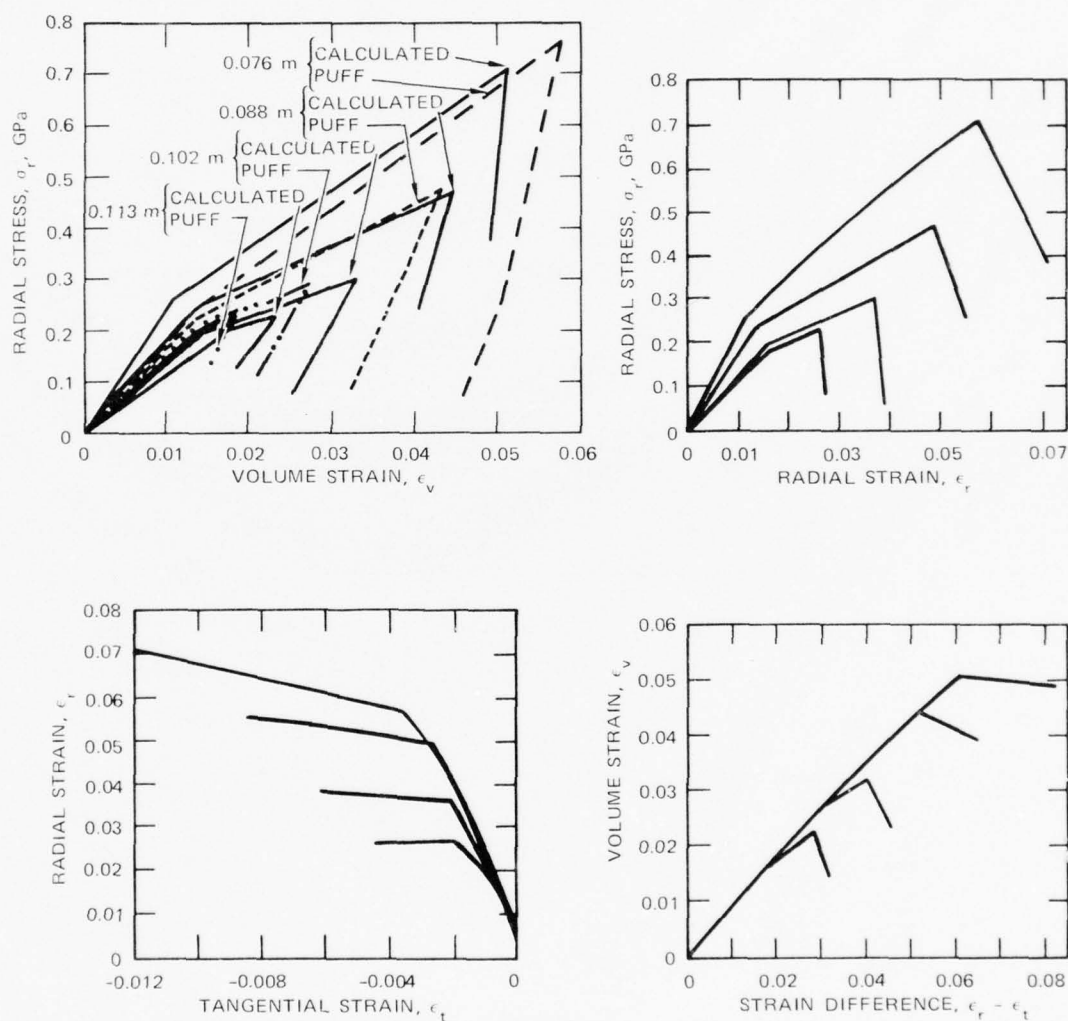
FIGURE 35   STRESS AND STRAIN TRAJECTORIES CALCULATED BY LASS FROM THE
STRESS AND PARTICLE VELOCITY PROFILES IN FIGURES 32 AND 33
The $\sigma_r - \epsilon_v$ relations used to obtain the profiles are shown in the upper left
plot for comparison with the LASS calculations.

77

spherical PUFF. Because the other three plots of LASS results give stress and strain data not generally obtained in other testing methods and hence not commonly used in material modeling, we did not evaluate their accuracy in the present work. $\dot{\phi}$ calculations are not presented because they contained understandably large oscillations and were not usable.

The four calculated $\sigma_r - \epsilon_v$ trajectories are generally correct in shape and in slope of the loading and release paths. It is important to note, however, that the two calculations for particles near the center of the measurement interval are considerably more accurate in absolute value than those near the ends of the interval. This is not surprising since the numerical estimates of the flow required by LASS will be most reliable near the center of the measurement interval. For the trajectory at 0.088 m, the calculated strain is within about 5 percent of the correct value at most stresses. We conclude that the LASS analysis even using a piecewise linear representation for the gage data, can now generate radial stress-volume strain paths accurate to about 5 percent at the center of a flow region if high quality stress and particle velocity records are obtained at 6 or 7 positions within the interval. Referring to the LASS strain definitions, equations 7 through 9, we note that the tangential strain is calculated as the time integral of a particle velocity record and that both the radial and volume strains are calculated as spatial derivatives of the time-integrated particle velocity records. Consequently we expect calculated tangential strains to be more accurate than calculated volume strains, and calculated radial strains to be comparable in accuracy to calculated volume strains.

The stress-strain trajectories calculated using 16 and 18 characteristic points rather than 3 to represent the profiles fall close to those in Figure 35. However because they displayed spurious kinks and fine structure, they are difficult to interpret. We conclude that,

78

except when the data set is of exceptional quality, it is probably cost effective to select a limited number of characteristic points corresponding to only the most distinct flow features. Although this produces a somewhat crude gage history representation, it results in reasonably accurate and easy-to-interpret stress-strain trajectories from which to extract major constitutive parameters such as effective moduli. The use of additional points in a later analysis can add detail and refinement, but usually the new link lines will show larger data scatter and hence be less accurate because of the difficulty in identifying the new points. For a first analysis, use of a small number of points provides reasonable accuracy and simplifies the analysis procedure.

Although both the linear and the quadratic exponential link lines were successful in fitting the data, the more complex quadratic form provided the better fit (see Figure 34) and was used to generate the results reported in Figure 35. Generally with field data, however, there is so much scatter that curvature cannot be defined and the quadratic form, with its extra degree of freedom, is not useful. This was the case in the analysis of CENSE II, Shots 8 and 9.

Using the best case spherical PUFF analysis reported in Figures 34 and 35, we examined the importance of the number of incremental time-steps used to interpolate between adjacent characteristic points on gage records. We concluded that this has little effect on computational accuracy; increments are now selected for maximum cost effectiveness.

Mixed Company Sandstone Small Scale Spherical Block Shots

Swift's stress and particle velocity records from scale model spherical explosive experiments on Mixed Company sandstone[19] were used by Grady to test the spherical Lagrange analysis concept two years ago.[5] Using a simple noncomputerized form of the analysis, he obtained very reasonable stress-strain paths reproduced in Figure 36(c). Last year

FIGURE 36   THREE CALCULATIONS OF LOADING AND UNLOADING PATHS FOR MIXED
COMPANY SANDSTONE (SPHERICAL BLOCK SHOTS)

(a.) LASS calculation, stress and particle
velocity peak times independent

(b.) LASS calculation, stress and particle
velocity peaks coincident
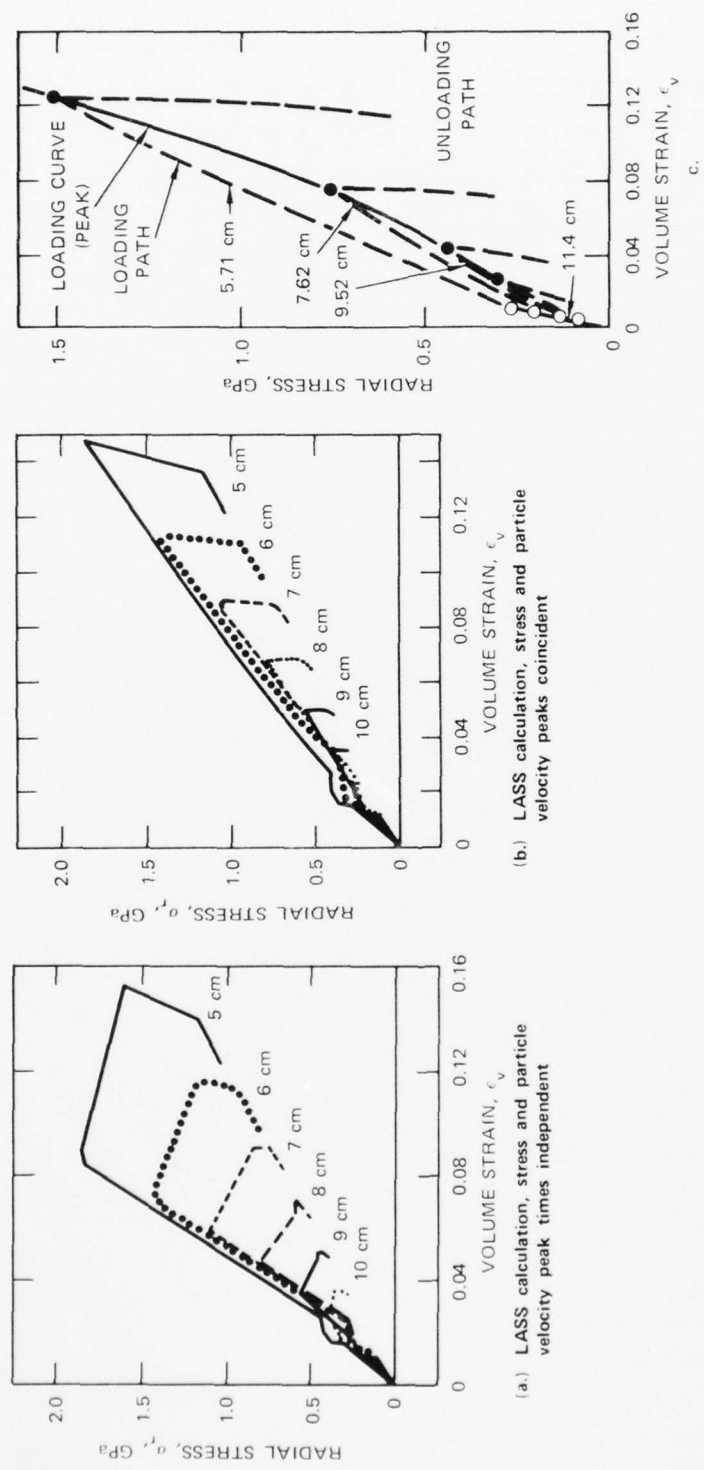
(c.) Earlier analysis using different
profile parameterization but with
peaks coincident.

MA-3698-51

80

we reanalyzed Swift's data to gain experience with the computerized LASS analysis.[6]   The resulting stress-strain trajectories, Figure 36(a), showed an apparent time-dependence in that the stress and strain did not peak together, and also the trajectories were more open and rounded near the top than those obtained by Grady.

At that time we attributed the differences between the hand-calculated and computer-calculated trajectories primarily to the fact that the stress and particle velocity histories at a given gage depth were forced to peak together in Grady's calculations but not in the LASS calculations. To test this hypothesis as well as the recent improvements in data characterization, we reanalyzed Swift's data with the present LASS analysis forcing the stress and particle velocity peaks to coincide. The resulting trajectories shown in Figure 36(b)   are in very close agreement with Grady's results, verifying our speculation in the previous final report.[6]

On the basis of these results, the spherical PUFF calculations, and our earlier experience with the spherical Lagrange analysis, we conclude that the stress and particle velocity peak times should be fit together unless a statistically significant difference exists. Otherwise the two least-squares fitting operations will generate slightly different link lines, which in general will cause the calculated $\sigma_r - \epsilon_v$ trajectories to show apparent time dependence as in Figure 36(a). The agreement between the present LASS results, Figure 36(b), and Grady's calculations by other methods, Figure 36(c), adds credibility to the current piecewise linear LASS analysis and to our ability to predict the effects on it of alternative data characterization approaches.

4. STATUS AND RECOMMENDATIONS

FIELD GAGES

Both ytterbium stress and mutual inductance particle velocity
field gages are now sufficiently reliable to provide a very high data
return. In the CENSE II events, Shots 8 and 9, they each yielded a
100 percent data return. The ytterbium stress gage records are generally
credible, long lasting, and sufficiently noise free for use in the LASS
analysis. This year these gages were also successfully fielded in two
nonspherical flow applications: the 100- and 120-ton (90.7 and 109 Mg)
Pre Dice Throw events[1] and several multiple source shots at the AFWL
Hardpan site.[12]

We conclude that the present ytterbium stress gages and emplacement
methods are satisfactory for use in weak soil sites to record stresses
in the 0.1 to 2.5 GPa range with pulse rise times and durations in the
microseconds to milliseconds range.

For these applications, we recommend no additional development
work at this time. If there are changes in measurement parameter
requirements such as accuracy, pulse rise times, pulse duration, pulse
shape (such as multiple loading), pulse amplitude, or site strength,
additional technique modification or calibration may be required.

The mutual inductance particle velocity (MIPV) gages generally
exhibit a poorer signal-to-noise ratio than the ytterbium stress gages.
However, the MIPV gage records for CENSE II, Shots 8 and 9, are signi-
ficant in that they are the first particle velocity field records of
sufficient quality for use in the analysis. Results of experimental
tests of the MIPV gage in conjunction with layered concrete matrix

82

test shots performed at the S^3 remote test site (Section 3 and Appendix D) and results of the two-dimensional code studies of MIPV gage emplacement in grout columns (Section 3) suggest that gage performance will be enhanced if short power cables are used and if the gages are fielded near the bottom of grout columns well-matched to the test site material. If these conditions are satisfied, we judge the MIPV gages to be satisfactory for use with the LASS technique subject to the conditions and restrictions listed for stress gages.

Thus, for the MIPV gage, we recommend: (1) modification of the power supplies to permit remote operation with shortened power cables to reduce noise pickup, (2) continuation of two-dimensional code simulation defining gage response in radial grout columns, and (3) experiments to confirm gage accuracy (for example, comparison with integrated accelerometer histories) and to identify major remaining sources of noise in the records.

It may also be desirable to extend the range of both gages to lower levels, nearer the failure regime of the site material. This is an important and difficult-to-model material response region. Finally, efforts should be made to quantify experimental error in both field measurements.

ANALYSIS

The present LASS analysis can determine the two independent strain tensor elements (e.g., radial and tangential or volumetric and deviatoric strains) for spherical flow to 5 to 10 percent accuracy given 5 to 8 high quality particle velocity histories. Using measured radial stress histories, it can produce any desired cross plots of these for material within the instrumented region of the flow, with highest accuracy near the center of the measurement interval. The tangetial

stress (or equivalently, stress deviator) cannot yet be accurately estimated. In principle, this quantity can be determined from the field measurements and the spherical flow equations, but our attempts to accomplish this have been unsuccessful in that the results show unrealistic oscillations. The basic problem is that the stress difference, a small quantity, appears in the flow equations as the difference in two large derivatives of the field data. We hope to improve the calculations next year by applying statistical methods to the problem to increase the signal-to-noise ratio of the calculation.

Since the LASS technique can now apparently produce dynamic in situ response data useful in modeling real sites, we recommend that error analysis procedures be added for estimating data reliability for the modeling community. We also recommend that the analysis approach be modified to produce better $\bar{\Phi}$-estimates because of the importance of shear response information to material modeling.

Secondary efforts should be undertaken to extend the range of applicability of the LASS technique. In particular, we recommend (1) that the technique be extended to cylindrical geometry (it could then be compared with or used in conjunction with CIST tests) and (2) that the effects on accuracy of nonideal sites (for example, transverse isotropy) be estimated. This latter recommendation could be implemented by using constitutive relations containing transverse anisotropy in conjunction with a two-dimensional wave propagation code to generate stress and particle velocity profiles for LASS analysis. The LASS results would then be compared with the known constitutive relations.

FIELD TESTS

The successful LASS field test in CENSE II, Shots 8 and 9, was significant in that it provided the first set of in situ field data of sufficient quality for LASS analysis. The $\sigma_r - \epsilon_v$ trajectories

produced by the analysis, especially during unloading, appear reasonable compared with static data for similar wet soils. Unfortunately, no material properties information is available for the CENSE II site material for comparison with the LASS results. No major problems are known regarding application of the LASS technique at appropriate field sites for peak stresses in the 0.1 to 2.5 GPa range. We recommend that the major effort of any follow-on work be a dedicated LASS test at a site of interest to DNA.

REFERENCES

1. W. J. Murri and C. W. Smith, "Stress Gage Measurements on Pre Dice Throw II," SRI Project Officer's Report (Draft) for Defense Nuclear Agency, Contract DNA 001-75-C-0077, Menlo Park, California, (1976).

2. D. D. Keough, C. W. Smith, and M. Cowperthwaite, "Constitutive Relations from In Situ Lagrangian Measurements of Stress and Particle Velocity," SRI Interim Report--Phase I, DASA 2685, Menlo Park, California (1971).

3. C. W. Smith, D. E. Grady, L. Seaman, and C. F. Petersen, "Constitutive Relations From In Situ Lagrangian Measurements of Stress and Particle Velocity," SRI Final Report, DNA 2883I, Menlo Park, California (1972).

4. D. E. Grady, C. W. Smith, and L. Seaman, "In Situ Constitutive Relations of Rocks," SRI Final Report DNA 3172-Z, Menlo Park, California (1973).

5. D. E. Grady, C. W. Smith, G. M. Muller, K. D. Mahrer, and C. F. Petersen, "In Situ Constitutive Relations of Soils and Rocks," SRI Final Report, DNA 3671Z, Menlo Park, California (1974).

6. C. W. Smith, C. F. Petersen, K. D. Mahrer, J. T. Rosenberg, M. J. Ginsberg, and L. B. Hall, "In Situ Constitutive Relations of Soils and Rocks," SRI Final Report, DNA 3678F, Menlo Park, California (1974).

7. C. W. Smith, "Dynamic Measurements of Stress Pulses in Tuff at Nevada Test Site," SRI Report, DNA 2811F, Menlo Park, California (1971).

8. M. J. Ginsberg, D. E. Grady, P. S. Decarli, and J. T. Rosenberg, "Effects of Stress on the Electrical Resistance of Ytterbium and Calibration of Ytterbium Stress Transducers," SRI Final Report, DNA 3577F, Menlo Park, California (1973).

9. A. H. Jones and S. J. Green, "The Role of Material Properties in Determining Ground Motion from High-Energy Detonators," Terra Tek, TR 71-41, Final Report Draft for Defense Nuclear Agency, Salt Lake City, Utah (1972).

10. C. W. Smith, "Stress Wave Measurements on the Mine Dust High Explosive Test," SRI Final Report, Contract DNA001-72-C-0235, Menlo Park, California (1972).

11. C. W. Smith, "Ytterbium Gage Measurements in Dido Queen and Husky Ace," SRI Final Report for Systems, Science and Software, Menlo Park, California (1973).

12. C. W. Smith, "Ytterbium Stress Gage Measurements at the Hardpan Site," SRI Topical Report, DNA 3805T, Menlo Park, California (1975).

13. W. L. Danek, Jr., D. L. Schooley, and F. A. Jerozal, "Particle Velocimeter for Use Close-In to Underground Explosions," DASA 1431-3 (October 1967).

14. J. D. Renick, N. H. Froula, and E. D. Stretanski, "Development of the Mutual Inductance Particle Velocimeter," ISA ASI 75263, pp. 361-373 (1975).

15. J. D. Renick, "Analysis of the Mutual Inductance Particle Velocimeter (MIPV)," AFWL-TR-74-205, Air Force Weapons Laboratory, Kirtland AFB, New Mexico (November 1974).

16.   J. G. Jackson, Jr. and J. Q. Ehrgott, "Recommended Profiles and Representative Constitutive Properties for FY 74 ESSEX I," Soil and Pavement Laboratory, U.S. Army Waterways Experiment Station, Vicksburg, Mississippi, Private Communication, 1974.

17.   M. F. Goodrich, C. M. Snell, and J. M. Thomson, "Equation of State Information for the Essex Test Site," Memorandum SDK 74-3, Lawrence Lavoratory Livermore, Livermore, California (29 March 1974).

18.   B. Mather, "Grout Design for Essex I at Fort Polk," WESCI Memo, Waterways Experiment Station, Vicksburg, Mississippi (26 April 1975).

19.   R. P. Swift, "Examination of Static and Dynamic Material Response for a Mixed Company Sandstone," Physics International Company Final Report PIFR 482, San Leandro, California (November 1973).

20.   I. Nelson, M. L. Baron, and I. Sandler, "Mathematical Models for Geological Materials for Wave Propagation Studies," in Shock Waves and Mechanical Properties of Solids, John J. Burke and Volker Weiss, Eds. (Syracuse University Press, 1971).

Appendix A

BACKGROUND

Previous work in the SRI in situ properties program and in related areas, described in a series of DNA reports, is summarized here. In 1971 Keough et al.[2] investigated the feasibility of applying the Lagrange analysis concept to radial flows and of making the in situ ground motion measurements required for the analysis. They presented the spherical flow equations and formulated an analysis for calculating specific volume from multiple Lagrange histories of radial particle velocity. This analysis was tested against an analytic solution for a specific decaying spherical shock problem and shown to be accurate. They also showed that the ytterbium piezoresistive stress gage could be modified for field use in divergent flows and they surveyed possible radial particle velocity measurement techniques.

In 1972 Smith et al.[3] modified the ytterbium stress gage design and emplacement technique and obtained successful field measurements in Middle Gust, Event 1. The mutual inductance particle velocity (MIPV) gage concept originally proposed by Engineering Physics Company was adopted, and two forms of this gage were built and evaluated. Both were shown to be feasible.

In 1973 Grady et al.[4] developed the technology and supporting theory for the longitudinal MIPV gage currently used in the LASS technique and performed successful field tests with it. They further improved ytterbium stress gage response, especially stretch sensitivity, by modifying the package design and emplacement procedures. High explosive proof tests of stress and particle velocity gages were conducted under conditions similar to field events, and stress measurements were made on Middle Gust, Event III. A practical numerical analysis was developed and

89

successfully applied to a spherical elastic problem with a known analytic solution. The analysis gave poorer results, especially during loading, when applied to experimental records obtained from small spherical shots in Westerly granite; however, these results provided insight for subsequent analysis development.

In 1974 Grady et al.[5] developed the basic piecewise linear form of the numerical LASS analysis now used for reducing field quality stress and particle velocity records to dynamic in situ stress-strain trajectories. A rate-independent variable-modulus model was fitted to the analysis results using data from small shots in Mixed Company sandstone.[19] This procedure demonstrated how the Lagrange analysis might be used to support ground motion calculations. The model, in conjunction with a spherical wave propagation code, produced wave profiles that compared favorably with the experimental data. The MIPV gage was developed to field instrument capability. Stress and particle velocity data were obtained for the CENSE I event, near Grand Junction, Colorado, and for four large HE tests for the Essex program at Fort Polk, Louisiana.

In late 1974, Smith et al.[6] refined the analysis to handle more accurately flows that exhibit rapidly changing or developing features such as precursor formation. Analysis sensitivity to internal data handling procedures was identified during reduction of records from small shots, and suggestions for improvement were offered. A series of stress and particle velocity records were obtained in the Essex I, Phase 2, event in Fort Polk, Louisiana, adding to our experience with ground motion measurements.

At DNA's request we have used the field gages developed for the in situ program, particularly the ytterbium stress gage, in several other programs during the past few years. In 1971 Smith described measurements on two 1000-pound high explosive shots at the Nevada Test Site (NTS).[7]

Later ytterbium calibration work by Ginsberg[8] led Smith to replot some

of the waveforms: these are included in a summary report by Jones and

Green.[9] In 1972 Smith reported measurements on another 1000-pound test

at NTS, the Mine Dust high explosive test.[10] Predictions and measurements

were in generally good agreement in all of these high explosive tests and

helped to establish the importance of air-filled porosity in controlling

the rate of stress wave attenuation in tuff. In 1973 we fielded ytterbium

gages on two nuclear shots, Dido Queen and Husky Ace.[11] The records were

very clean and consistent, the best we had obtained at that time. In

1975 Smith[12] reported ytterbium gage measurements made at the AFWL

Hardpan test site in a series of shots designed to investigate the stress

and motion fields generated under multiple loading by arrays of HE charges.

The high quality, long duration records obtained clearly showed the signals

from individual charges. These measurements demonstrated that passage of

the first wave produced unexpectedly large alterations in the medium,

resulting in significant amplitude enhancement of subsequent waves. In

1975 Murri and Smith[1] obtained high quality, long duration stress meas-

urements in the 0.1 - 1.0 GPa range in the 100-ton and 120-ton (90.7 and

109 Mg) Pre Dice Throw Events. These measurements are expected to provide

DNA with important field information for use in designing the 600-ton

(544 Mg) Dice Throw event and also to make stress-time and stress-range

data available to the ground shock community.

MICROCOPY RESOLUTION TEST CHART

NATIONAL BUREAU OF STANDARDS-1963-A

Appendix B

CENSE II, SHOT 5

Shot 5 of the CENSE II series conducted by WES was a half-buried, 300-pound (136-kg) cast TNT detonation. For WES's study of energy coupling into the soil, this shot was the transition shot between the air shots and the buried shots. SRI participated in this event to provide close-in measurements for WES and to evaluate gage performance and fielding techniques.

Figure B-1 shows the location of the SRI gages relative to the charge and to the ground surface. Three paddle gages were installed in 30° holes, one cylindrical epoxy gage in a radial hole that extended to the charge, and two particle velocity gages in a vertical hole beneath the charge. During the installation, numerous roots, up to an inch in diameter, and organic materials were encountered near the surface; consequently much of the volume beneath the charge was back filled with grout.

Figure B-2 shows three stress waveforms and one particle velocity waveform obtained from this shot. Gage S1 at 2.9 feet (0.88 m) from shot center was a fiberglass paddle. The trace shows a reasonable rise to about 0.3 GPa; however there is a strong dip in the unloading. The gage failed at about 625 μs but began recording again at about 740 μs--the time between is denoted by the rectangular pulse. Gage S2, a cylindrical gage at 3.1 feet (0.94 m) shows two spikes before the main energy arrival. Unfortunately, the sizable volume of grout in front of the gage clouds the interpretation of the record. The record from the paddle gage S3 at 3.9 feet (6.94 m) shows oscillations in its waveform; however, we can observe an arrival time, a rise time of about 160 μs, and a peak stress

93
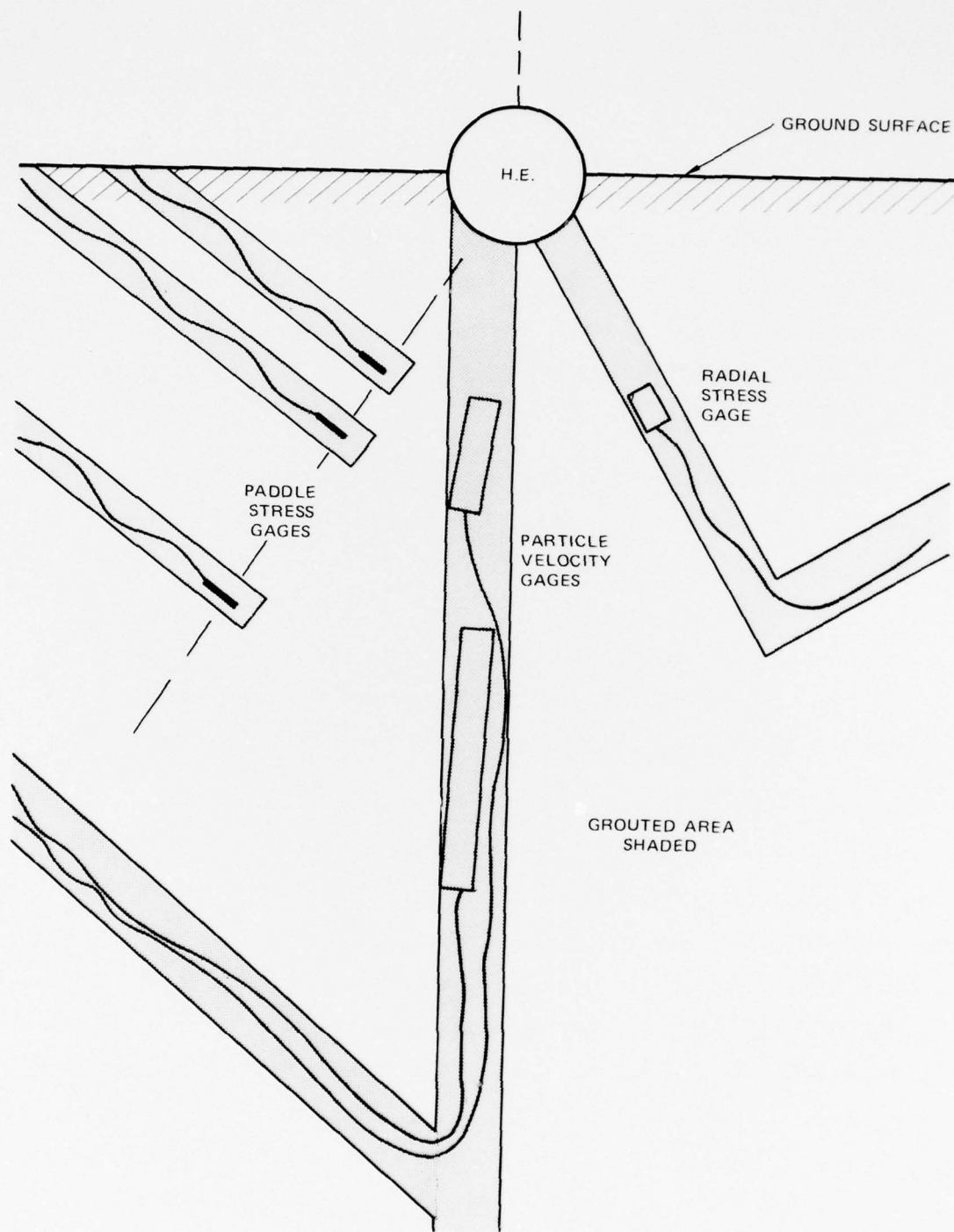
FIGURE B-1   CROSS SECTION VIEW OF CENSE II, SHOT 5

MA-3698-52

94
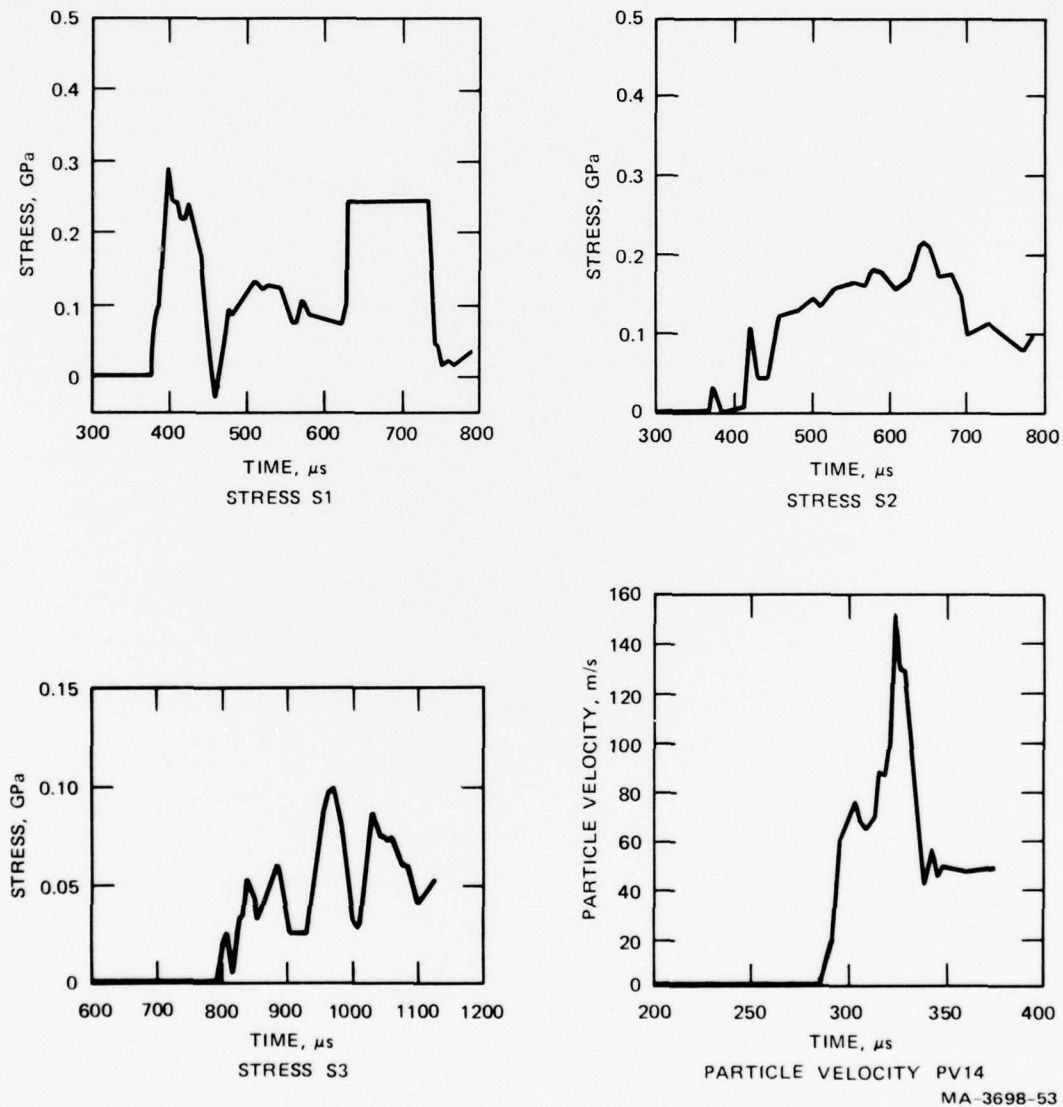
FIGURE B-2   STRESS AND PARTICLE VELOCITY WAVEFORMS FROM CENSE II, SHOT 5

MA-3698-53

95

of about 0.1 GPa. Particle velocity gage PV14 shows an anomalous spike
in its profile. The arrival and first peak of about 70 m/s are credible,
but the spike showing about 140 m/s   is not believable. Our "best guess"
amplitude predictions were too high for the outer stress and particle
velocity gages, and we obtained marginal information from these records.
The following is a tabulation of the pertinent shot information from
Shot 5.

Gage	Gage Distance (ft)	(m)	Time of Arrival (μs)	Peak	Notes
S1	2.9	0.88	375	0.28 GPa	Fiberglass paddle
S2	3.1	0.94	360	0.22 GPa	Cylindrical gage
S3	3.9	1.20	790	0.10 GPa	Epoxy paddle
S4	6.42	1.96	--	--	No data
PV14	2.75	0.84		70 m/s	140-m/s spike
PV2	5.75	1.75	$\sim$ 1700	<15 m/s	Poor record

On Shot 5 we obtained some useful arrival time and peak measure-
ments, although the overall quality of the records is poor. Surface
organic material and roots probably affected the records; also the lack
of good predictions was a detriment.

Appendix C

DATA DISCUSSION, CENSE II, SHOTS 8 AND 9

The stress and particle velocity profiles measured in CENSE II, Shots 8 and 9, were presented in Section 3, Figures 11-14. Details of those profiles are discussed below.

STRESS RECORDS, SHOT 8 (SEE FIGURE 11)

The closest gage, S1, a cylindrical epoxy gage shows a rapidly rising trace to 0.84 GPa and then unloads to about half the peak stress. At that time the trace flattens and eventually starts to rise. Although this rising portion is not valid stress data, the gage at least shows electrical continuity for well over 5 ms. In examining the recovered gage, we saw delaminations in the epoxy. (During fabrication, the epoxy is added in half-inch layers.) In particular there was a delamination immediately behind the ytterbium grid and a fracture line though the grid itself. We suspect that the rising portion of the waveform is associated with the delamination process. Gage S2 was a fiberglass paddle and shows a shock arrival with a peak of 0.76 GPa. About 60 μs after the peak the gage failed temporarily; we have arbitrarily chosen to show this section with a rectangular shape. The data near 500 μs is useful because it shows when the stress was approximately zero. It is not clear what generates the 20-μs humps in the unloading.

Gage S3 was a paddle made with 6.3-mm-thick epoxy sheet. Again we see a shock arrival, a clearly defined peak, some oscillations in the unloading, and near zero stress. By the time the stress wave reached gage S4 at 1.44 m, the character of the wave has started to change. Although we still see a shock arrival and a 0.12-GPa peak, the pulse has lengthed. The overall character of the unloading shows a dip and rise whose origin is unclear. Gage S5 shows a rise time of about 300 μs, a 0.1 GPa peak, and reasonably uniform unloading.

97

PARTICLE VELOCITY RECORDS, SHOT 8 (SEE FIGURE 12)

Because of the noisy waveforms, the peak values are ambiguous.
When the wave reaches the front of a gage, we see a rapid rise to some
peak particle velocity and then a decay until the wave reaches the end
of the gage. At that time there is often a large spike in the waveform.

Gage P6 shows the arrival, a peak, the decay, and the end spike
near 500 μs. The noise pickup, however, obscures the size of the peak.
The first shoulder, at 129 m/s, is followed by a dip and a higher peak
of 150 m/s; it is not clear which of these is the true peak. Gage P7
is easier to interpret for here we see a peak, a decay, and the end
spike near 600 μs.

In P8 and P9 there were a series of very high frequency noise
bursts, which were arbitrarily replaced in data reduction by rectangular
shapes. Our experience is that these high frequency noise bursts are
electrical in origin and not caused by ground motion.

In the record from gage P10 the wave reaches the end of the gage
at 2200 μs; the subsequent trace is not valid data. This record shows,
however, that at 1.65 m from charge center the particle velocity generated
by the passage of the stress wave rises to a peak of 20 to 25 m/s in
approximately 800 μs and is reasonably constant for 600 to 700 μs after
this peak.

STRESS RECORDS, SHOT 9 (SEE FIGURE 13)

The stress gage records from Shot 9 are characterized by long
recording times. Gage S1 was a cylindrical gage and produced a record
with a plausible waveform. Records from these cylindrical gages have
fewer oscillations in their unloading than those from the paddle gages.
The oscillations in the paddle gage records may be associated with
reverberations in the vertical grout column.

98

Gage S2 shows a rise to a 0.6 GPa shoulder followed by an unusual spike of 1 GPa amplitude. Examination of the recovered gage showed damage in the grid area, as if a high velocity pebble had impacted the area. Such an impact would have caused a stress spike. In the unloading portion of the record there is another spike and a 20-μs temporary break in the record (shown as a rectangular shape) just before the ultimate gage failure.

Gages S3, S4, and S5 show credible records; a rapid rise to a peak followed by a gradual unloading with a certain amount of oscillation in the unloading. At the outer gage, S5, we still see a shock arrival, while in Shot 8 at this distance the wave showed a finite rise time.

PARTICLE VELOCITY RECORDS, SHOT 9 (SEE FIGURE 14)

Again we see mixed results. Gage P6 shows a clear peak, minimum noise, and a distinct ending; however, gage P9 shows ambiguities in its peak, that is, a first shoulder followed by subsequent peak. Gages P7 and P8 are reasonably good in that one can average the oscillations and obtain a useful waveform. The farthest out gage, P10, shows much oscillation; however, the amplitude of 20 m/s is approaching the lower limits of MIPV gage usefulness. This lower limit occurs because the gage must deform to produce output and at low particle velocities the strength of the gage inhibits the deformation and causes under registration.

Appendix D

PARTICLE VELOCITY GAGE MEASUREMENTS IN CONCRETE

In the fall of 1974, Systems, Science and Software (S^3) conducted a series of small explosive shots to model stress wave propagation in layered geologic materials (Contract DNA001-74-C-0082). In three of these shots SRI installed mutual inductance particle velocity gages in order to gain experience with the field gage in a relatively quiet and controlled test environment. These gages, plus ytterbium stress gages installed by S^3, were cast in concrete blocks along with a spherical container to hold the explosive. One shot was high strength concrete only; the other two consisted of a soft concrete layer over the high strength concrete. Particle velocity waveforms were obtained at two of the three locations in each shot.

EXPERIMENT DESCRIPTION

The gages were small-scale versions of the MIPV field gages used in previous work. The experiment was constructed by casting the concrete into 6 x 6 x 6 ft (1.8 x 1.8 x 1.8 m) plywood forms containing the gages, held in position by wire and turn buckles. Figure D-1 shows the gages and plywood forms; the three vertical gages are particle velocity, the two horizontal gages are the S^3 ytterbium stress gages. The high strength concrete was cast in the lower portion of this form; after curing, the soft concrete and explosive container were added. (Details on two concretes are available from S^3.) In all three shots the 8-inch-diameter (0.20 m) explosive container held about 10 pounds (4.53 kg) of nitromethane, which was centrally detonated by a tetryl pellet and exploding bridge wire.
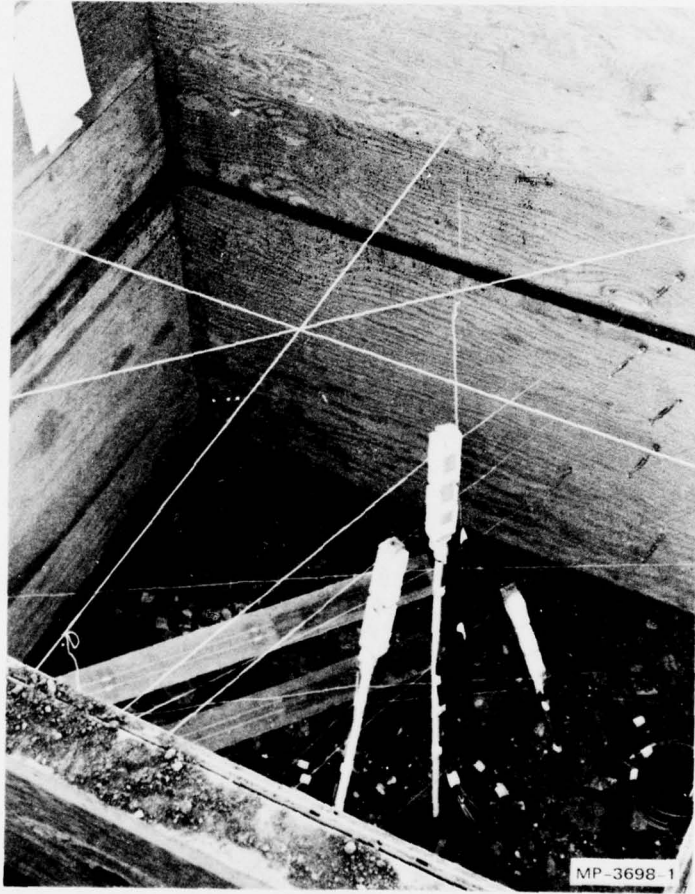
101

FIGURE D-1   PARTICLE VELOCITY AND STRESS GAGES
MOUNTED IN PLYWOOD FORMS PRIOR TO
CONCRETE POURING

The first shot (SP7) consisted solely of the high strength concrete and had particle velocity gages at 9.75, 14.5, and 34.5 inches (0.248, 0.368, and 0.876 m) from the charge center. (Details on the stress gages locations are available from S^3.) In the second shot (SP8), the charge center was located in the soft concrete 14 inches (0.35 m) above the interface between the soft and high strength materials. Particle velocity gages were located at 11.25, 21, and 37 inches (0.268, 0.533, and 0.940 m); thus, 2.75 inches (0.0698 m) of one gage was in the soft material and the rest in the high strength concrete. In SP9, the third shot, the charge center was located 30 inches (0.762 m) above the interface; the first particle velocity gage at 14.5 inches (0.368 m) was wholly in the soft material. The second gage at 24.5 inches (0.622 m) protruded 5.5 inches (0.140 m) into the soft material, and the third gage at 35 inches (0.889 m) was wholly in the stiff concrete.

Gage output was recorded on oscilloscopes in the bunker at S^3's Green Farm Test Site. No notable electrical pickup was observed, and the particle velocity gages operated correctly.

DATA

From Shot SP7 we obtained the two records shown in Figure D-2. The record from the gage at 9.75 inches (0.248 m) rises rapidly to a peak particle velocity of 139 m/s and then decreases to a value of about 90 m/s. Near 250 μs, the stress wave has reached the end of the 1-foot-long (0.30 m) gage and the output drops rapidly. The second record, from the gage at 14.5 inches (0.368 m), shows how the particle velocity waveform has changed in the 4.25 inches (0.108 m) between the gages; the risetimes has increased about 5 times, the width of the initial peak or spike has increased, and the overall amplitude has decreased. Since the oscilloscope recorded only until 300 μs, we did not observe the time that the stress wave reached the end of the gage.

103
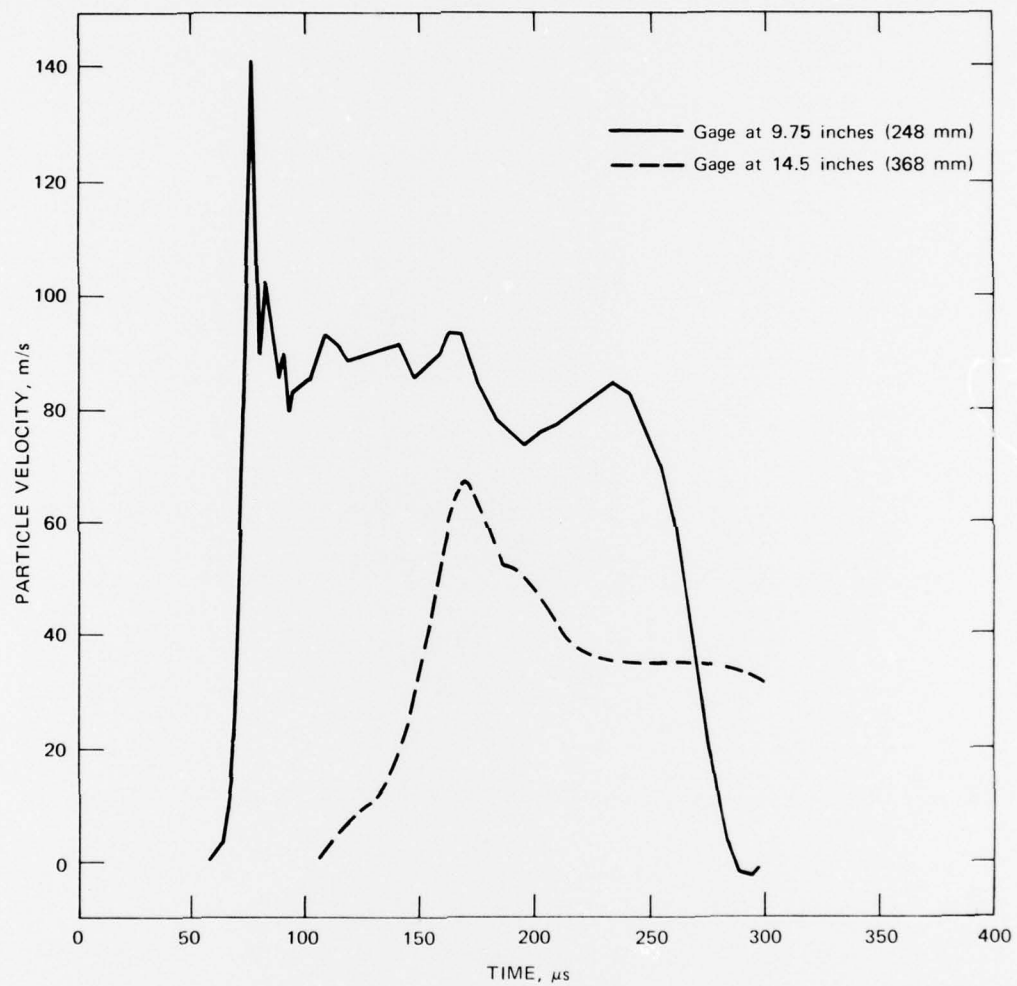
FIGURE D-2   PARTICLE VELOCITY RECORDS FROM SHOT SP7

MA-3698-2A

The third gage in this all stiff concrete shot produced an anomalous waveform.

In the second shot (SP8), there was a soft layer over the stiff concrete, and the first gage extended 2.75 inches (0.0698 m) into the soft layer. Figure D-3 shows the two records obtained. The close gage, at 11.25 inches (0.286 m), shows a 32 μs rise to 86 m/s peak, which does not show the spike nature that we observed in the stiff concrete. The slowly decaying peak shows an abrupt dip at 220 μs; from this time on the waveform decays. The gage in the stiff concrete at 21 inches (0.533 m) shows a gradual rise to a rounded peak of 16 m/s, followed by a smooth decay. For the gage at 37 inches (0.940 m) the wave appeared to arrive before the oscilloscope was turned on, that is, before 400 μs. The amplitude was too small to produce a usable record; the upper limit for the amplitude is 6 m/s.

In Shot SP9 the first particle velocity gage was entirely in the soft concrete. The precursor seen in Figure D-4 for this close gage has an amplitude of 1.3 m/s which is followed by a rapid rise to a peak of 84 m/s. The double spike peak is followed by a decay to a plateau that gradually decays. The gage at 24.5 inches (0.622 m) shows a very gradual rise above the zero level, reaches a peak of 10.5 m/s, and shows a slight amplitude decrease by the end of the recording interval. As in SP8, the amplitude produced by the third gage was too small to produce a usable record.
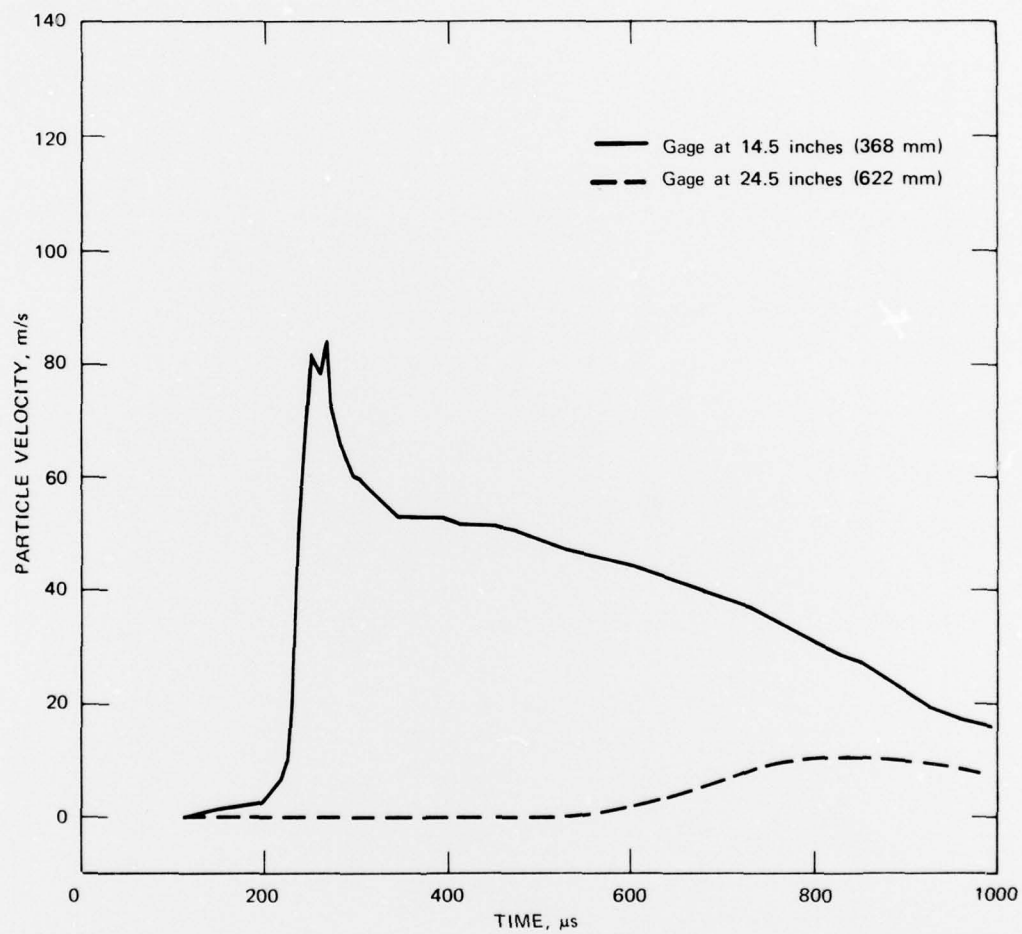
DISCUSSION

Table D-1 tabulates arrival times and peak amplitudes for the gages in the three shots. Each gage was observed by two oscilloscopes whose amplitude and arrival times differed slightly; hence we have given the data from both oscilloscopes.
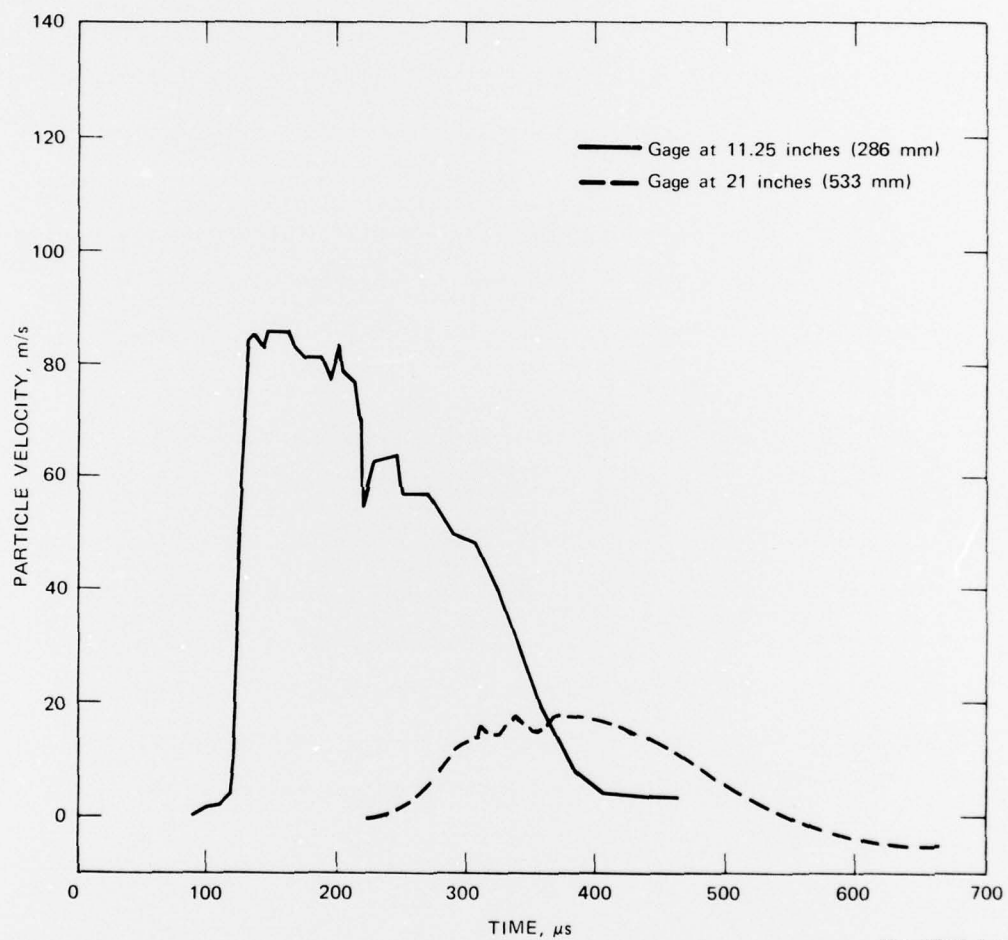
FIGURE D-3   PARTICLE VELOCITY RECORDS FROM SHOT SP8

FIGURE D-4   PARTICLE VELOCITY RECORDS FROM SHOT SP9

Table D-1

PARTICLE VELOCITY DATA SUMMARY CONCRETE TESTS

Shot No.	Gage No.	Distance (inches)	(m)	Scope No.	Time First Arrival (μs)	Time Peak (μs)	Peak (m/s)	Notes
7	P5	9.75	0.248	D2	64	76	139	Gage in stiff material
				E2	63	75	140	Gage in stiff material
	P6	14.5	0.368	D3	103	166	66	Gage in stiff material
				E3	106	169	68	Gage in stiff material
	P10	34.5	0.876	--	--	--	--	Anomalous waveform
8	P1	11.25	0.286	D2	98	130	86	2.75 in. (0.0698 m) of gage in soft material, rest in stiff material
				D3	103	138	92.6	
	P2	21	0.533	E4	239	~350	15.5	Gage in stiff material
				D4	235	~360	17.7	Gage in stiff material
	P8	37	0.940	Arrival not recorded; maximum amplitude 6 m/s				
9	P3	14.5	0.368	D2	144	248	84	In soft material, precursor 1.3 m/s
				D3	140	--	--	
	P4	24.5	0.622	D4	~500	~775	10.5	5.5 in. (0.140 m) of gage in soft material
	P9	35	0.889	Arrival not recorded; maximum amplitude 1 m/s				

The waveforms from SP7 appear entirely reasonable and clearly show the change of waveforms over the 4.75 inches (0.121 m) between the two gages. From the separation of the two gages and the times of first energy arrival, we obtain a velocity of 2.94 mm/μs, which is the stress wave velocity averaged over the range of 9.75 to 14.5 inches (0.248 to 0.368 m). By using the first energy arrival on the gage at 9.75 inches (0.248 m) and assuming that the wave reached the end of the gage at 247 μs, the point where the amplitude starts to drop rapidly, we measure a stress wave velocity of 1.65 mm/μs averaged over 9.75 to 21 inches (0.248 to 0.533 m). Notably absent in the second shot is the spike on the first waveform, for even at the greater distance in the third shot, the spike is present on the first gage of that shot. The rapid drop in amplitude at 220 μs for this first gage in SP8 is most likely related to the soft/stiff material interface. Using the distance the gage protruded into the soft concrete and the time from main energy arrival to the marked dip, we calculate a velocity of 0.87 mm/μs. This value is reasonable, for the soft concrete was expected to have a sonic velocity about 1 mm/μs. Assuming that the dip represents the interface, the particle velocity just below the interface is 64 m/s. Beyond 300 μs the amplitude drops rapidly; presumably the stress wave has reached the end of the gage. The second gage of SP8 is quite reasonable and is most likely the steady-state wave shape. The small ripples near the peak are minor electrical noise.

In the third shot the double spike on the first waveform is unusual. Using a wave velocity of 1.0 mm/μs and a gage length of 1 foot (0.30 m), we see that the inflection near 480 μs is probably associated with the arrival of the wave at the end of the gage. Thus amplitude beyond that time is not free-field particle velocity. For the second gage in SP9 it is difficult to assess the arrival time accurately. The measured peak of 10.5 m/s is well below the expected operating range of the gage. On the other hand the precursor on the first gage in this shot is clearly there and measurable, although the accuracy of the measurement is probably low.

109

DISTRIBUTION LIST

DEPARTMENT OF DEFENSE

Assistant to the Secretary of Defense
Atomic Energy
      ATTN: Executive Assistant

Defense Advanced Rsch. Proj. Agency
      ATTN: TIO

Defense Civil Preparedness Agency
Assistant Director for Research
      ATTN: Admin. Officer

Defense Documentation Center
12 cy ATTN: DD

Defense Intelligence Agency
      ATTN: DB-4C, E. O'Farrell
      ATTN: DB-4E

Defense Nuclear Agency
      ATTN: DDST
2 cy ATTN: SPSS
4 cy ATTN: TITL

Field Command
Defense Nuclear Agency
      ATTN: FCPR
      ATTN: FCTMOF

Interservice Nuclear Weapons School
      ATTN: TTV

Joint Strat. Tgt. Planning Staff
      ATTN: NRI-STINFO Library

Livermore Division Fld. Command, DNA
      ATTN: FCPRL

NATO School (SHAPE)
      ATTN: U.S. Documents Officer

Under Secy. of Def. for Rsch. & Engrg.
      ATTN: Strategic & Space Systems (OS)

WWMCCS System Engineering Org.
      ATTN: T. Neighbors

DEPARTMENT OF THE ARMY

BMD Advanced Technology Center
      ATTN: 1CRDABH-X
      ATTN: ATC-T

Chief of Engineers
      ATTN: DAEN-MCE-D
      ATTN: DAEN-RDM

Deputy Chief of Staff for Ops. & Plans
      ATTN: MOCA-ADL

Harry Diamond Laboratories
      ATTN: DELHD-N-NP
      ATTN: DELHD-N-TI

DEPARTMENT OF THE ARMY (Continued)

Redstone Scientific Information Ctr.
      ATTN: Chief, Documents

U.S. Army Ballistic Research Labs
      ATTN: DRDAR-BLE, J. Keefer
      ATTN: DRXBR-X, J. Meszaros
      ATTN: DRXBR-BLE, W. Taylor
      ATTN: Technical Library

U.S. Army Engineer Center
      ATTN: ATSEN-SY-L

U.S. Army Engineer Div. Huntsville
      ATTN: HNDED-SR

U.S. Army Engineer Div. Ohio River
      ATTN: ORDAS-L

U.S. Army Engr. Waterways Exper. Station
      ATTN: Library
      ATTN: G. Jackson
      ATTN: J. Strange
      ATTN: L. Ingram
      ATTN: W. Flathau

U.S. Army Material & Mechanics Rsch. Ctr.
      ATTN: Technical Library

U.S. Army Materiel Dev. & Readiness, CMD
      ATTN: DRXAM-TL

U.S. Army Nuclear & Chemical Agency
      ATTN: Library

DEPARTMENT OF THE NAVY

Civil Engineering Laboratory
Naval Construction Battalion Center
      ATTN: R. Odello
      ATTN: Code L08A
      ATTN: S. Takahashi

Naval Electronic Systems Command
      ATTN: PME 117-21A

Naval Facilities Engineering Command
      ATTN: Code 03A
      ATTN: Code 04B
      ATTN: Code 09M22C

Naval Material Command
      ATTN: MAT 08T-22

Naval Postgraduate School
      ATTN: Code 0142

Naval Research Laboratory
      ATTN: Code 2627

Naval Surface Weapons Center
      ATTN: Code F31

DEPARTMENT OF THE NAVY (Continued)

Naval Surface Weapons Center
ATTN: Technical Library & Information Services
Branch

Naval Underwater Systems Center
ATTN: Code EM, J. Kalinowski

Naval War College
ATTN: Code E-11

Naval Weapons Evaluation Facility
ATTN: Code 10

Office of Naval Research
ATTN: Code 474, N. Perrone
ATTN: Code 715
ATTN: Code 461, J. Warner

Office of the Chief of Naval Operations
ATTN: OP 981
ATTN: OP 03EG

Strategic Systems Project Office
ATTN: NSP-43

DEPARTMENT OF THE AIR FORCE

Air Force Geophysics Laboratory
ATTN: LWW, K. Thompson

Air Force Institute of Technology, Air University
ATTN: Library

Air Force Systems Command
ATTN: DLCAM

Air Force Weapons Laboratory
ATTN: DE, M. Plamondon
ATTN: SUL

Assistant Chief of Staff
Intelligence
ATTN: INT

Deputy Chief of Staff
Research, Development, & Acq.
ATTN: AFRDQSM

Deputy Chief of Staff
Programs & Resources
ATTN: PRE

Foreign Technology Division, AFSC
ATTN: NICD Library

Rome Air Development Center, AFSC
ATTN: Documents Library/TSLD

Space & Missile Systems Organization/MN
ATTN: MNN

Strategic Air Command/XPFS
ATTN: NRI-STINFO Library

DEPARTMENT OF ENERGY

Department of Energy
ATTN: Doc. Con. for Technical Library

DEPARTMENT OF ENERGY (Continued)

Department of Energy
ATTN: Doc. Con. for Classified Library

Department of Energy
ATTN: Doc. Con. for Technical Library

Lawrence Livermore Laboratory
ATTN: Doc. Con. for Technical Information
Department Library
ATTN: Doc. Con. for L-94, L. Woodruff

Los Alamos Scientific Laboratory
ATTN: Doc. Con. for Reports Library
ATTN: Doc. Con. for R. Bridwell

Oak Ridge National Laboratory
Union Carbide Corporation
Nuclear Division
X-10 Lab Records Division
ATTN: Doc. Con. for Technical Library
ATTN: Doc. Con. for Civil Defense Research
Project

Sandia Laboratories
Livermore Laboratory
ATTN: Doc. Con. for Library & Security
Classification Division

Sandia Laboratories
ATTN: Doc. Con. for A. Chabai
ATTN: Doc. Con. for L. Hill
ATTN: Doc. Con. for 3141

OTHER GOVERNMENT AGENCIES

Central Intelligence Agency
ATTN: RD/SI, Rm. 5G48, HQ Bldg. for J. Ingley

Department of the Interior
Bureau of Mines
ATTN: Technical Library

DEPARTMENT OF DEFENSE CONTRACTORS

Aerospace Corp.
ATTN: Technical Information Services

Agbabian Associates
ATTN: M. Agbabian

Applied Theory, Inc.
2 cy ATTN: J. Trulio

AVCO Research & Systems Group
ATTN: Library

BDM Corp.
ATTN: Corporate Library

Boeing Co.
ATTN: Aerospace Library

California Research & Technology, Inc.
ATTN: S. Shuster
ATTN: K. Kreyenhagen
ATTN: Library

Calspan Corp.
ATTN: Library

112

Civil/Nuclear Systems Corp.
    ATTN: J. Bratton

University of Dayton
Industrial Security Super KL-505
    ATTN: H. Swift

University of Denver
Colorado Seminary
Denver Research Institute
    ATTN: Sec. Officer for J. Wisotski

EG&G Washington Analytical Services Center, Inc.
    ATTN: Library

Eric H. Wang
Civil Engineering Rsch. Fac.
    ATTN: N. Baum

Gard, Inc.
    ATTN: G. Neidhardt

General Electric Company—TEMPO
Center for Advanced Studies
    ATTN: DASIAC

IIT Research Institute
    ATTN: M. Johnson
    ATTN: R. Welch
    ATTN: Documents Library

University of Illinois
Consulting Services
    ATTN: N. Newmark

Institute for Defense Analyses
    ATTN: Classified Library

Kaman AviDyne
Division of Kaman Sciences Corp.
    ATTN: E. Criscione
    ATTN: N. Hobbs
    ATTN: Library

Kaman Sciences Corp.
    ATTN: Library

Lockheed Missiles and Space Co., Inc.
    ATTN: T. Geers
    ATTN: Technical Information Center, D/Coll.

Lovelace Biomedical & Environmental Research
Institute, Inc.
    ATTN: R. Jones

McDonnell Douglas Corp.
    ATTN: R. Halprin

Merritt Cases, Inc.
    ATTN: Library
    ATTN: J. Merritt

Physics International Co.
    ATTN: Technical Library
    ATTN: J. Thomsen
    ATTN: L. Behrmann
    ATTN: F. Sauer
    ATTN: E. Moore

R&D Associates
    ATTN: J. Carpenter
    ATTN: R. Port
    ATTN: H. Brode
    ATTN: A. Latter
    ATTN: C. MacDonald
    ATTN: Technical Information Center
    ATTN: W. Wright, Jr.
    ATTN: J. Lewis

R&D Associates
    ATTN: H. Cooper

Science Applications, Inc.
    ATTN: Technical Library

Science Applications, Inc.
    ATTN: D. Bernstein
    ATTN: D. Maxwell

Southwest Research Institute
    ATTN: W. Baker
    ATTN: A. Wenzel

SRI International
    ATTN: B. Gasten
    ATTN: G. Abrahamson
    ATTN: J. Rosenburg
    ATTN: C. Smith
    ATTN: D. Curran

Systems, Science & Software, Inc.
    ATTN: D. Grine
    ATTN: T. Cherry
    ATTN: T. Riney
    ATTN: Library

Terra Tek, Inc.
    ATTN: A. Abou-Syaed
    ATTN: Library
    ATTN: S. Green

Tetra Tech, Inc.
    ATTN: Library
    ATTN: L. Hwang

TRW Defense & Space Sys. Group
    ATTN: Technical Information Center
    ATTN: P. Bhutta
 2 cy ATTN: P. Dai

TRW Defense & Space Sys. Group
    ATTN: E. Wong

Universal Analytics, Inc.
    ATTN: E. Field

Weidlinger Assoc., Consulting Engineers
    ATTN: M. Baron

Westinghouse Electric Corp.
    ATTN: W. Volz